Exploring cosmic ray origins with ground-based EAS arrays Tunka and HiSCORE

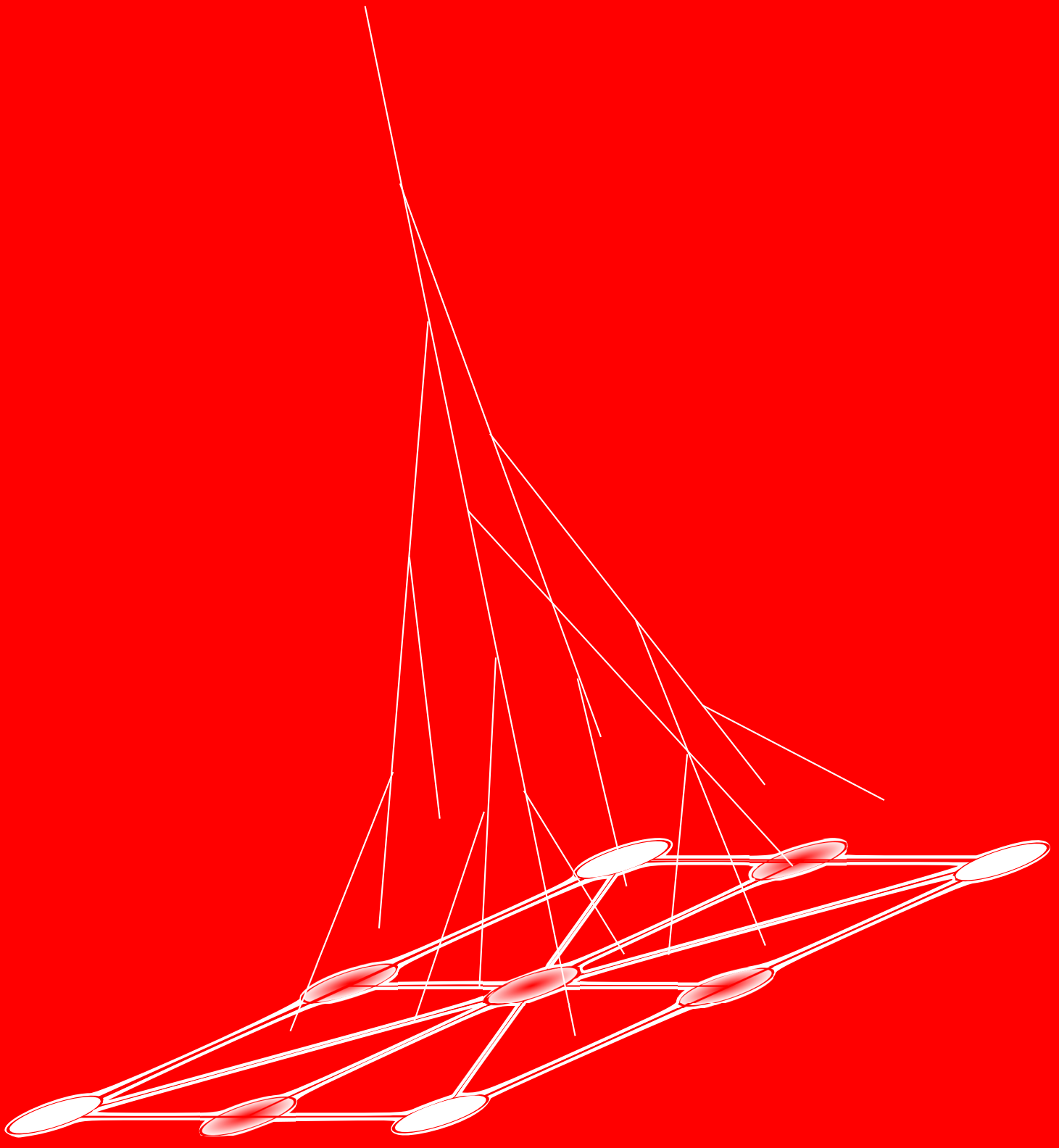

Sergey Epimakhov

Exploring cosmic ray origins with ground-based EAS arrays Tunka and HiSCORE

Dissertation with the aim of achieving a doctoral degree

at the

Faculty of Mathematics, Informatics and Natural Sciences
Department of Physics
University of Hamburg

Submitted by
Sergey Epimakhov

Hamburg 2015

Gutachter der Dissertation:	Prof. Dr. Dieter Horns Dr. Vasily Prosin
Gutachter der Disputation:	Prof. Dr. Günter Sigl Prof. Dr. Caren Hagner Dr. Martin Tluczykont
Datum der Disputation:	24.09.15
Dekan der MIN Fakultät:	Prof. Dr. Heinrich Graener

Dedicated to my family

Per aspera ad astra

Abstract

The main properties of cosmic radiation over the last hundred years have been studied with good accuracy and are not in doubt: cosmic rays are nuclei of almost all elements of the periodic table with a small fraction of other particles coming from the outer space at Earth with the non-thermal energy spectrum from 10^6 to 10^{20} eV. However, the source of cosmic rays still remains unknown. To examine the question of the origin of cosmic rays neutral particles are perfectly suited as messengers. Thereby the gamma ray sky in the range above 10 – 100 TeV is of great interest. Hypothetical galactic accelerators, pevatrons, must have gamma ray spectra up to these energies.

A new non-imaging wide-angle Cherenkov experiment HiSCORE is aimed at searching the ultra-high energy gamma rays above 30 TeV and measuring the primary spectrum and mass composition of cosmic rays above 100 TeV with a unprecedented accuracy. In autumn 2013, a first 9-station engineering array has been deployed at the site of the existing Cherenkov experiment Tunka-133 in Russia.

In this thesis, a summary of basic reconstruction techniques used in the Tunka experiment to date is given. The recent results has been achieved in the all-particle spectrum reconstruction and the mass composition analysis of cosmic rays in the PeV range is shown.

The first data of HiSCORE-9 have been analysed and the array performance has been studied. The results were complemented with Monte Carlo simulations and the instrument potential for the detection of gamma rays has been investigated.

A new fast code CHERRY to simulate Cherenkov light in the atmosphere from cosmic rays and gamma rays above 10 TeV has been developed. Preliminary results of the Tunka-133 performance obtained with this program are discussed.

Zusammenfassung

Die Hauptbestandteile der kosmischen Strahlung wurden in den letzten hundert Jahren mit einer guten Genauigkeit erforscht und somit besteht kein Zweifel: Kosmische Strahlung, die die Erde erreicht, besteht aus den Kernen fast aller Elemente des Periodensystems und einem kleinen Teil anderer Teilchen in einem nicht-thermischen Energiespektrum von 10^6 eV bis 10^{20} eV. Ihr Ursprung bleibt aber weiterhin unbekannt. Um eine Antwort auf die Frage nach dem Ursprung der kosmischen Strahlung zu finden, sind neutrale Teilchen perfekt als Boten geeignet. Von besonderem Interesse ist der Gammastrahlenhimmel ab Energien über 10^{14} eV (100TeV). Hypothetische galaktische Beschleuniger, so genannte Pevatrone, müssten nämlich Gammastrahlungsspektren bis zu diesen Energien besitzen.

Das neue nichtabbildende Weitwinkel-Cherenkovlichtexperiment HiSCORE richtet sich mit einer nie dagewesenen Präzision auf die Erforschung von ultrahochenergetischer Gammastrahlung über 30 TeV und des Primärspektrums sowie der Massenzusammensetzung kosmischer Strahlung über 100 TeV. Im Herbst 2013 wurde das erste Versuchsdetektorfeld mit neun Stationen (HiSCORE-9) auf dem Gelände des bereits existierenden Cherenkovlichtexperimentes Tunka-133 in Russland gebaut.

In dieser Arbeit wird eine grundlegende Zusammenfassung der aktuellen Schauerrekonstruktionsmethode des Tunka-Experiments gegeben. Die erlangten Ergebnisse umfassen die Rekonstruktion eines Gesamtteilchenspektrums und die Analyse der Massenzusammensetzung der kosmischen Strahlung im PeV-Energiebereich.

Die ersten Daten von HiSCORE-9 wurden analysiert und mittels der Schachbrettmethode die Leistung des Detektorfeldes untersucht. Dies wurde mit Monte-Carlo-Simulationen ergänzt und die Möglichkeiten zum Detektieren von Gammastrahlung wurden erforscht.

Ein neuer und schneller Code CHERRY zur Simulation des Cherenkovlichtes, das in der Atmosphäre durch kosmische Strahlung und Gammastrahlung oberhalb von 10 TeV erzeugt wird, wurde entwickelt. Vorläufige Ergebnisse zur Detektorleistung von Tunka-133, die mit diesem Programm erhalten wurden, werden diskutiert.

Acknowledgements

I wish to express my sincere thanks to my supervisor Dieter Horns and to our HiSCORE group leader Martin Tluczykont for giving me a chance to work in this breakthrough project and made my coming to Hamburg possible. It was great to work with the original founders of this project and follow in their footsteps.

I am grateful to our HiSCORE group members Rayk Nachtigall and Maike Kunnas, with whom I shared office during these three years. I also take this opportunity to express gratitude to all the members of the astrophysics group in Hamburg for their help and support.

My sincere thanks also go to my supervisor Vasily Prosin and to the leader of the Tunka-133 collaboration Leonid Kuzmichev, which do everything in order to implement the project HiSCORE. They taught me and always participated in all my scientific activities all the time since my days in Moscow State University.

I am very happy that the HiSCORE concept has found its place in the complex experiment TAIGA under the leadership of Razmik Mirzoyan.

I thank my parents and my lovely wife Sasha, that all this time believed in me. They were always there cheering me up and stood by me through the good and bad times.

I also place on record, my sense of gratitude to one and all, who directly or indirectly, have lent their hand in this venture.

Contents

Chapter 1

Introduction

Ground-based gamma ray astronomy has come a long way from the detection the first gamma ray source, the Crab Nebula, in early 1989 by the Whipple Telescope [1] to observations of more then hundred local sources above 1 TeV with the third generation of imaging atmospheric Cherenkov telescopes (HESS [2], MAGIC [3], VERITAS [4]).

Sensitivity of the existing and the currently planned gamma ray telescopes is optimized for the energy range 100 GeV – 20 TeV. Despite a significant number of sources in the TeV energy range were detected, only 10 exceed the energy of 10 TeV, and none was detected above 100 TeV.

The upcoming telescopes (CTA [5], HAWC [6], LHAASO [7]) will improve our knowledge about very-high-energy gamma rays. However, the limited area of these arrays ($0.1 - 1\,\mathrm{m}^2$) makes it difficult to access the energy range above 100 TeV.

In all these experiments gamma rays are detected by registering secondary particles from the extensive air showers (EAS) initiated by various primary particles in the atmosphere. Either the Cherenkov light component or charged particles can be used for the detection. The most efficient type of gamma ray telescope is the imaging atmospheric Cherenkov telescope (IACT). Such a telescope has a narrow field of view and consists of a mosaic of photomultipliers placed in the focus of the mirror. The mirror reflects Cherenkov light onto the mosaic creating an image of the shower. The method based on the analysis of the image shape proposed by Anthony Hillas [1] allows with high reliability to separate the showers initiated by gammas from the showers initiated by hadrons.

The modern Cherenkov arrays are composed of 2–4 telescopes with a mosaic of $\sim$ 1000 photomultipliers each. To cover an instrumental area of 1 km^2 one needs about 10 mirrors and about 10000 photomultipliers (10000/km^2). Further area increase, say 10 times, is practically impossible due to financial reasons.

An alternative approach would be the registration of Cherenkov light from air showers without creating the image (*non-imaging*). Such an array may consist of a network of wide-angle Cherenkov optical stations ($\sim$ 1 sr). To cover an area of 1 km^2 one needs about 100 stations (100/km^2). This allows to build an array with an instrumental area of 10–100 km^2.

Such a technique has been successfully used for gamma ray studies in the past by AIROBICC [8]. Following this experience, a similar approach is also used for cosmic rays studies in the Tunka experiment since many years [9].

A project of non-imaging wide-angle Cherenkov array **HiSCORE** (**H**undred****i** **S**quare km **C**osmic **O**rigin) was initiated in Spring 2008 with the main goal of investigating the gamma ray sky in the energy above 10 TeV and cosmic rays above 100 TeV [10]. This experiment might be the first to detect gamma ray sources in the PeV energy range (*pevatrons*).

A 9-station engineering array with an instrument area of 0.09 km^2 has been deployed in October 2013 at the Tunka-133 array site in Russia [11]. The experimental data of the first season (2013–2014) have been taken and an analysis will be presented in this work.

In 2014 the array was enlarged and now it comprises 28 stations with an area of 0.25 km^2. Moreover, HiSCORE detectors will be complemented with wide-angle imaging telescopes and charge particle detectors within the framework of the **TAIGA** experiment (**T**unka **A**dvanced **I**nternational **G**amma-ray and **C**osmic ray **A**strophysics) [11].

Chapter 2

From cosmic rays to gamma astronomy

Since the cosmic rays were discovered in 1912 by Victor Hess they are still subject of intense research. Some open questions in cosmic ray physics so far remain unanswered and the main question — the origin of cosmic rays.

Cosmic rays (CR) are particles entering the Earth atmosphere from outer space originated substantially beyond the Solar System. They are mostly ionised atomic nuclei with a small fraction of electrons and positrons as well as gammas and neutrinos. The charged particles are deflected by irregular magnetic fields so that it becomes difficult to determine the direction of arrival and identify the source. However, measurements of the spectra and the composition of cosmic rays allows to draw conclusions on their acceleration mechanisms and diffusion in the interstellar medium. As opposed to that, the local sources can be observed by means of neutral particles, which are gammas and neutrinos.

2.1 Cosmic rays

Investigation of cosmic rays is a complex experimental and theoretical problem. Due to the low intensity of cosmic rays at high energies ($> 10^{14}\,\mathrm{eV}$) the indirect detection with ground-based arrays can only be used. On the other hand, the data interpretation is based on Monte Carlo simulations (MC). Modern accelerators, such as the Large Hadron Collider (LHC) and the Tevatron, used to investigate

particle interactions, end at the equivalent energies of $10^{16} - 10^{17}$ eV, while cosmic rays reach few 10^{20} eV. A detailed review of cosmic ray theory can be found in the literature [12]. Here some aspects will be briefly outlined.

2.1.1 Primary spectrum

The all-particle primary energy spectrum extends over many orders of magnitude up to at least 10^{20} eV, indicating non-thermal origin (Fig. 2.1). This spectrum represents the flux of cosmic rays as a function of energy and follows a power law

$$\frac{dN}{dE} \propto E^{-\gamma}, \tag{2.1}$$

with the spectral index γ.

The spectrum has three remarkable features. The spectral index changes from –2.7 to –3.2 at about 3–5 PeV[1] (*knee*), then the spectrum steepens slightly around 400 PeV (*2nd knee*) and flattens at the highest energies around 10 EeV (*ankle*). The knee was first observed by the Moscow state university group in the electromagnetic component more than 40 years ago [14], and has been confirmed by many experiments in other components of extensive air showers.

The knee can be interpreted as a maximal energy for protons up to which they can be accelerated in the Galaxy, while the second knee represents the end of the iron component ($E_c^Z = Z \cdot E_c^p$). The ankle is usually interpreted as a feature caused by transition from galactic to extragalactic cosmic rays [12].

The flux of cosmic rays drops rapidly with energy. For a detector with an aperture of 1 sr, the integral flux of cosmic rays above the knee is typically one particle per square metre per year, while for the highest energy cosmic rays above the ankle the event rate falls to one particle per square kilometre per century (!).

The all-particle spectrum at low energies is measured reliably with balloon experiments and satellites. Since the effective area of such detectors is very limited, cosmic rays above 10^{14} eV can only be accessed using indirect experiments.

The spectrum at highest energies ($\sim 6 \cdot 10^{19}$ eV) is predicted to be suppressed due to interaction of cosmic rays with the cosmic microwave background radiation.

[1] SI unit prefixes commonly used in this thesis: GeV = 10^9 eV, TeV = 10^{12} eV, PeV = 10^{15} eV, EeV = 10^{18} eV.

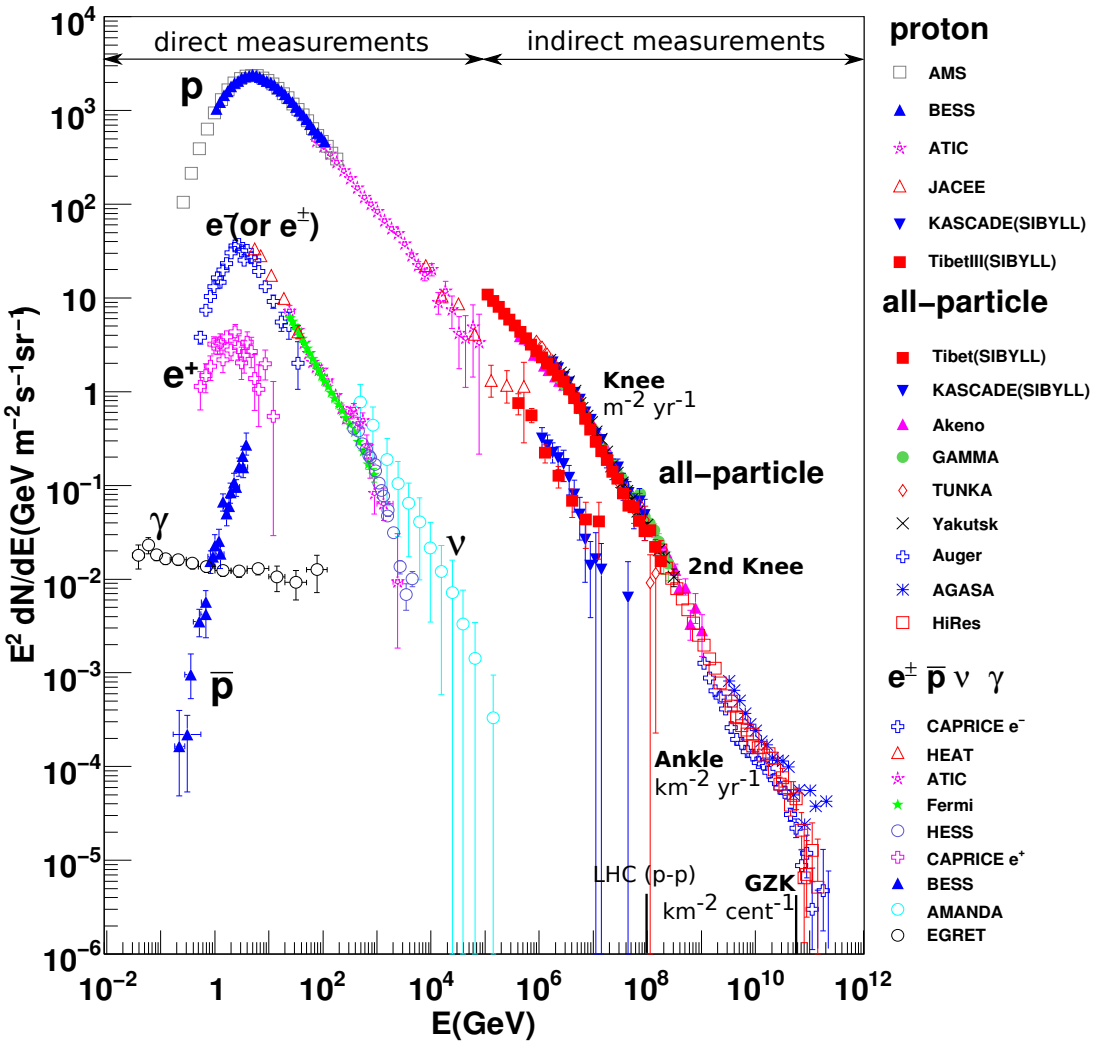

FIGURE 2.1: All-particle energy spectrum of cosmic rays and spectra of various components (adapted from the compilation [13]). The corresponding LHC energy ($\sqrt{s} = 14\,\text{TeV}$) is shown for reference.

This is the so-called GZK-cutoff ([15],[16]). The question whether the cutoff is being observed in the spectrum of cosmic rays is still speculated [17].

2.1.2 Composition

Overall energies cosmic rays are mostly protons (87%) and helium nuclei (12%) with small amounts of heavier elements [18]. Electrons, positrons account for 1–2% of the cosmic rays. Above $10^{12}\,\text{eV}$, the composition changes to about 50% protons, 25% helium, 13% CNO, and 13% iron [19]. Composition of cosmic rays is shown in Fig. 2.2.

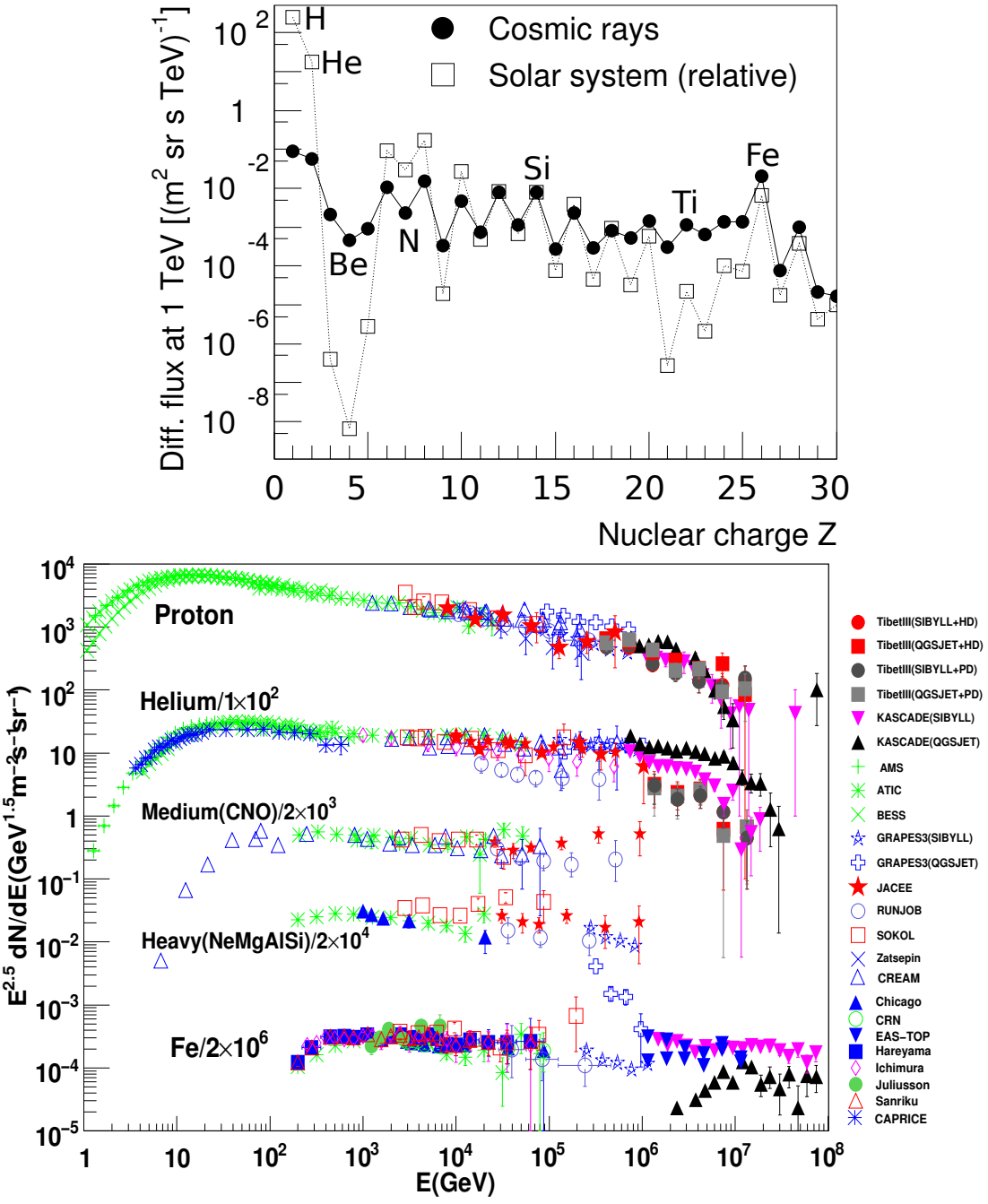

FIGURE 2.2: *Top:* Abundance of elements ($Z < 28$) in cosmic rays at 1 TeV. For comparison, abundances in the Solar System are presented as well (adapted from [20]). *Bottom:* Compilation of cosmic ray spectra for different mass groups (adapted from [13]).

Cosmic rays at low energies are present in about the same relative abundances as in the Solar System with some exceptions. H and He are under-abundant in cosmic rays, the light elements Li – B and the sub-iron elements Sc – V are over-abundant. A way to explain the composition of cosmic rays is to assume that the relative abundances reproduce the average galactic composition except that heavy nuclei spallate into lighter nuclei when they propagate through the interstellar medium. Elements more massive than iron were found to be very rare.

Mass composition of cosmic rays for energies above 10^{15} eV is only accessed via ground-based arrays. Unfortunately the measurement of primary masses is the most difficult task in air shower physics because the data interpretation is based on Monte Carlo simulations. Sensitivity of shower parameters to the primary mass is low. The main uncertainties come from hadronic interaction models basically because the energy range of interest is much beyond the energy of particle accelerator experiments. However, the recent data by the LHC provide an important improvement of existing high-energy interaction models and have been awaited with great interest.

The essential feature of the cosmic ray acceleration and their propagation in interstellar fields is the dependence on the magnetic rigidity[2]. This leads to the fact that whatever the mechanism of the knee formation in the spectrum of cosmic rays is, above the knee the composition is expected to become heavier. This prediction is convincingly confirmed by the experiments registering charged particles EAS-TOP [21], KASCADE [22] and MSU [23] as well as the Cherenkov experiment Tunka [24]. However, the estimates on the mass composition in various experiments are still far from agreement [12]. For this reason, the composition of cosmic rays is the problem that had not yet been fully resolved.

There are mostly two observables sensitive to the mass of the primary particle: the ratio of the number of electrons to muons (N_e/N_μ) and the depth of the shower maximum (X_{max}).

The N_e/N_μ method employs a two-dimensional unfolding technique, first utilized by KASCADE [25] and later by KASCADE-Grande [26]. It allows to reconstruct energy spectra for various mass groups (usually up to 5). Unfortunately the data interpretation depends on a chosen high-energy interaction model used in Monte Carlo simulations.

[2]Rigidity is defined as particle momentum divided by its charge p/Z

Alternatively, the mass composition can be accessed with the depth of the shower maximum X_{max}. Such techniques are used in Cherenkov or fluorescence experiments. This observable in turn depends on the hadronic interaction models to a lesser extent. The data of the mean shower depth $\langle X_{max} \rangle$ are usually interpreted in terms of the mean logarithmic mass $\langle \ln A \rangle$. As seen from Fig. 2.3, the composition trends a gradual increase of the average logarithmic mass of cosmic rays between 10^{15} eV and 10^{17} eV followed by a transition towards a lighter composition during the next decade. Most likely, above the ankle the composition becomes again heavier up to GZK energies. The region from 10^{17} to 10^{18} eV may confirm the transition from galactic to extragalactic acceleration.

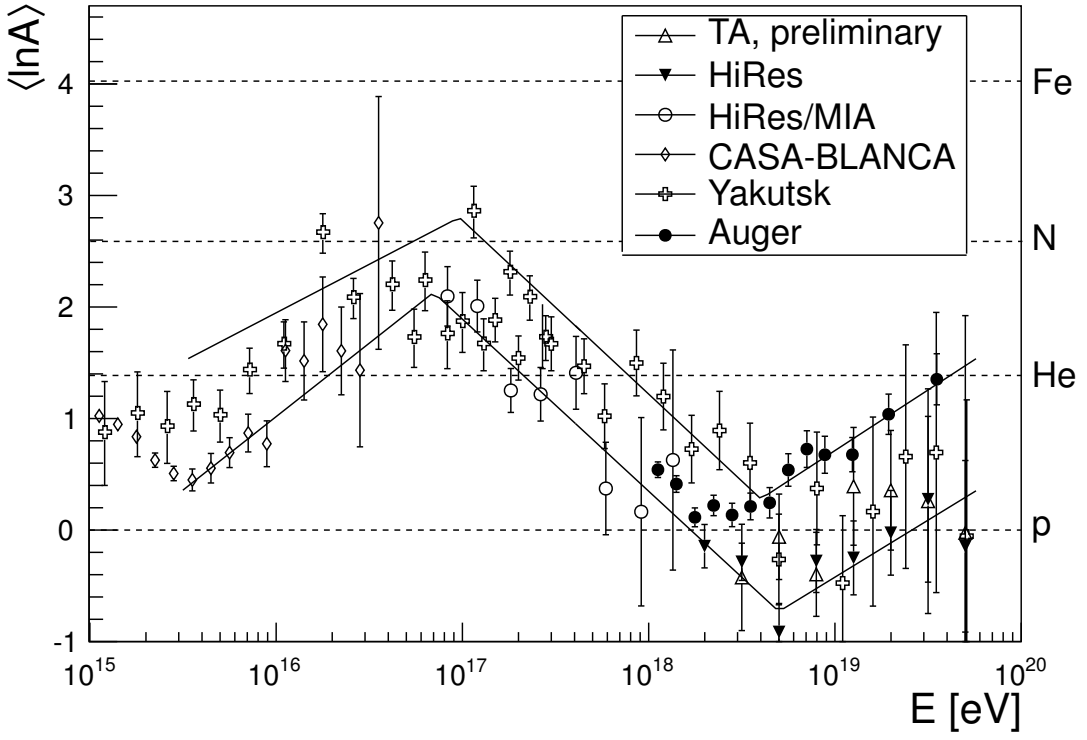

FIGURE 2.3: Mean logarithmic mass of cosmic rays as a function of energy derived from X_{max} measurements with surface optical detectors for the QGSJET01c interaction model (based on [27]). Lines show the experimental systematics.

2.2 Gamma astronomy

Energetic neutral particles, such as gammas and neutrinos, allow to identify possible sources of cosmic rays. As a result, a significant amount of gamma ray sources

in different energy ranges up to tens TeV have been found in the past and could be identified with known astronomical objects.

Gamma rays below hundreds GeV directly can be detected with satellites. First observations of gamma ray sky above 100 MeV were carried out by the Energetic Gamma Ray Experiment Telescope (EGRET) [28]. As a result, the 271 sources have been detected. EGRET was a predecessor of the modern Fermi-LAT telescope [29], which has successfully detected to date about 3000 gamma sources within the energy range from 100 MeV to 300 GeV.

Gamma rays in this range are dominated by galactic diffusive emission that is particularly bright along the plane of the Galaxy (Fig. 2.4). This emission is generated primarily by energetic cosmic rays (electrons and protons) that interact with interstellar gas and radiation fields [30]. Furthermore the Fermi-LAT has observed a large number of sources that include active galaxies, pulsars, compact binaries, globular clusters, and supernova remnants.

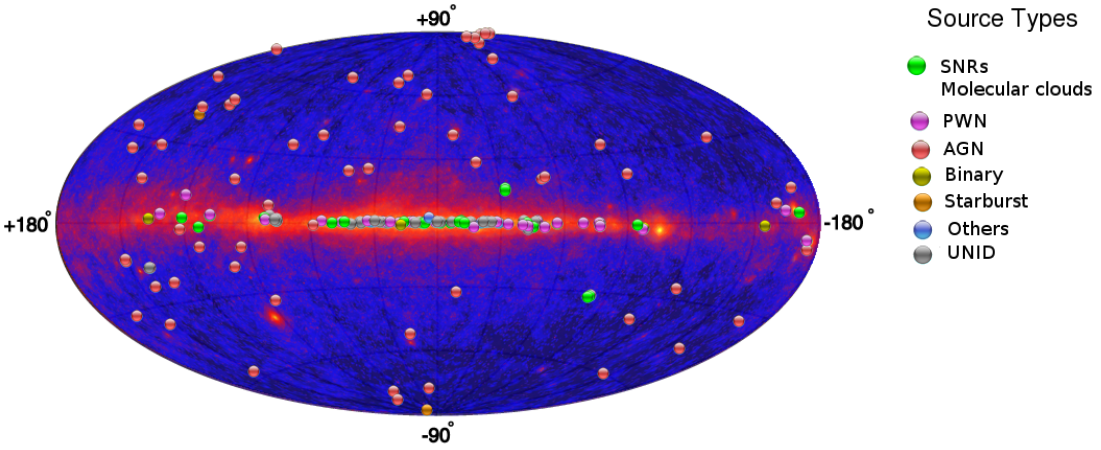

FIGURE 2.4: Known TeV gamma ray sources (blobs) combined with Fermi-LAT skymap (TeVCat catalogue [31]).

Gamma rays in the TeV energy range can only be accessed with ground-based arrays. Back in 1989, TeV-astronomy started with the detection of the first source, Crab Nebula, by the imaging Cherenkov telescope Whipple [1]. Not less interesting gamma ray observations have been also made in the past by non-imaging wide-angle telescopes, such as Milagro [32], ARGO-YBJ [33] and Tibet [34].

A great success has been achieved in this direction only recently. All known TeV sources were mostly detected by the imaging Cherenkov telescopes: HESS [2], MAGIC [3] and VERITAS [4]. The discovery of such sources belongs to the most

remarkable achievements of the last decade in astrophysics [35]. The implications of the results obtained with ground-based TeV gamma-ray detectors are vast. They have the strong impact on key problems of modern astrophysics and cosmology. The number of TeV sources observed to date is 129 (Fig. 2.4). They can be associated with various galactic as well as extragalactic astronomical objects:

TABLE 2.1: TeVCat default catalogue [31].

Source class	Number of TeV sources
supernova remnants and molecular clouds	20
pulsar wind nebulae	28
active galactic nuclei	45
binary systems	5
starburst galaxies	2
other sources	7
unidentified sources	22
total	**129**

2.2.1 Gamma ray sources

Supernova remnants. Massive stars may end their life with a supernova explosion forming supernova remnants (SNRs) (Fig. 2.5). Diffusive shock acceleration (DSA) mechanism at shock fronts [36, 37] makes it possible to accelerate particles (hadrons and leptons) to extremely high energies. Supernova remnants are good candidates to explain the population of cosmic rays in the Galaxy up to energies beyond the knee.

In the TeV range, presently 12 shell-type SNRs have been firmly identified [31]: RX J1713.7-3946, Cassiopeia A, RX J0852.0-4622, CTB 37B, IC 443, HESS J1731-347, RCW 86, SN 1006 SW, SN 1006 NE, SNR G106.3+02.7, Tycho, SNR G015.4+00.1.

Molecular clouds. An attractive evidence for acceleration of cosmic rays in supernova remnants comes from studies of emission in the TeV range from dense interstellar medium. Molecular clouds (MC) close to SNRs are expected to emit gamma rays due to cosmic ray interactions in the magnetized gas, and an characteristic hadronic shape of the emission spectrum should be observed [39]. Very often in these objects the spectral cut-off is not present, at least up to energies 20 TeV (Fig. 2.6).

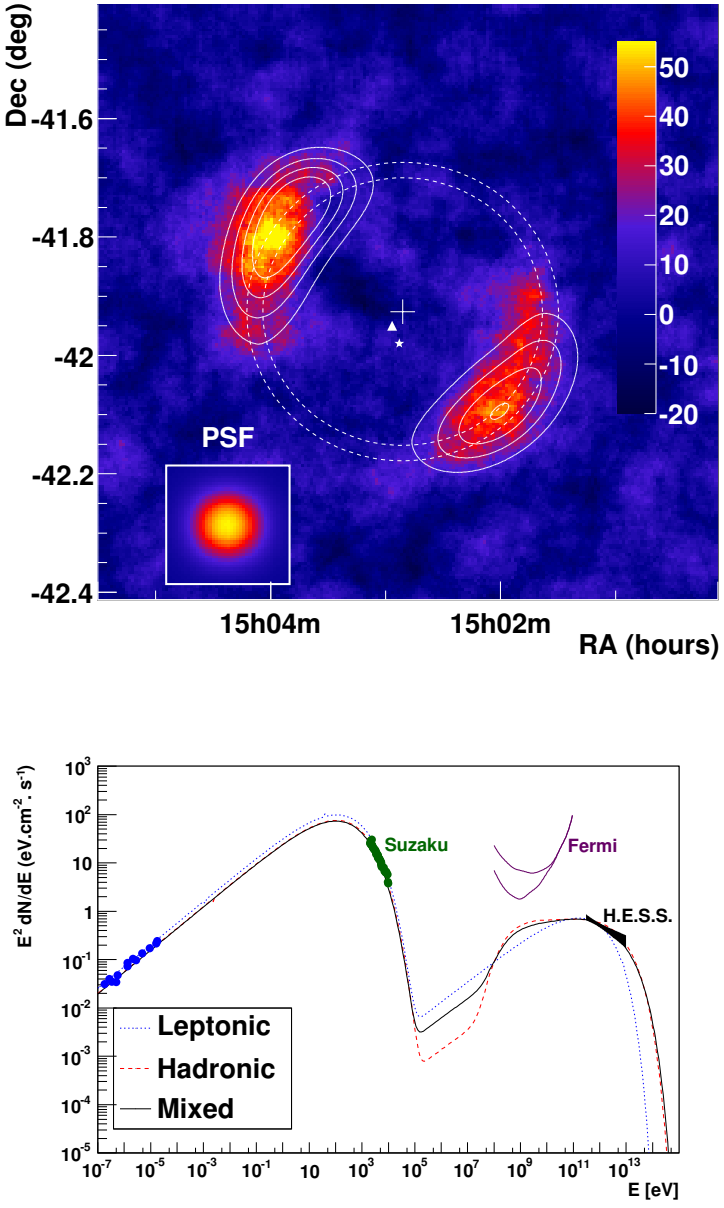

FIGURE 2.5: Probing the acceleration mechanisms for the supernova remnant SN 1006. *Top:* HESS gamma rays correlated excess map of SN 1006. *Bottom:* Spectrum predicted for SN 1006 for three different emission models. Figures from [38].

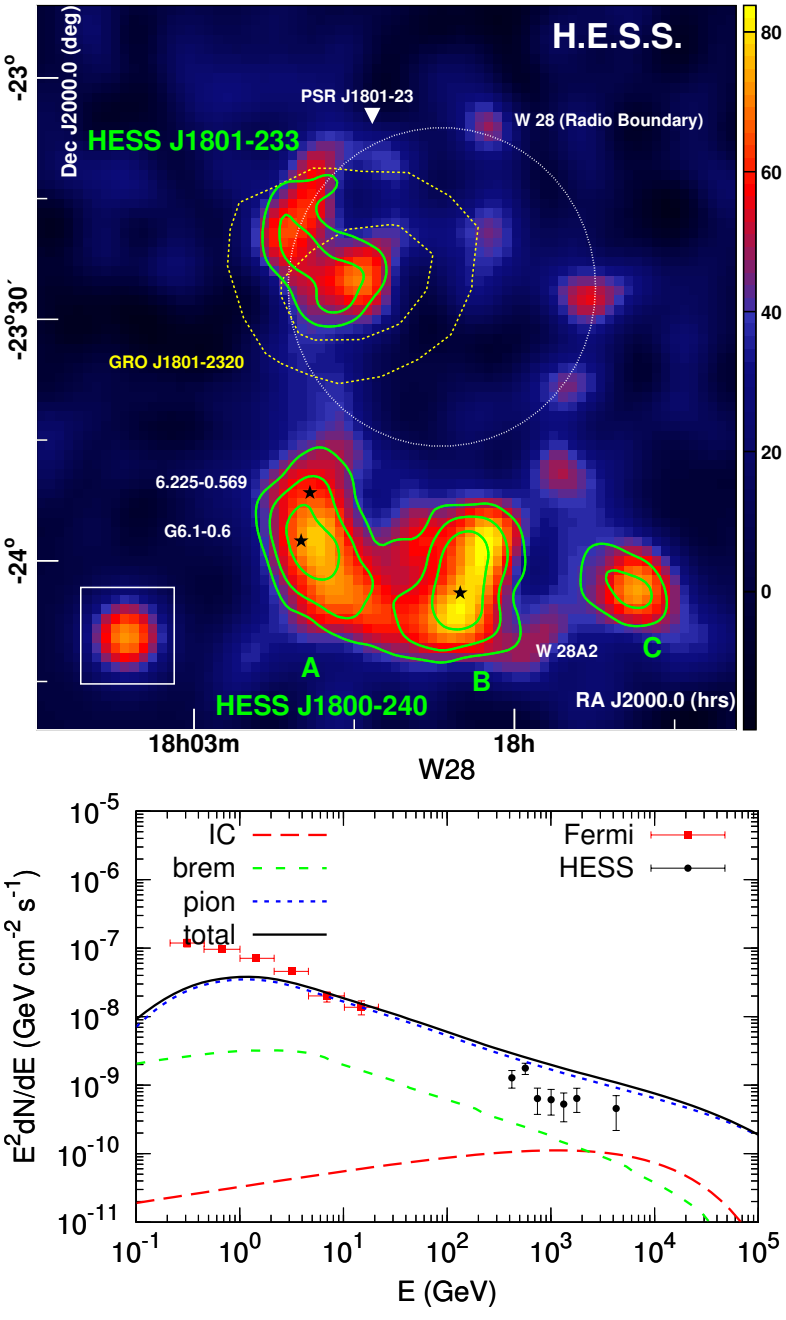

FIGURE 2.6: *Top:* SNR-MC interacting system W28 [38]. *Bottom:* Predicted gamma ray spectrum [40].

The number of such sources to date is 8. They are: HESS J1745-303, W 28, HESS J1800-240A, HESS J1800-240B, W 51, CTB 37A, SNR G349.7+00.2, LMC N132D.

Pulsar wind nebulae. The largest class of identified Galactic TeV gamma ray sources is pulsar wind nebulae (PWN). PWN can be often found inside the shells of supernova remnants or around older pulsars whose supernova remnants have disappeared. A classical pulsar wind nebula is the Crab Nebula. Although in such systems gamma emission is caused by mainly inverse Compton scattering of electrons, the hadron component in the wind is not excluded. However, there were no indications obtained so far. If the gamma emission from hadrons is present, it must occur at higher energies [41].

Active galactic nuclei. Most of the extragalactic objects observed in the TeV range are active galactic nuclei (AGN). The radiation from AGN is believed to be a result of accretion of mass by a supermassive black hole at the centre of its host galaxy. This process forms a narrow collimated plasma flows along the axis of rotation of the black hole — relativistic jets. According to the unification model of AGNs [42], different extragalactic objects can be attributed to different orientations to the observer (Fig. 2.7). At large distances from the galaxy, the jet interacts with the intergalactic gas and forms relativistic shock waves which may accelerate particles [43]. These energetic sources are best candidates to explain the cosmic ray population above 10^{18} eV in the Metagalaxy. The study of extragalactic sources in gamma ray astronomy, in fact, supports this assumption with the main role of AGN in the formation of extragalactic cosmic rays. However, this hypothesis is not confirmed experimentally yet.

Dark accelerators. A large part of the TeV sources show no clear counterparts in lower-energy wavebands and remain unidentified. Understanding the emission mechanisms in these sources is a challenge for multi-wavelength astronomy [38].

2.2.2 Imaging Cherenkov gamma ray telescopes

Very-high energy gamma rays above $50 - 100$ GeV are being investigated mostly since 2003–2004 by means of ground-based imaging arrays of Cherenkov telescopes.

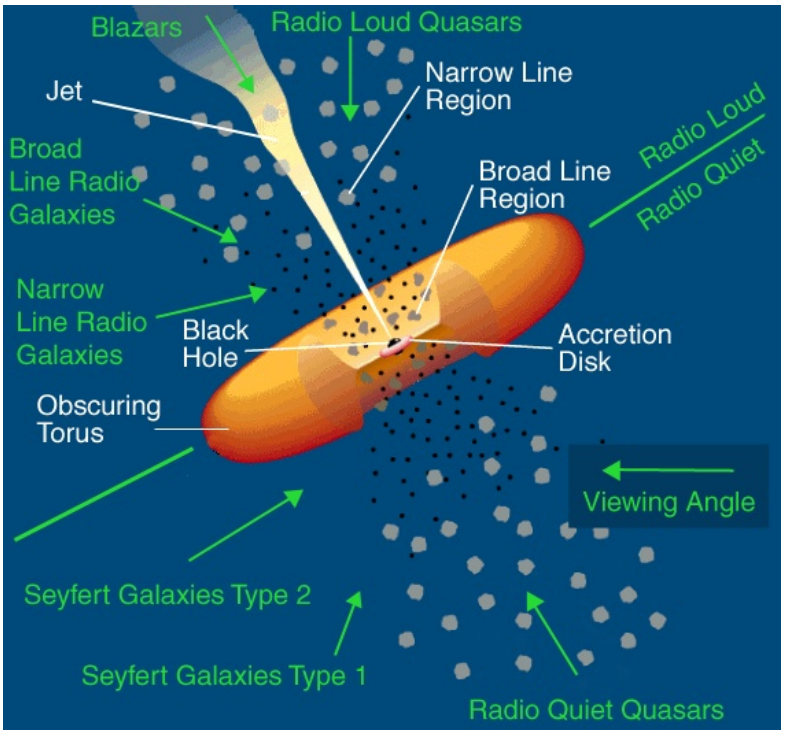

FIGURE 2.7: The unification model of AGNs [44]). Detailed view shows the class objects as function of viewing angle.

They are the High Energy Stereoscopic System (H.E.S.S.) [2], the Major Atmospheric gamma ray Imaging Cherenkov Telescopes (MAGIC) [3] and the Very Energetic Radiation Imaging Telescope Array System (VERITAS) [4]. These arrays consist of 2–4 telescopes with a spacing of 80–120 m. Each telescope is usually equipped with a tessellated mirror (12–17 m in diameter) focusses Cherenkov light on a focal plane covered by a mosaic of photomultipliers (500–1000 PMTs). The stereoscopic approach allows to substantially improve the background rejection and the angular resolution. Such narrow-angle telescopes have a field-of-view of $3-5^{\circ}$ and allow to explore gamma ray sources with intensities at a level of 1/100 of the Crab Nebula flux in 50 hrs (Crab at 5σ in 30 sec) up to an energy of 10–80 TeV with an angular resolution of 0.1° and an energy resolution of 15%. IACT telescopes have a high gamma/hadron rejection power. The duty cycle observations with Cherenkov light is limited to 10% because the telescope can operate during clean moonless nights only.

A new Cherenkov telescope array (CTA) is planned to be deployed in the nearest future [5]. The project intends to improve the sensitivity for gamma ray detection by an order of magnitude. The observatory will consist of two arrays located in both hemispheres in order to provide all-sky coverage. CTA plans the construction

TABLE 2.2: Properties of current generation of IACT telescopes. Adapted from [45].

Telescope	Location	Alt. (m)	N_{tel}	A_{tel} (m^2)	FoV (°)	E_{th} (TeV)	S_γ (% Crab)
HESS I	23°S, 17°E	1800	4	107	5	0.1	0.7
MAGIC I+II	28°N, 18°E	2200	2	234	3.5	0.03	1.0
VERITAS	32°N, 111°W	1300	4	106	3.5	0.1	0.7

of many tens of telescopes divided in three kinds of configurations to operate in the energy range from 30 GeV to 100 TeV. The angular resolution is expected to be 0.05° at an energy of 1 TeV and to have an energy resolution of 10%. The south part will cover 3 km^2 with 60 telescopes while the north part will cover 1 km^2 with 30 telescopes.

2.2.3 Non-imaging gamma ray telescopes

High-energy gamma rays can also be detected by high-altitude wide-angle arrays registering charged particles from air showers. The next generation of such experiments will be represent by two instruments: The High Altitude Water Cherenkov (HAWC) experiment in Mexico (4300 m a.s.l.) [6] and The Large High Altitude Air Shower Observatory (LHAASO) in China (4400 m a.s.l.) [7]. Design of such arrays allows to detect TeV gamma ray sources in the energy range from 300 GeV to 100 TeV at a typical level of mCrab in one year (Crab at 5σ in 1 day) with a modest resolution (0.1–0.5°, $\Delta E/E \geq 30-50\%$), but exhibiting a high duty cycle ($> 90\%$) and a wide field of view (1–2 sr).

The HAWC experiment follows the detection of gamma rays with the water Cherenkov technique that was pioneered by Milagro. HAWC consists of water tanks with a total area of 22,000 m^2. Water detectors are used to sample the charged particles created in the air showers. Charged particles pass through the detector volume and emit Cherenkov radiation which can be observed.

In contrast, LHAASO is a complex array, and at the first stage it will consist of three parts: a 1 km^2 scintillator array (LHAASO-KM2A) with a small shower core detector array (SCDA), 4 water Cerenkov detector arrays (WCDAs) with area of 22,500 m^2 each, 24 wide-angle air Cherenkov detectors (WFCA). At the second stage it is planned to be equipped with two IACT telescopes.

Comparison between different EAS techniques is summarised in the following table (adopted from [46]):

Method	E_{th}	$\Delta\theta/\theta$	$\Delta E/E$	$Q_{\gamma/h}$	duty cycle
Particles					
scintillator detectors	3 TeV	$\sim 1^\circ$	$30-50\%$	~ 1	100%
water tanks	100 GeV	$\sim 0.5^\circ$	$30-50\%$	~ 6	100%
Cherenkov light					
imaging	5 GeV	$\sim 0.1^\circ$	$10-15\%$	~ 6	10%
non-imaging	10 TeV	$\sim 0.1^\circ$	$10-15\%$	$\sim 1.5-2$	10%

2.3 The HiSCORE experiment

2.3.1 Experiment motivation

Gamma rays with energies above 10 TeV were detected from only 10 sources by now and none was detected with energies beyond 100 TeV. Although the use of imaging telescopes brought unprecedented success, this experiments have a number of serious limitations to extend their energy range and the main one is the limited instrumental area. Sensitivity of presently existing telescopes (HESS, MAGIC VERITAS) is optimized for the energy range 100 GeV – 20 TeV. To cover an instrument area of 1 km^2, such an approach will require to use, say, a net of 10 telescopes and about 10000 photomultipliers (10000/km^2). Further increase of the area by an order of magnitude is practically impossible due to financial reasons. The new experiments (CTA, HAWC, LHAASO) with a limited area of 0.1 – 1 km^2 will probably access the energy range up to 100 TeV. However, the range beyond 100 TeV is of considerable interest.

If the knee energy range up to 10^{17} eV characterises a maximal acceleration limit of nuclei in the Galaxy, there must be sources that accelerate cosmic rays up to PeV energies: *pevatrons* [47]. Such pevatrons is expected to have gamma ray spectra up to several 100 TeV [48]. As mentioned above, good candidates for acceleration of Galactic cosmic rays are supernova remnants. However, in the TeV energy regime, the observed emission from SNRs is ambiguous since it can be explained in both leptonic and hadronic scenarios [49]. This ambiguity disappear above 10 TeV, where the leptonic radiation is highly suppressed (Klein-Nishina regime).

Thus, a hard gamma ray spectrum continuing up to few hundred TeV would be a clear signature of hadronic acceleration.

An addition argument supporting the hadronic nature of the gamma-ray emission will possibly come from the direct detection of neutrinos from SNRs. They are expected to be produced during the same hadronic interactions responsible for the production of gamma rays [48]. As a result, the first astrophysical PeV-neutrinos were observed recently by IceCube [50], but it is too early to draw any conclusions on their origin.

2.3.2 Detector concept

An alternative would be to register the Cherenkov light in a sampling mode without the imaging. Such an array may consist of a network of wide-angle Cherenkov optical stations ($\sim$1 sr). To cover an area of 1 km^2 one needs about 100 stations (100/km^2). This approach was first employed in the AIROBICC experiment 20 years ago [8]. This allows to build an array with an instrumental area as large as 10 – 100 km^2.

A new project of a wide-angle non-imaging gamma ray telescope **HiSCORE** (**H**undred*__i__ **S**quare km **C**osmic **O**rigin) was proposed in 2008 [10]. It stands for investigating the gamma ray sky in the energy above 10 TeV and cosmic ray studies above 100 TeV. A net of such detectors will cover an area up to 100 km^2. The expected array sensitivity is shown in Fig. 2.8.

The following problems are addressed to the HiSCORE project:

1. Gamma ray sky above 30 TeV.
2. Cosmic ray spectrum and composition above 100 TeV.
3. Gamma-ray propagation and searches for a new physics.

The array was decided to be deployed at the site of the existing Cherenkov experiment Tunka-133 in Russia. It is expected, that with the HiSCORE array about 30 known gamma ray sources can be observed in the northern hemisphere [52, 53]. They are the following.

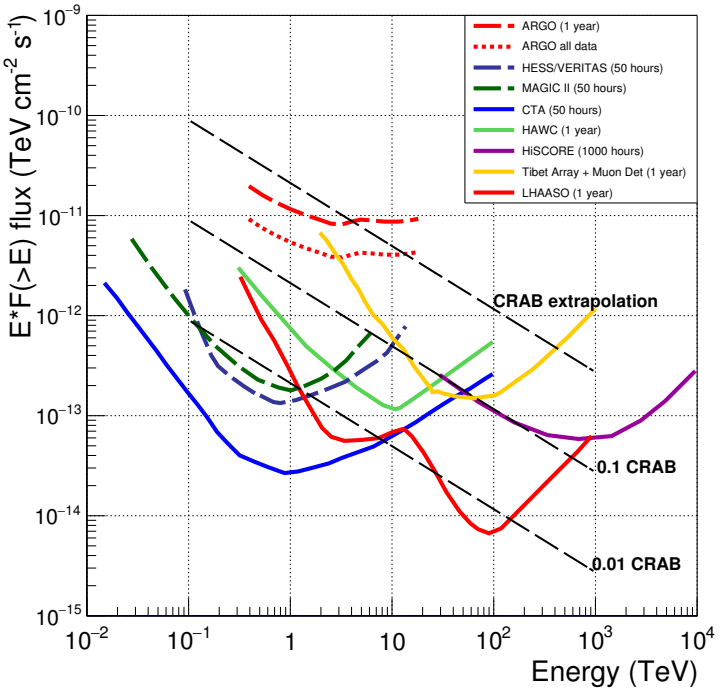

FIGURE 2.8: Sensitivity of ground-based gamma-ray detectors to a Crab-like point source [51].

Supernova remnants and molecular clouds: Tycho, IC443, W51, J1954+286, Cas A. Pulsar wind nebulae: Crab, J0631+105, Geminga, HESS J1912+101, SNR G054.1+00.3, J1958+284, MGRO J2019+37, J2021.5+4026, J2032+4130, Boomerang, CTA1. Active galactic nuclei: Mkn421, M87, Mrk501, 1ES 2344+514. Starburst: M82. Unidentified sources: MGRO J1908+06, MGRO J2031+41.

A 9-station engineering array with an instrument area of 0.09 km^2 has been installed in October 2013. As a result, the experimental data of the first season (2013–2014) have been collected and an analysis of the data will be presented in this work.

In 2014 the array was further increased. Now it consists of 28 stations and covers an area of 0.25 km^2. Furthermore, the HiSCORE array now is a part of a complex experiment **TAIGA** (**T**unka **A**dvanced **I**nternational **G**amma-ray and **C**osmic ray **A**strophysics) [11], where non-imaging HiSCORE detectors will be complimented with imaging telescopes and detectors of charged particles.

Chapter 3

Atmosheric Cherenkov technique

In 1947 Patrick Blackett suggested that Cherenkov radiation emitted by high-energy cosmic rays should contribute to the light of the night sky. Five years later, in 1952, the first Cherenkov light was sucessfully detected by Galbraith and Jelley. Since then the Cherenkov light was used to study properties of air showers, and starting from 70s, Cherenkov telescopes were used to search for high-energy gamma rays.

3.1 Extensive air showers

Energetic cosmic rays entering the Earth's atmosphere initiate there cascades of particles, called extensive air showers (EAS). Each shower produces a large number of secondaries as well as electromagnetic radiation: Cherenkov, fluorescence and radio. As a result, a single primary creates a shower that can be detected at the ground level.

3.1.1 Electromagnetic shower

An electromagnetic primary (γ or e) induces in the atmosphere a shower dominated by electromagnetic interactions, called *electromagnetic shower*. Such an cascade consists mainly of electrons (e^- and e^+) and gammas. The secondary electrons produce highly energetic photons through bremsstrahlung, which in turn give new electron-positron pairs through pair production (see Fig. 3.1 (a, c)). The average

energy of the secondary particles will decrease with height due to further reaction and inelastic scattering. The number of secondaries increases until the particle energy becomes low enough to stop further multiplication. The point where the number of charged particles becomes maximal called *shower maximum*. From this point the shower decays slowly through ionisation losses for electrons and Compton scattering for photons.

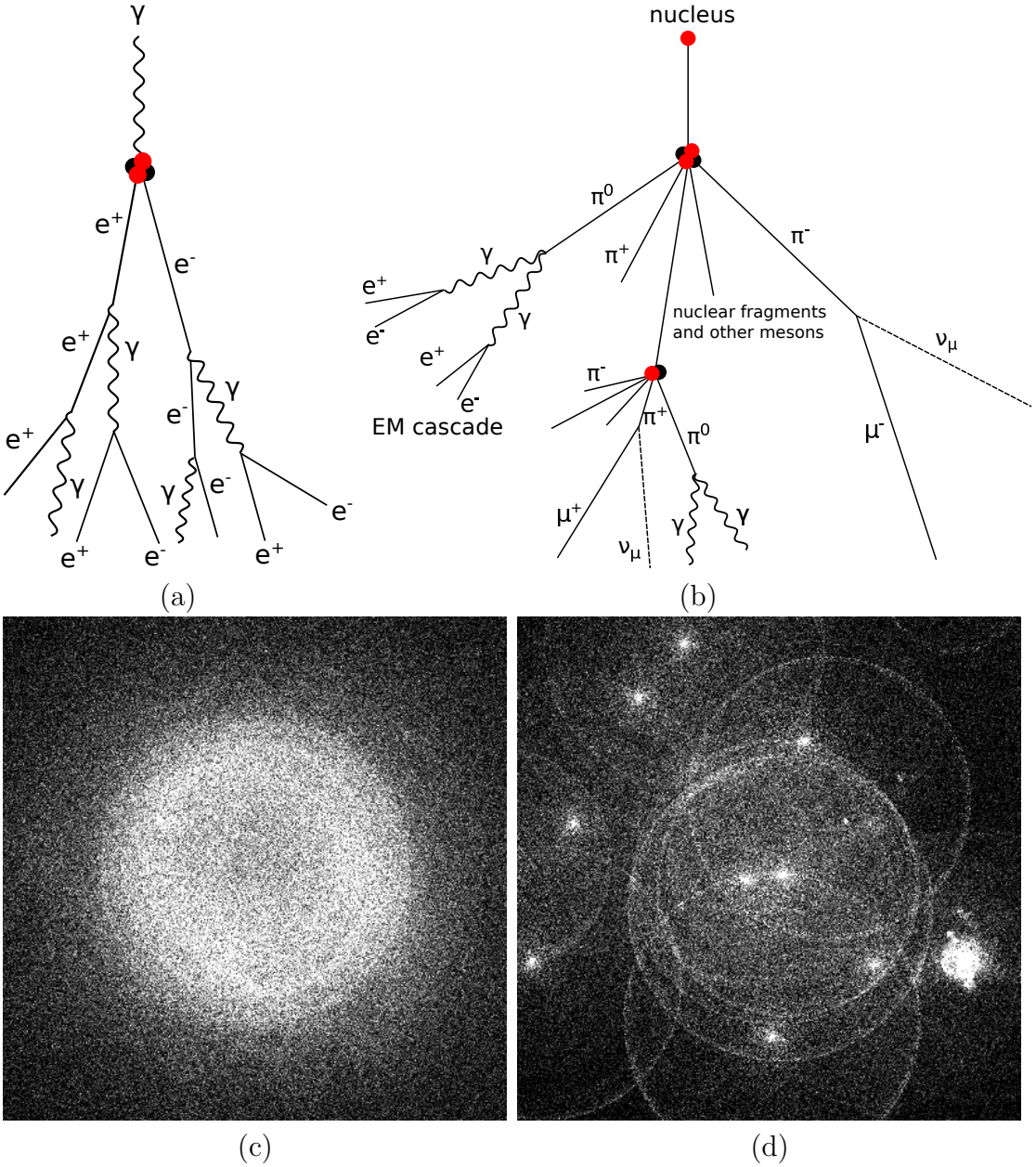

FIGURE 3.1: *Upper panel*: Schematic model of air shower development generated by a gamma (a) and a hadron (c). *Lower panel*: Lateral distribution of Cherenkov light of air showers at the ground level initiated by a vertical gamma of 300 GeV (b) and by a vertical proton of 1 TeV (d) in $400 \times 400\,\mathrm{m}^2$ area. The lateral distributions were taken from [54].

3.1.2 Hadronic shower

In contrast, *hadronic shower* (Fig. 3.1 (b, d)) induced by a nucleus develops in a different way. Much of the incident energy is passed on to pions production with a small fraction of nuclear fragments and different mesons ($K^{\pm}$ and others). Such π-mesons will decay in the following sub-products:

$$\begin{aligned}
&\pi^0 \rightarrow \gamma\gamma, \\
&\pi^{\pm} \rightarrow \mu^{\pm}\nu_{\mu}, \\
&\qquad \hookrightarrow e^{\pm}\overline{\nu}_e\nu_{\mu}.
\end{aligned}$$

The process continues until the charged pions fall below the critical energy E_c where they cannot decay no more, yielding muons. The photons from π^0 decay originate electromagnetic sub-cascades in the shower (similar to electromagnetic shower) because from here only electron-positron pair production and secondary photons through bremsstrahlung will take place. Roughly 1/3 of the incident energy of the primary is passed into π^0 production.

3.2 Cherenkov emission from air showers

3.2.1 Cherenkov effect

Cherenkov light (Fig. 3.2) is emitted when a charged particle moves through a medium faster than the speed of light in the medium, i.e. if

$$v > \frac{c}{n} \text{ or } \beta = \frac{v}{c} > \frac{c}{n}, \tag{3.1}$$

where n is the refractive index of the medium. The light is produced along the particle track within the cone with a narrow opening angle given by

$$\cos\theta = \frac{c}{nv} = \frac{1}{n\beta}. \tag{3.2}$$

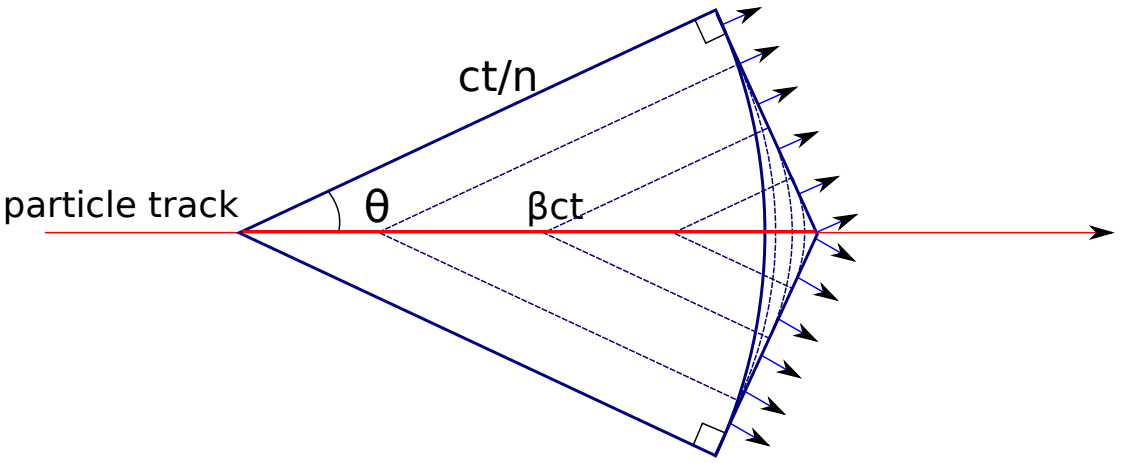

FIGURE 3.2: Cherenkov effect.

Furthermore, the light production is characterized by a minimal energy required to emit Cherenkov radiation and is defined by the equation

$$E_{th} = \frac{m_0 c^2}{\sqrt{1-\beta^2}} = \frac{m_0 c^2}{\sqrt{1-(1/n)^2}}. \tag{3.3}$$

The number of photons per unit of length produced by a particle with the charge Z can be calculated as

$$\frac{d^2N}{dxd\lambda} = 2\pi\alpha Z^2 \left(1 - \frac{1}{\beta^2 n(\lambda)^2}\right) \frac{1}{\lambda^2}, \tag{3.4}$$

where $\alpha \approx 1/137$ is the fine structure constant and $n(\lambda)$ is the refractive index. The formula reveals that the light yield is proportional to charge of particle Z in the power of 2. In the visible light regime, where $n(\lambda)$ is roughly constant, the Cherenkov light spectrum follows a $1/\lambda^2$ dependence, making Cherenkov light appear blue. Due to atmospheric absorption (Rayleigh scattering, aerosol and molecular absorption) Cherenkov light is attenuated in air and the Cherenkov spectrum will be slightly modified (Fig. 3.3).

The refractive index n is a function of atmospheric altitude h due to the density of air. With the assumption of an isothermal atmosphere one can use the barometric formula and obtain

$$n(h) = 1 + \eta_0 \cdot e^{-h/h_0}, \tag{3.5}$$

with η_0=0.00029 and h_0=7.1 km.

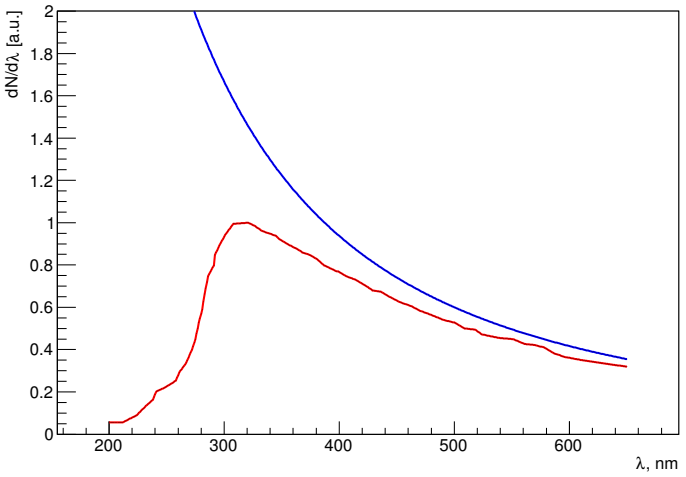

FIGURE 3.3: The intrinsic Cherenkov emission spectrum (*blue*), compared to the spectrum after attenuating with the atmosphere (*red*). Adopted from [55].

.

An ultrarelativistic particle ($\beta \approx 1$) with the charge $Z = 1$ moving through the air with a refractive index of 1.00029 at the sea level will produce 25 photons per metre for an wavelength interval of 300–700 nm within an angle of 1.4°. At a typical height of 8 km of the air shower maximum ($n = 1.00009$) the same particle will produce only 8 photons per metre within an angle of 0.8°.

Cherenkov light in the atmosphere is mostly produced by charged electromagnetic particles, such as electrons and muouns. According to Eq. 3.3, it results a minimal threshold of 21 MeV for electrons and 4.4 GeV for muons at the sea level. At a height of 8 km it leads to a threshold of 38 MeV for electrons and 7.9 GeV for muons.

3.2.2 Light distribution at the ground level

The light emitted from particles at different heights superimposes at the observation level. Such a light distribution at the ground level provides a key information about primary energy, direction and mass composition. Imaging atmospheric telescopes look at the shower within a narrow angle and can see the shower development projected onto the telescope camera with a high resolution (*image*). In

contrast, sampling arrays with a network of non-imaging detectors register integrated over the viewing angle Cherenkov light with large photomultipliers. Both approaches are illustrated in Fig. 3.4.

Shower sampling. Pulse forming in case of the shower sampling can be explained with a simple model. At large enough distances from the shower core, the shower can be considered as a point light source, moving with the speed of light c_{air} along the shower axis. Consider a right triangle with catheti H and r (Fig. 3.4 (*top*)), which are the height of emission and the distance to the detector. In that case, the time of arrival from the height H is given by the equation

$$\Delta t = \frac{1}{c_{air}}(\sqrt{H^2 + r^2} - H). \tag{3.6}$$

If $r \ll H_1$ and $r \ll H_2$, then the pulse duration τ between two points in time come from the different heights may be approximated as

$$\tau = \Delta t_2 - \Delta t_1 \approx \frac{r^2}{2c_{air}}(\frac{1}{H_2} - \frac{1}{H_1}), \tag{3.7}$$

where H_1 and H_2 are the heights from which the light come at the moments t_1 and t_2 respectively.

The pulse duration is sensitive to the longitudinal development of the shower, and, thus, to the position of the shower maximum X_{max}. In general, pulse width tends to be increased with r and it also decreases with the distance to the shower maximum.

Shower imaging. Shower image recorded by the camera of the imaging telescope can be parametrised with the so-called Hillas parameters [1]. Image analysis provides a very powerful method to discriminate gamma and hadron showers. Hadronic showers are basically less regular and have larger fluctuations, and, thus, the Cherenkov images of hadronic showers are mostly irregular in shape. On the contrary, Cherenkov images from gamma ray showers in camera are elliptical in shape and compact.

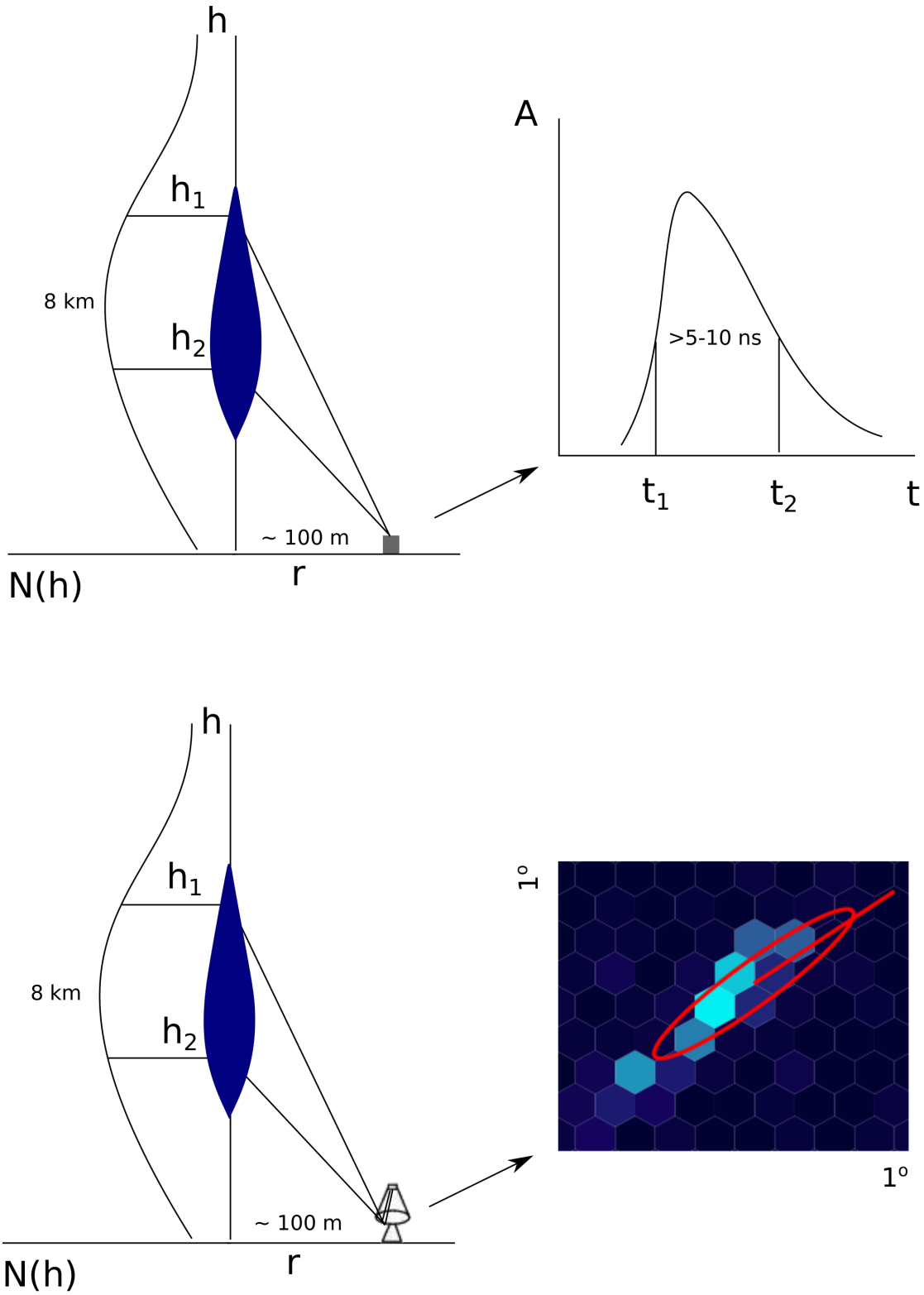

FIGURE 3.4: Formation of the Cherenkov light distribution at the ground level. Signals seeing by sampling array (*top*) and by IACT telescope (*bottom*) are shown.

3.3 Night sky background

One of the main problems in the detection of the atmospheric Cherenkov light is the night sky background (NSB). Its fluctuations limit a minimal Cherenkov yield, that can be detected, and thus the energy threshold of the detector. What is more, the background light generates a continuous direct current (DC) in the photomultiplier, which may limit their lifetime and may require to operate at lower gain in order to limit the total charge accumulated on the last dynodes and the anode. In addition, a photomultiplier device itself possesses a parasitic effect, called afterpulsing, that requires to set the detector threshold much higher than in case of Poissonian noise (see Sect. 5.4.3).

The night sky background has different components. These are zodiacal light, integrated starlight, air-glow, aurorae, diffuse galactic and extragalactic light [56].

Atmospheric Cherenkov experiments perform their measurements during moonless dark nights when the zodiacal component is very weak or negligible. Also aurorae are rare at mid latitude places. So the main and strong components of NSB influencing Cherenkov detectors are the integrated starlight and air-glow [57].

In addition, anthropogenous light ("light pollution") has to be mentioned here as an important noise source. Artificial light contributes significantly in total surrounding brightness. However, as a rule the array location and experiment conditions are chosen to minimize this effect and it will not be considered here.

NSB brightness is typically on the order of 10^{12} photons $\mathrm{m}^{-2}\,\mathrm{s}^{-1}\,\mathrm{sr}^{-1}$ over the PMT sensitive wavelength range 300–700 nm depending on observing region of the sky and the field of view of the detector [57–59]. Near bright regions of the sky the intensity may increase by a factor up to 4 and more (Fig. 3.5).

Detectors with different angles of view will collect different amount of the NSB. This is due to how many bright stars are in the field of view of the detector. According to [57], for a HiSCORE-like **wide angle** detector ($\Omega \gg 1^\circ$) pointed to a dark region in the sky the intensity is expected to be

$$\Phi_{\mathrm{NSB}}^{0^\circ} = 3.2 \cdot 10^{12}\ \mathrm{ph/m^2\ sr\ s}. \tag{3.8}$$

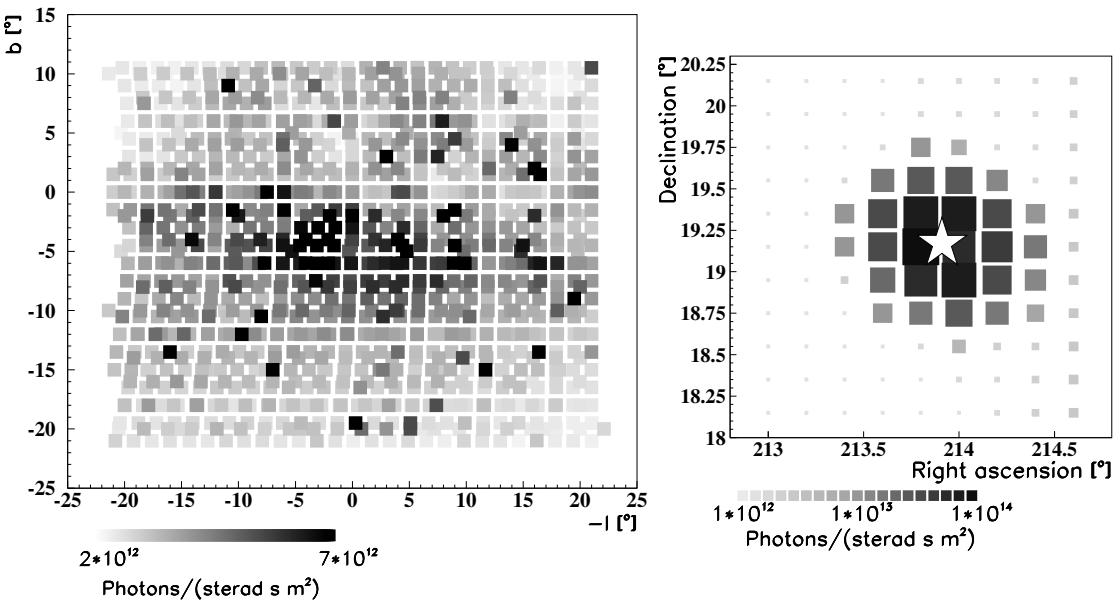

FIGURE 3.5: Photon flux from the central region of the Galaxy, as a function of galactic longitude l and latitude b (*left*). Isolated points with very high flux indicate bright stars. Measured photon flux in the proximity of the star Arcturus (*right*). Source: [58].

In contrast, for a **narrow angle** detector the night sky intensity is lower and it reduces to $\Phi_{\mathrm{NSB}} = (2.2 - 2.5) \cdot 10^{12}\,\mathrm{ph/m^2\ sr\ s}$ [58].

As measured in [57], the count rate drops down by 20% when the detector is inclined at a zenith angle of 30°. With a further increase of the zenith angle to 45° the count rate drops by a further 5%. Hence, for a wide-angle detector inclined by 30° the night-sky intensity is expected to be

$$\Phi_{\mathrm{NSB}}^{30^\circ} = 2.7 \cdot 10^{12}\,\mathrm{ph/m^2\ sr\ s}. \tag{3.9}$$

3.4 Light registration technique

As it was mentioned above, the Cherenkov light registering by an optical detector is contaminated by the night sky light (Fig. 3.6), which is the main limiting factor for lowering the detector energy threshold.

A Cherenkov pulse can be registered if it exceeds the average noise level by a few standard deviations:

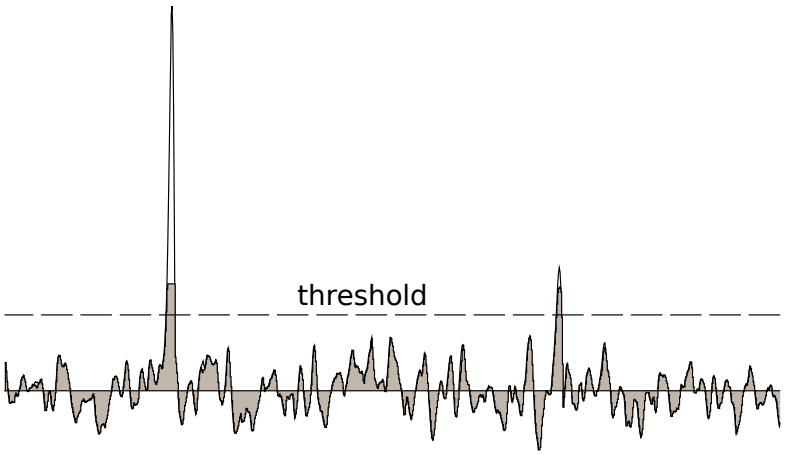

FIGURE 3.6: Cherenkov pulse superimposed on the night sky background. Adopted from [10].

$$\frac{Signal}{Noise} = N_\sigma = \frac{\Phi_{\rm Ch} \cdot QE_{\rm Ch}}{\sqrt{\Phi_{\rm NSB} \cdot \Omega \cdot QE_{\rm NSB} \cdot \tau}}. \tag{3.10}$$

where Φ is the light density, QE is the average quantum efficiency and τ is the system integration time.

For a HiSCORE-like detector ($\Omega \sim 1\,{\rm sr}$) which has $QE_{\rm Ch} = 0.2$ and $QE_{\rm NSB} = 0.1$, $\Phi_{\rm NSB} = 3200\,{\rm ph/m^2}$ sr ns and $\tau = 10\,{\rm ns}$, the minimal required Cherenkov flux results in

$$\Phi_{\rm Ch} = \frac{N_\sigma \sqrt{\Phi_{\rm NSB} \cdot \Omega \cdot QE_{\rm NSB} \cdot \tau}}{QE_{\rm Ch}} = \frac{5\sqrt{3200 \cdot 1 \cdot 0.1 \cdot 10}}{0.2} = 1400\,{\rm ph/m^2}. \tag{3.11}$$

The flux from a 1 TeV gamma ray at a distance of 100 m is roughly $\sim$100 ph/m^2 (see Sect. 7.4.4) that gives an energy threshold of

$$E_{th} = \frac{1400\ {\rm ph/cm^2}}{100\ {\rm ph/cm^2\ TeV}} = 14\,{\rm TeV}. \tag{3.12}$$

Under the same conditions, for an imaging telescope with a narrow angle of $\Omega \sim 0.001\,{\rm sr}$ with a lower integrated intensity of $\Phi_{\rm NSB} = 2200\,{\rm ph/m^2\,sr\,ns}$, the minimal required Cherenkov flux becomes $37\,{\rm ph/m^2}$, that corresponds to an energy threshold of 370 GeV.

The estimates obtained in both cases are very close to the performance of the real Cherenkov detectors. Energy threshold of the existing imaging telescopes have

been summarized early in Sect. 2.2.2. Parameters of the HiSCORE detector will be given in Chap. 6.

Chapter 4

The Tunka-133 experiment

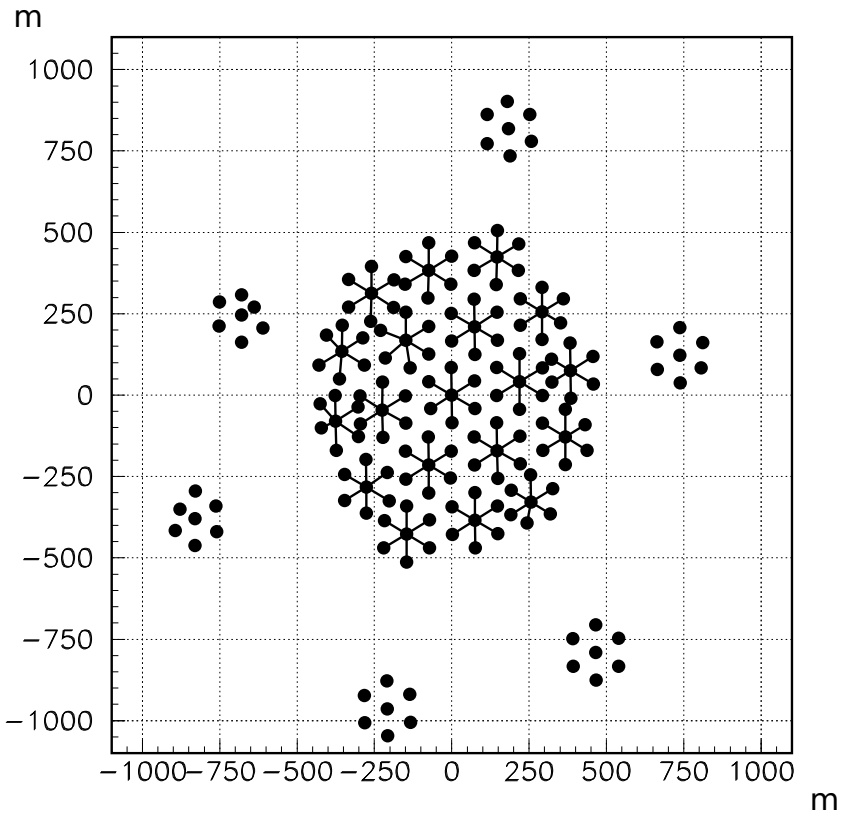

Tunka-133 is an extensive air shower Cherenkov array, which takes data since autumn 2009 [60]. The array was deployed in the Tunka Valley, Russia (51° 48” 35″ N, 103° 04′ 02″ E; 675 m a.s.l.). Tunka-133 operates during clean moonless nights from October to April with a duty circle of 400 h per season. Currently the extended array consists of 175 optical detectors. Each detector is built on the basis of 8″-PMT EMI 9350. The detectors are grouped into 19 clusters with 6 additional outer clusters. Each cluster is composed of seven detectors: six hexagonally arranged detectors with one in the center. The distance between the detectors is chosen to be 85 m, similar to the predecessor array Tunka-25 [61]. The radii of the inner and the outer parts are 0.5 km and 1 km respectively. The optical stations and the electronics of the data acquisition have been designed to operate under the severe conditions of Siberia.

4.1 Data acquisition

4.1.1 Optical detector

Each photomultiplier is placed into a cylindrical metal container with a diameter of 50 cm (Fig. 4.1). The container window is pointed to the zenith and covered with an acrylic glass plate heated from the inside against hoarfrost and dew. The detector is equipped with a remote controlled lid protecting the PMT from sunlight and precipitation. The distance between the container window and the top of the PMT is ranged from 12 to 15 cm. Angular acceptance of the detector reduces smoothly to about 80% at a zenith angle of 40° and to 50% at 50° [60].

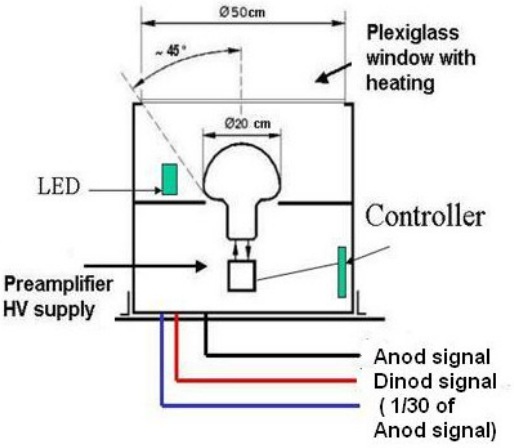

FIGURE 4.1: Optical detector.

Two analog signals, one from the anode and one from the dynode, are read out to provide the required dynamic range of 10^4. The amplitude anode/dynode ratio of these signals is about 30.

4.1.2 Cluster DAQ

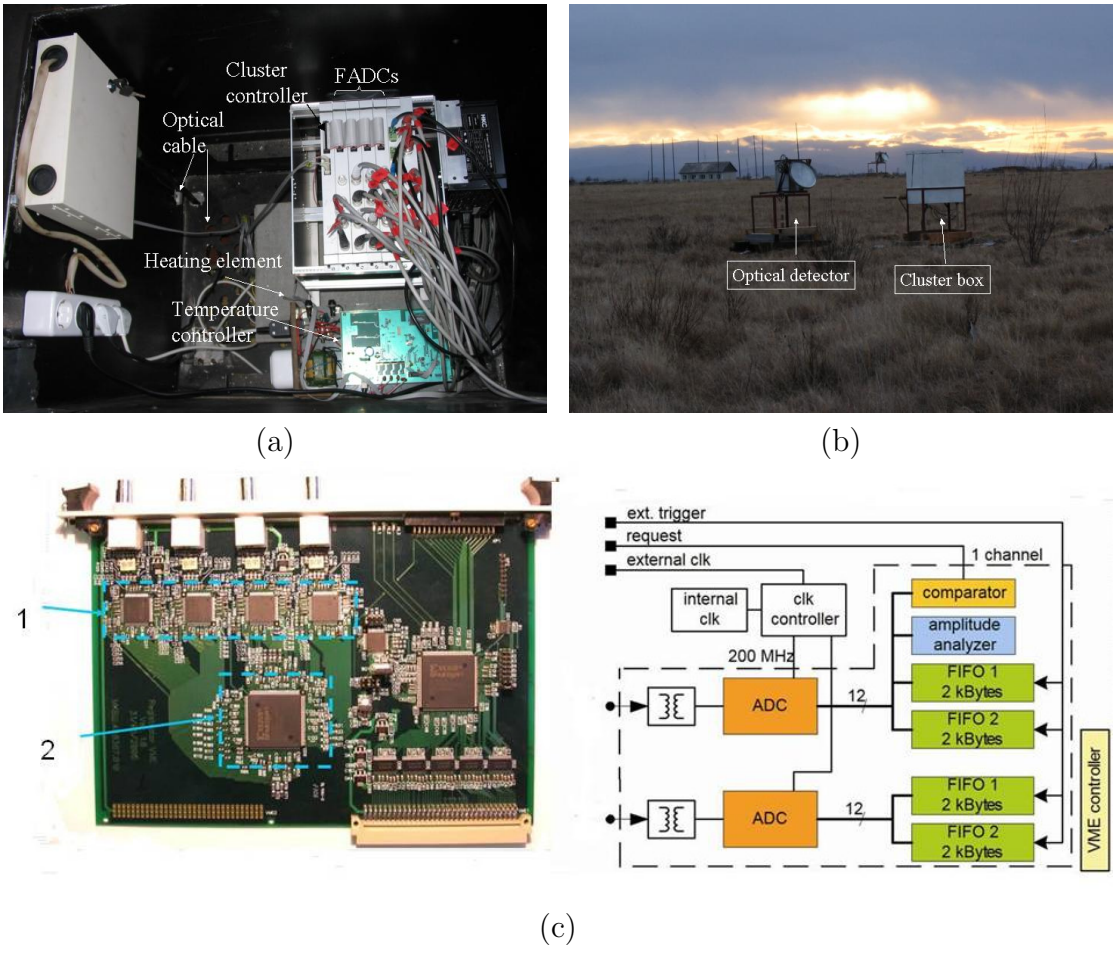

FIGURE 4.2: Cluster DAQ (a). Cluster center (b). FADC board and its internal structure (c): 1 — AD9430 (12 bit, 200 MHz), 2 — FPGA Xilinx Spartan-3.

The PMT signals from the optical detector are transmitted via 100 m coaxial cable RG-58 to the cluster box placed in the center of the cluster (Fig. 4.2). They are digitized by custom-made 12 bit 4-channel-FADC modules with 200 MHz sampling rate and connected to comparators with an adjustable threshold [62]. The sampling FADC board is based on AD9430 fast ADC and FPGA XILINX Spartan XC3S300 microchip [63]. The local cluster trigger is formed by the coincidence of at least three pulses from detectors exceeding the threshold within a time window

of 0.5 μs. The cluster box is equipped with a heater and remote radio control to keep the temperature inside the box at a required level of 18°C.

4.1.3 Time synchronization

Optical detectors of a cluster are connected with the cluster box via cables RG-58 of equal length. Deviations from the equality can be corrected at the subsequent stages during the reconstruction using the shower front. Clusters in turn are connected with the central DAQ via optical fibers having different lengths. Since every cluster has a local timer, the time offsets between the clusters have to be found.

The time synchronization between clusters is performed in two steps (Fig.4.3). First, the cable delay and other propagation delays are measured. Central DAQ sends to the cluster a synchronous package which returns back from the cluster after decoding. The resultant delay divided by two corresponds to the propagation delay. Second, the central DAQ sends a timer reset command simultaneously to all cluster DAQs. This scheme allows to calculate differences between timers for each cluster. The accuracy of this time synchronization between clusters is about 10 ns. The procedure is repeated every second to avoid mistiming.

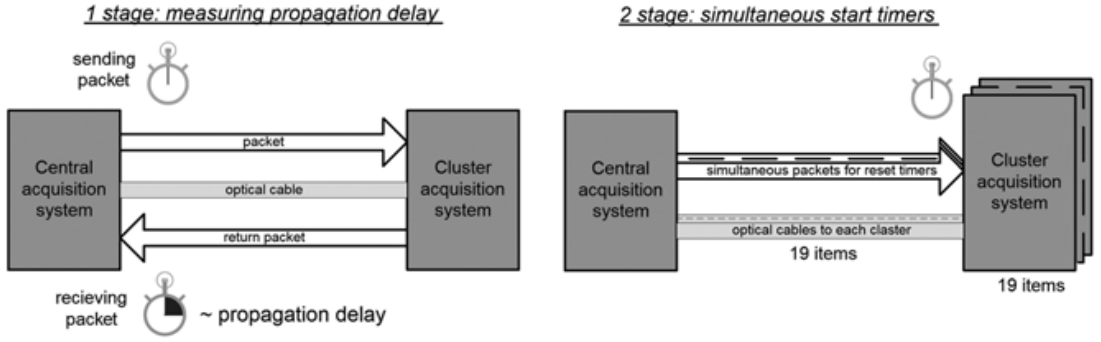

FIGURE 4.3: Concept of the time synchronization system [63].

4.2 Data processing

4.2.1 Preprocessing

A pretreatment program block processes the raw data taken separately by each cluster and merges the data into shower events. Data preprocessing is carried out in three main steps [9].

(1) Analysis of pulse traces:

- ▷ analysis of the 5 μs pulse trace digitized with a step of 5 ns;
- ▷ pulse finding as a significant excess of the amplitude in 5 and more sequential points;
- ▷ determination of the zero-line level as an average value on an interval of 1.5 μs from the beginning of the trace;
- ▷ correction of measured amplitudes by subtracting the zero-line due to the transformer connection at the input and output of the transmitting cable RG-58.

(2) Pulse fitting:

- ▷ fitting the pulse (Fig. 4.4) by the four parametric function [64];
- ▷ determination of three basic pulse parameters using this function: front delay on a level of 0.25 of the pulse maximum (t_i), pulse integral (Q_i), and pulse width at a level of 0.5 of the pulse maximum ($\tau_{1/2}$). The function is given by

$$f(t) = \begin{cases} A\exp\left(-k^{2+0.5k}\right), & x \leq 0, \\ A\exp\left(-g^{h}\right), & x > 0, \end{cases} \tag{4.1}$$

where

$$x = t - t_{max},$$
$$k = \mid x/t_{rise} \mid,$$

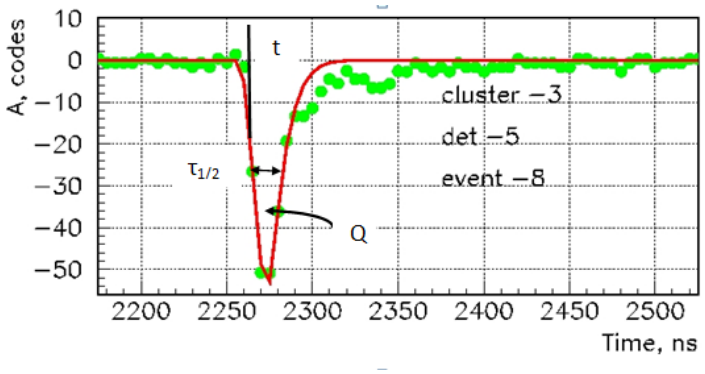

FIGURE 4.4: Pulse fit.

$$g = x/t_{fall},$$

$$h = \begin{cases} 1.7 - 0.5g, & g < 0.8, \\ 1.3, & g \geq 0. \end{cases} \tag{4.2}$$

(3) Data merging. Different clusters are merged into one event within 2 μs coincidence time.

Finally, the data of each event are summarized into ascii *prm*-files (see Appendix D), which include parameters of pulses and trigger times of clusters.

4.2.2 Calibration

Time calibration. The time calibration begins with the correction of internal detector delays t_i inside each cluster relative to the central detector. This is required because the length of coaxial cables is known with a precision of 2 m ($\sim$ 10 ns). Moreover pulse delays may vary likewise when changing the high voltage of the PMT. In that case, these detector delays can be determined offline using the shower data [9]. This method is applied only to a cluster with maximal pulse amplitudes. Measured time delays t_i of each cluster are fitted by a parametrization of the plane shower front and the hardware delays are corrected until the average shower front residuals become less 1 ns. Finally, these correction coefficients are kept. However, the reconstructed shower direction by a single cluster can be incorrect. This systematic error is eliminated by the second calibration.

This method calibrates clusters between each other. For this, events with more then 9 triggered clusters (shower radius $R \sim 500$ m) are used. In the same way,

measured delays t_i are fitted by a curved shower front (Fig. 4.5) and the hardware delays are tuned. The resultant synchronization accuracies between clusters become less than 10 ns, leading to an inaccuracy in arrival direction of less then $\arcsin(3/500) = 0.3°$.

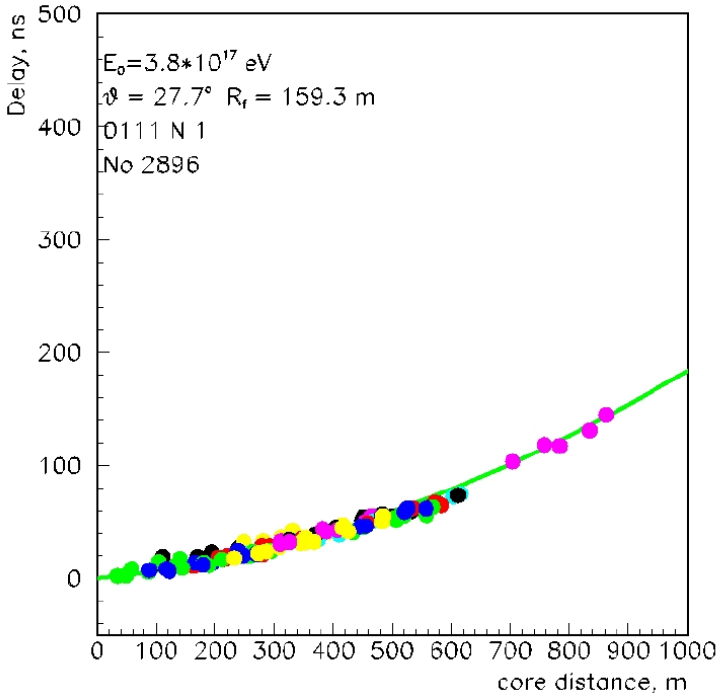

FIGURE 4.5: Fit to the data with the curved shower front. The colors mark different clusters.

Amplitude calibration. The abundance of registered events permits to calibrate detectors between each other [65].

Integral spectra of Cherenkov light densities reflect in some sense the slope of the integral spectra of cosmic rays. Before the knee the slope is 1.7. However, the measured slope of light densities may differ due to the nature of the Cherenkov light production in the atmosphere and the trigger logic of the actual data acquisition system. As a result, the resulting slope becomes less than 1.7.

The idea of the amplitude calibration is that the flux of cosmic rays is constant. If it is so, then any actual flux displacements registered by a photodetector are due to differences in parameters of the detector, such as sensitivity, area or aperture. But when all detectors are similar, the same area and aperture, the differences are caused by the detector sensitivity only, or rather by the gain of the PMT.

Amplitude integral spectra are analysed and correction coefficients, which make spectra similar for large amplitudes, are determined. As a rule, the slope of the spectrum is chosen to be the same for all detectors, and the calibration is done with respect to a reference detector. Finally, correction coefficients are stored into a calibration file.

Weather selection. Weather conditions have an impact on detector rates. Sudden changes in detector rates indicate the changes of the atmosphere transparency caused by cloudiness or fog (Fig. 4.6). An analysis of detector rates allows to select good weather periods. Typically stable periods ($\Delta R/R < 20\%$) longer then 1 h are chosen. The number of such periods is typically up to 5. Roughly 50% of the data can be used for the further analysis.

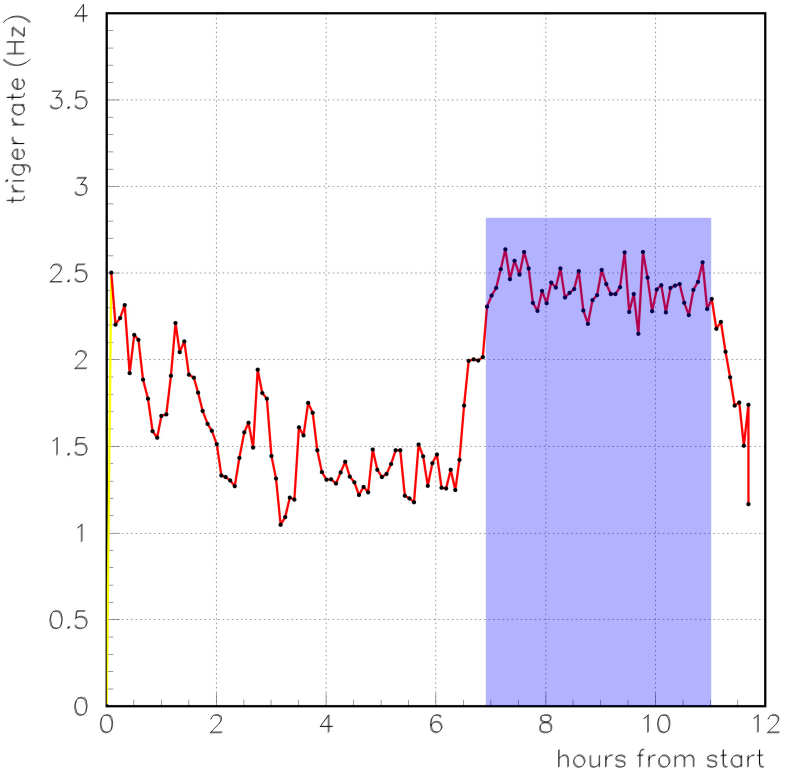

FIGURE 4.6: Rate variation of a single station during the observation period. The good period from 7 to 11 h will be selected for analysis.

4.3 Shower reconstruction

Here will be given a summary of the reconstruction techniques used in the Tunka-133 experiment. An example of the reconstructed event is shown in Fig. 4.7.

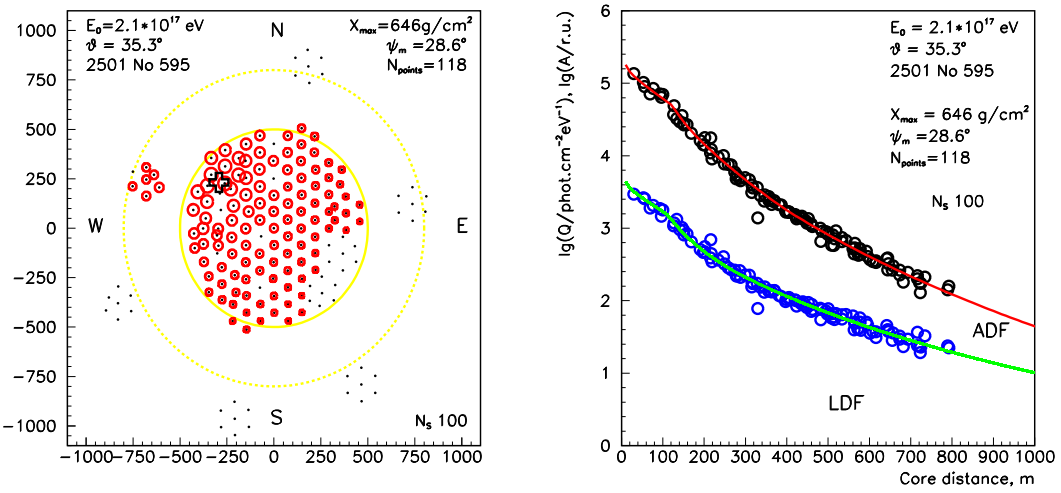

FIGURE 4.7: *Left*: Tunka-133 event display. *Right*: Resulting fit using lateral functions ADF and LDF. ADF is shown in relative scale.

4.3.1 Centre of gravity

The centre of gravity (COG) of the measured signals S_i is used as preliminary estimator of the core position:

$$\mathbf{x}_{\mathrm{COG}} = \frac{\sum_i S_i \mathbf{x_i}}{\sum_i S_i}, \tag{4.3}$$

where S_i is the pulse integral Q_i or the pulse amplitude A_i. This method is employed to estimate initial guess parameters for further approximations by lateral functions and by the curved front. In some cases $\log_{10} S_i$ instead of S_i should be used to take into account the rapid decrease of signals at large distances.

4.3.2 Arrival direction

The expected signal time of a detector at the position $\mathbf{x}$ is parametrized as

$$t(\mathbf{x}) = t_0 + \underbrace{(\mathbf{x} - \mathbf{x_c})\mathbf{n}/c_{air}}_{\text{plane wavefront}} + \underbrace{\widetilde{t}(R)}_{\text{curved wavefront}} \quad . \tag{4.4}$$

Here, t_0 is the time when the shower core reaches the ground, $\mathbf{x_c}$ is the position of the shower core on the ground and $\mathbf{n}$ is the unit vector in the direction of the shower axis. The term $\widetilde{t}(R)$ describes the shape of the curved shower front as a

function of distance R to the shower axis. Monte Carlo studies with CORSIKA show that the shower front is described well up to 1 km distance by a parabolic front with a single curvature parameter R_s [66]:

$$\widetilde{t}(R) = \left(\frac{200+R}{R_s}\right)^2 \frac{1}{c_{air}}. \tag{4.5}$$

The standard functional for minimization is given by

$$\chi^2 = \sum_i (t_i - t(\mathbf{x_i}))^2. \tag{4.6}$$

Here, some pre-defined core position is required for both plane and curved terms. However, it can be slightly modified excluding the core position from the plane wavefront term. Finally, the core position is replaced with coordinates of a reference detector:

$$\chi^2 = \sum_i (t_i - \Delta t_{in}(\mathbf{x_i}, \mathbf{x_n}) - \widetilde{\Delta t}_{in}(\mathbf{x_i}, \mathbf{x_n}, \mathbf{x_c}) - t_n)^2, \tag{4.7}$$

where

$$\begin{aligned}
&\Delta t_{in}(\mathbf{x_i}, \mathbf{x_n}) = (((x_i - x_n)\cos\phi + (y_i - y_n)\sin\phi)\sin\theta + (z_i - z_n)\cos\theta)/c_{air},\\
&\widetilde{\Delta t}_{in}(\mathbf{x_i}, \mathbf{x_n}, \mathbf{x_c}) = \widetilde{t}(R_i) - \widetilde{t}(R_n),\\
&R_i = \sqrt{(x_{\perp i} - x_{\perp c})^2 + (y_{\perp i} - y_{\perp c})^2}.
\end{aligned}$$

The coordinates (x_n, y_n) define the reference detector. Recalculation to the shower plane is given by

$$\begin{aligned}
x_\perp &= (x\cos\phi + y\sin\phi)\cos\theta + z\sin\theta,\\
y_\perp &= -x\sin\phi + y\cos\phi.
\end{aligned} \tag{4.8}$$

As can be seen, it is not necessary to use the shower core position to perform the planewave fit, however, it cannot be excluded from the curved wavefront.

4.3.3 Lateral distribution function

Previously, in Tunka-25, the whole reconstruction was based on the fit of Cherenkov densities Q_i with a specially designed lateral distribution function (LDF) [67]. This method was used to reconstruct most shower parameters, such as shower core, energy, and depth of the shower maximum. Today, for Tunka-133, the LDF fit was slightly changed and it is mostly used to derive the parameter Q_{200} to reconstruct the shower energy. The reconstruction of other shower parameters was implemented on the basis of a new amplitude distance function (ADF), that, on the contrary, fits pulse amplitudes.

The LDF is parametrised as

$$Q(R) = Q(200) \cdot \left(\frac{200}{R_{kn}}\right)^{a_Q} \cdot f_Q(R). \tag{4.9}$$

The function $f_Q(R)$:

$$f_Q(R) = \begin{cases} \exp\left(\frac{R_{kn}-R}{R_0}\left(1+\frac{3}{R+3}\right)\right), & R < R_{kn}, \\ \left(\frac{R}{R_{kn}}\right)^{-a_Q}, & R_{kn} \le R < 300 \text{ m}, \\ \left(\frac{300}{R_{kn}}\right)^{-a_Q}\left((\frac{R}{300}+1)/2\right)^{-b_Q}, & R \ge 300 \text{ m}, \end{cases} \tag{4.10}$$

where three variables are expressed in terms of the steepness b_Q:

$$b_Q^* = \begin{cases} \log_{10}(b_Q - 2.6), & b_Q > 2.9, \\ \log_{10}(2.9), & b_Q \le 2.9, \end{cases}$$

$$R_{kn} = \begin{cases} 100 - 38 \cdot (b_Q - 4.5)^2 \text{ [m]}, & b_Q \le 4.5, \\ 100 \text{ [m]}, & b_Q > 4.5, \end{cases}$$

$$R_0 = 10^{2.3-1.76 \cdot b_Q^*} \ [m],$$

$$a_Q = 1.97 + 0.12 \cdot (b_Q - 3.314)^2.$$

4.3.4 Amplitude distance function

The reconstruction of the shower core position and the depth of the shower maximum is done by fitting the measured amplitudes A_i using the amplitude distance function (ADF):

$$A(R) = A(200) \cdot f_A(R). \tag{4.11}$$

The function $f_A(R)$:

$$f_A(R) = \begin{cases} \left(\frac{200}{R_{kn}}\right)^{a_A} \exp\left(\frac{R_{kn}-R}{R_0}\left(1+\frac{3}{R+2}\right)\right), & R < R_{kn}, \\ \left(\frac{R}{200}\right)^{-a_A}, & R_{kn} \le R < 200, \\ \left(\frac{c_A+0.5}{c_A+1}\right)^{b_A} \left(\left(\frac{R}{400}+c_A\right)/(1+c_A)\right)^{-b_A}, & 200 \le R < 400, \\ \left(\frac{c_A+0.5}{c_A+1}\right)^{b_A} \left((\frac{R}{400}+1)/2\right)^{-b_A}, & R \ge 400. \end{cases} \tag{4.12}$$

The four variables are parametrized via the similar to LDF steepness parameter b_A:

$$b_A^* = \begin{cases} \log_{10}(b_A - 5), & b_A > 5.4, \\ \log_{10}(0.4), & b_A \le 5.4, \end{cases}$$

$$R_{kn} = 145 - 115 \cdot b_A^* \ [m],$$

$$R_0 = 10^{2.44-2\cdot b_A^*} \ [m],$$

$$a_A = \begin{cases} 2.4 + 2 \cdot (b_A^* - 0.15), & b_A^* \ge 0.15, \\ 2.4, & b_A^* < 0.15, \end{cases}$$

$$c_A = 0.89 - 0.29 \cdot b_A^*.$$

4.4 Energy spectrum of cosmic rays

4.4.1 Energy reconstruction

The Cherenkov light flux density at a core distance of 200 m is used as the energy estimator:

$$E_0 = const \cdot Q_{200}^{g}. \tag{4.13}$$

CORSIKA simulations reveal that the index g is 0.94 over the energy range $10^{16} - 10^{17}$ eV. The index value was obtained for the zenith angle from 0° to 45°, and a complex composition, consisting of equal fractions of protons and iron nuclei. The absolute energy calibration is performed using a reference energy spectrum from the joint experiment QUEST [68].

4.4.2 Energy spectrum

The energy spectrum of cosmic rays was reconstructed using the data of 3 seasons (2009–2012) and is illustrated in Fig. 4.8 [66]. The data with a total observational time of 980 hrs and a total number of registered events of $\sim 6 \cdot 10^6$ were used. Showers were selected inside a circle with a radius of $R = 450$ m from the center of the array and with the zenith angle below 45°. The array under these cuts reaches the full efficiency at an energy of $6 \cdot 10^{15}$ eV. Above this energy, about 170,000 events were selected: 60,000 with $E > 10^{16}$ eV and 600 with $E > 10^{17}$ eV.

The energy spectrum can be extended to higher energies by additionally taking into account events inside an larger area with a radius of 800 m. This allows to increase statistical validity for energies up to 10^{18} eV. Both spectra are well connected at an energy of 10^{17} eV. Finally, the combined spectrum containing about 1900 events with $E > 10^{17}$ eV was obtained.

The knee in the region from 3 to 6 PeV seems to have a compound structure and may indicate the acceleration limit of the light component: proton (2.8 PeV, Z=1) and helium (5.6 PeV, Z=2). The energy spectrum above the knee looks also complicated and can be fitted by a power law with 3 different indices:

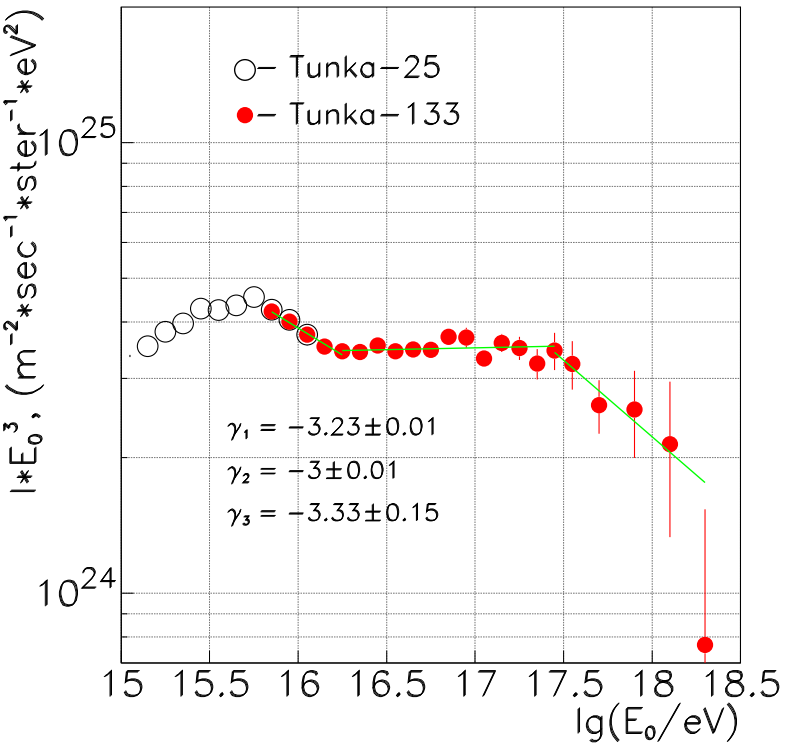

FIGURE 4.8: Combined primary cosmic ray spectrum measured with Tunka-133 array. Three years of data were used.

$$\gamma = \begin{cases} 3.23 \pm 0.01, & 6 \cdot 10^{15} < E \leq 2 \cdot 10^{16} \text{ eV}, \\ 3.00 \pm 0.01, & 2 \cdot 10^{16} < E \leq 3 \cdot 10^{17} \text{ eV}, \\ 3.33 \pm 0.15, & 3 \cdot 10^{17} < E \leq 10^{18} \text{ eV}. \end{cases}$$

It should be noted, that the spectrum is in good agreement with the results of the present experiments (see Sect. 5.7).

4.5 Mass composition of cosmic rays

The mass composition studies in the knee energy range are important for understanding acceleration and propagation mechanisms of cosmic rays in the Galaxy and Metagalaxy. In the PeV energy range the composition beyond the knee monotonically changes. As established by KASCADE [25] and KASCADE-Grande [26], the composition becomes heavier up to 10^{17} eV and the spectrum of heavy elements has a knee-like structure. In the range $10^{17} - 2 \cdot 10^{18}$ eV, the mass composition

turns again to be lighter according to the Auger data [69]. These may hint the transition from the galactic to the extragalactic acceleration regime.

Substantially there are two observables available, which are sensitive to the mass of the primary nucleus: the depth of the shower maximum X_{max} and the ratio between the number of electrons and muons at the ground level N_e/N_μ.

While fluorescence detectors, such as Auger [69] and TA [70], provide reliable measurements of X_{max} above 10^{17} eV, only the Cherenkov technique accesses the depth of the shower maximum below this energy with a good accuracy of 25–30 g/cm^2. Cherenkov light registration with a modern non-imaging array has potentially a much better energy resolution of 10-15% than EAS arrays detecting charged particles only. Moreover, interpretation of the data obtained with the charged particle counters is based on the used hadron interaction model and may vary from model to model. Cherenkov light from an air-shower in the atmosphere is mainly produced as a result of electromagnetic cascades that is less dependent on the chosen interaction model. Thus, the Cherenkov technique gives a unique possibility for studies of the mass composition of cosmic rays.

Different parameters such as mean and RMS of the experimental X_{max} distributions are typically used to draw conclusions about the mass composition. Their behaviour with energy can be interpreted in terms of the logarithm of the mass number A [71]:

$$\langle \ln A \rangle = \frac{\langle X^p_{max} \rangle - \langle X^{data}_{max} \rangle}{\langle X^p_{max} \rangle - \langle X^{Fe}_{max} \rangle} \ln A_{Fe}. \tag{4.14}$$

Besides that, the X_{max} data can be characterized by a fit using primary distributions for different mass groups (typically up to 5).

4.5.1 Shower maximum reconstruction

The depth of the shower maximum X_{max} in the standard Tunka-133 approach can be reconstructed in two different ways [66]. The first method is based on the shape of the amplitude distance function b_A (b-method). The second method employs the width of pulse at 400 m τ_{400} (τ-method). Since the τ-method has a higher energy threshold the b-method is mainly used.

Following the Monte Carlo simulations, these two parameters, b_A and τ_{400}, are strictly correlated with the *distance to the shower maximum* $\Delta X_{max} = X_0/\cos\theta - X_{max}$:

$$\Delta X_{max} = A_1 - B_1 \cdot \log_{10}(b_A - 2),$$
$$\Delta X_{max} = A_2 - B_2 \cdot \log_{10}\tau_{400}.$$

MC predicts that the parametrization does not depend on energy, zenith angle of showers, mass composition and the used interaction model.

The model parameters are derived with the so-called *phenomenological approach* [66]. By knowing how parameters b_A and τ_{400} vary with the zenith angle (more general with $\sec\theta$), coefficients (A_1, A_2, B_1, B_2) can be determined. For that, a narrow energy bin with the known mean depth of the shower maximum is used. This approach provides more robust method to reconstruct the shower maximum then pure Monte Carlo. Currently, the X_{max} was calibrated using the data of the fluorescence experiments Auger [69] and HiRES/MIA [72]. For the energy bin $16.4 < \log_{10}(E_0/\mathrm{eV}) < 16.5$ and $< X_{max} >= 580\,\mathrm{g/cm^2}$ the constants are the following:

$$A_1 = 2865\ \mathrm{g/cm^2}, B_1 = 3519\ \mathrm{g/cm^2};$$
$$A_2 = 3344\ \mathrm{g/cm^2}, B_2 = 1624\ \mathrm{g/cm^2}.$$

The comparison of both methods gives an X_{max} resolution ranging from $37\,\mathrm{g/cm^2}$ at $10^{15.85}\,\mathrm{eV}$ to $28\,\mathrm{g/cm^2}$ at $10^{16.35}\,\mathrm{eV}$ or higher [66]. This value is close to the width of natural shower fluctuations of iron induced showers in the atmosphere. This makes the steepness b_A and the pulse width τ_{400} sensitive parameters for chemical composition studies.

4.5.2 Elemental composition

Experimental X_{max} distributions at different energies can be fit using several elemental groups from proton to iron [73]. The fraction of each group will characterize its contribution to the primary composition.

For this analysis, experimental distributions of the shower depths within narrow logarithmic intervals were selected and analysed. The energy range was divided into two data samples with the following binning: $E = 7 \cdot 10^{15} - 10^{17}$ eV with a bin width of 0.1 on a logarithmic scale, $E = 10^{17} - 10^{18}$ eV with three merged bins.

Similar to the reconstruction of the energy spectrum (see Sect. 4.4.2), the same data set of 3 seasons (2009-2012) was used. Events were selected with core positions inside a circle radius of 450 m and with the zenith angle below 45°. The total number of selected events is 99510: 53399 ($> 10^{16}$ eV) and 617 ($> 10^{17}$ eV).

Primary distributions were simulated for four types of nucleus, such as proton, helium, nitrogen and iron, with CORSIKA 7.35 (QGSJETII-04/GHEISHA) within the energy range from $10^{15.5}$ to $10^{17.5}$ eV (see Sect. 7.4.5). Each distribution was parametrised by the Gamma function and can be interpolated to any primary energy within the PeV energy range. Primary distributions were additionally convoluted before the fit with the resolution of the shower maximum, which is modelled by a Gaussian with σ given in Sect. 4.5.1 The instrument response is taken equal for all nuclei groups.

The weight of each group was found by the log-likelihood minimization and used to obtain the elemental spectra and the mean logarithm of mass A. As initial guesses, each weight was ranged with a step of 0.1 from 0 to 1. The resultant mean and the standard deviation were calculated. Furthermore, each bin of the experimental distributions was varied according to Poisson law and the procedure is repeated 10 times to estimate systematic uncertainties.

The results of the fit for different groups are shown in Fig. 4.9. More informative can also be the fraction of the light (H+He) and heavy components (N+Fe), which are shown in Fig. 4.10 in comparison with results from KASCADE-Grande [26].

As seen, the features of the primary spectrum might be explained from the standpoint of the mass composition of cosmic rays. This investigation reveals that the complex knee at $(3 - 6) \cdot 10^{15}$ eV in the spectrum could be associated with a limit

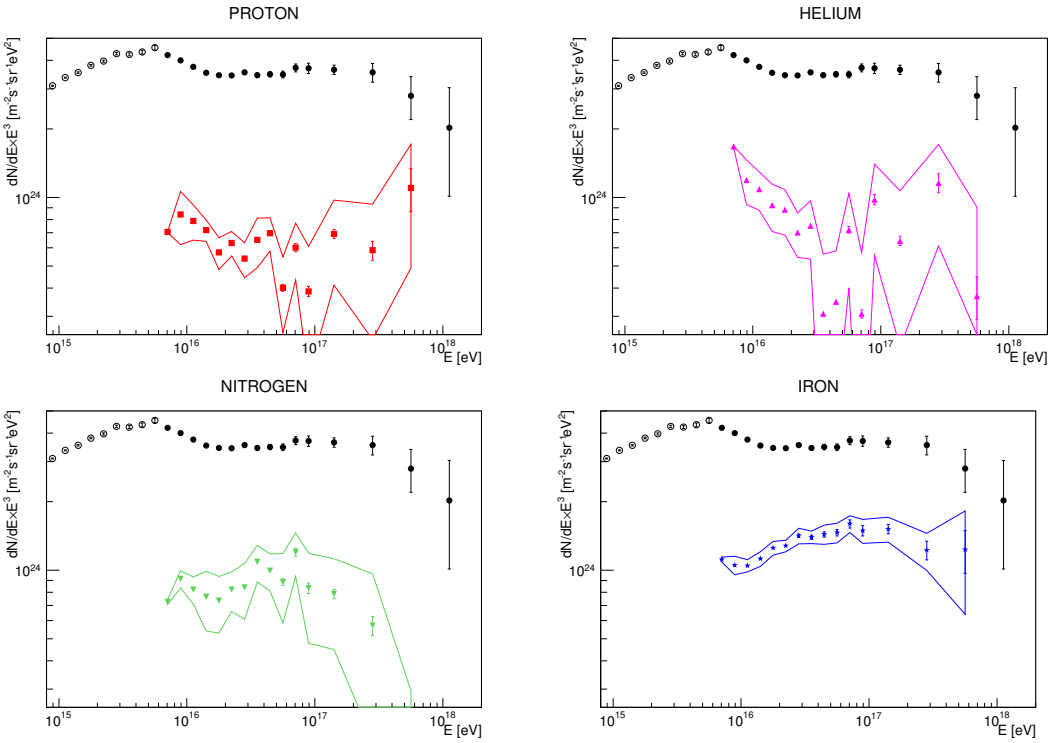

FIGURE 4.9: Elemental spectra of different nuclei: proton, helium, nitrogen and iron. The merged Tunka-25(○)/Tunka-133(●) all-particle spectrum is shown. Error bars and shaded bands represent statistical and systematic uncertainties.

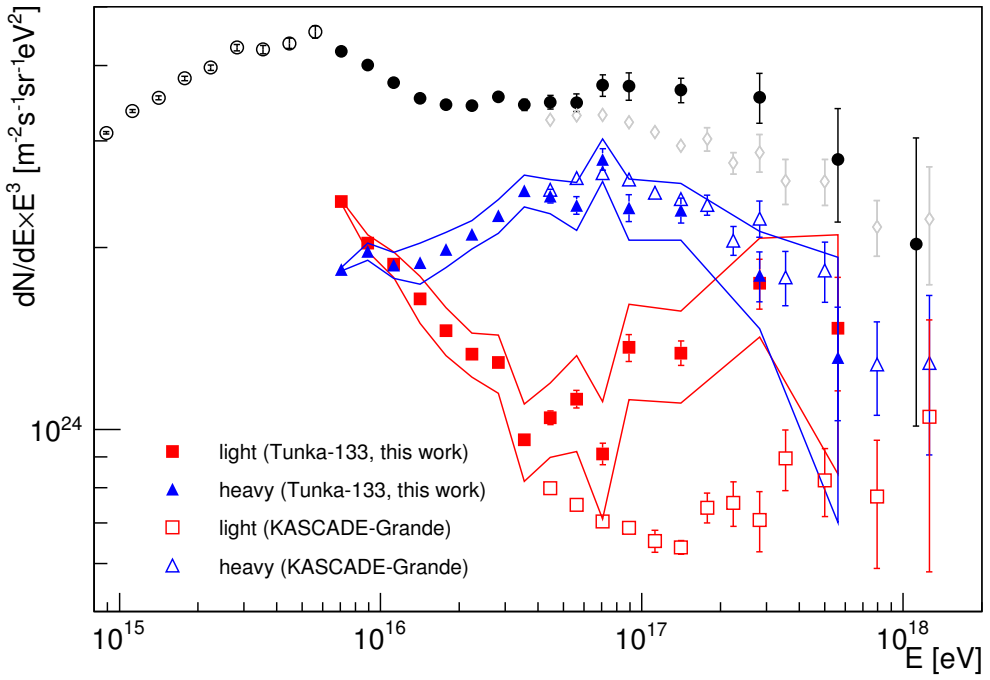

FIGURE 4.10: Spectrum of the *light* and *heavy* fractions in comparison with the KASCADE-Grande results [26].

of acceleration of the light component in the Galaxy. Moreover, above $3 \cdot 10^{16}$ eV a similar growth of the light component can be seen also caused by probably the potential extragalactic modulation [74]. Similar to KASCADE-Grande, the same knee-like structure in the spectrum of the heavy component has been obtained at an energy of $7 \cdot 10^{16}$ eV.

This behaviour implies an increase of the mean logarithmic mass as a function of energy (Fig. 4.11) up to 10^{17} eV from 2.0 to 2.7. Above 10^{17} eV the composition becomes lighter again down to 2.1 at an energy of $6 \cdot 10^{17}$ eV. The obtained $\ln A$ has a quite smooth behaviour and in good agreement with the KASCADE data [25] and the data of the fluorescence experiments HiRES/MIA [72] and Auger [69].

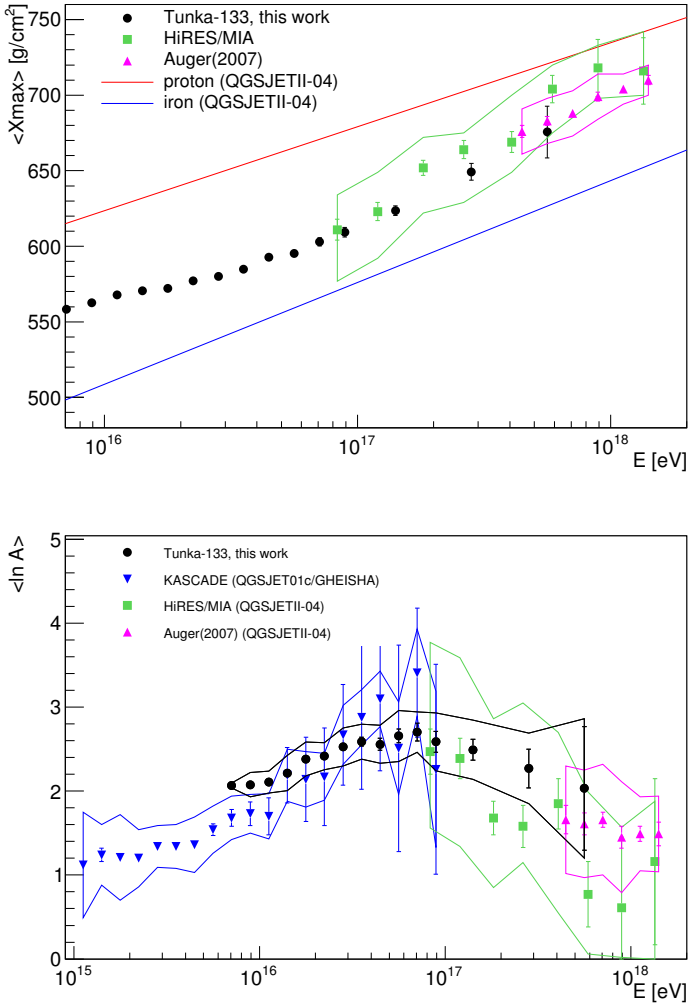

FIGURE 4.11: Mean depth of shower maximum (*left*) and mean logarithm of atomic number (*right*) as a function of energy in comparison with fluorescence experiments HiRES/MIA [72] and Auger [69]. Error bars and bands represent statistical and systematic uncertainties.

Chapter 5

The HiSCORE-9 experiment

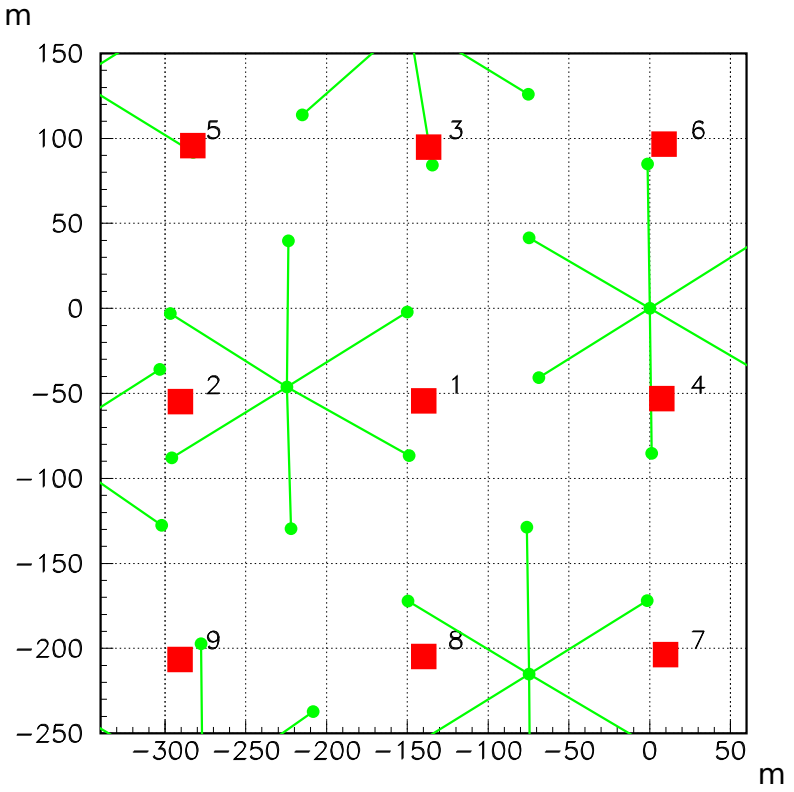

FIGURE 5.1: The HiSCORE-9 detector layout. Red squares – HiSCORE detectors, green circles – Tunka-133 detectors.

HiSCORE (**H**undred***i** **S**quare km **C**osmic **O**rigin) is a new detector concept, based on the air shower Cherenkov detection technique, using a non-imaging wide-angle array up to 100 km^2. HiSCORE is intended for gamma ray astronomy from 10 TeV to several PeV and cosmic ray studies from 100 TeV to 1 EeV. It will search for ultra-high energy gamma ray sources (*pevatrons*) and measure cosmic

ray spectrum and mass composition in the region of the knee with a unprecedented accuracy. The HiSCORE array is started to be deployed at the site of the Tunka-133 experiment near Lake Baikal in Russia. A 9-station engineering array is in operation since October 2013, arranged on a regular grid of 3×3 stations with 150 m distance and an instrumented area of 0.09 km^2 (Fig. 5.1). Analysis of the first data of HiSCORE-9 will be presented in this chapter.

5.1 Optical station

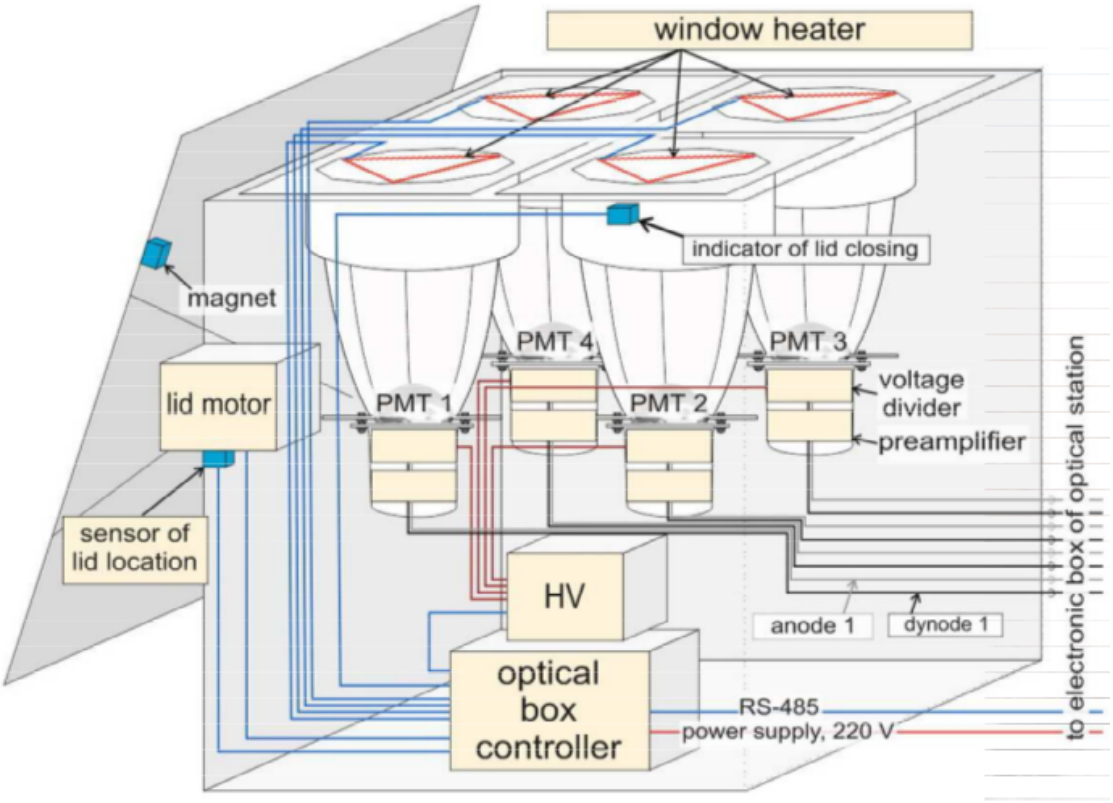

FIGURE 5.2: HiSCORE optical station [75].

The optical station (Fig. 5.2) consists of four photomultipliers with a photocathode of 20 cm in diameter. Each PMT is placed in the focus of a Winston cone with a half-opening angle of 30°, which enlarges the collection area of the station by a factor of 4. Each station is covered with an acrylic glass plate with a thickness of 4 mm. The plate is heated from the inside to protect the PMT and the light concentrator from dust and atmospheric precipitation. Furthermore, the heating prevents from the hoarfrost formation on the plate during cold periods, and an

opening lid is used to protect PMTs from destructive light. The optical station either can be pointed to the zenith or can be tilled to the south/north by 25°.

The station is equipped with a slow-control and high-voltage supply. Signals from the anode and the dynode of each PMT are transferred into an electronic box with coaxial cables RG-58 with a length of ∼5 m, that does not lead to a strong distortion of signals. Anode signals are summed up by an analog summator [76], and the sum proceeds to a discriminator.

5.2 Data acquisition and time synchronization

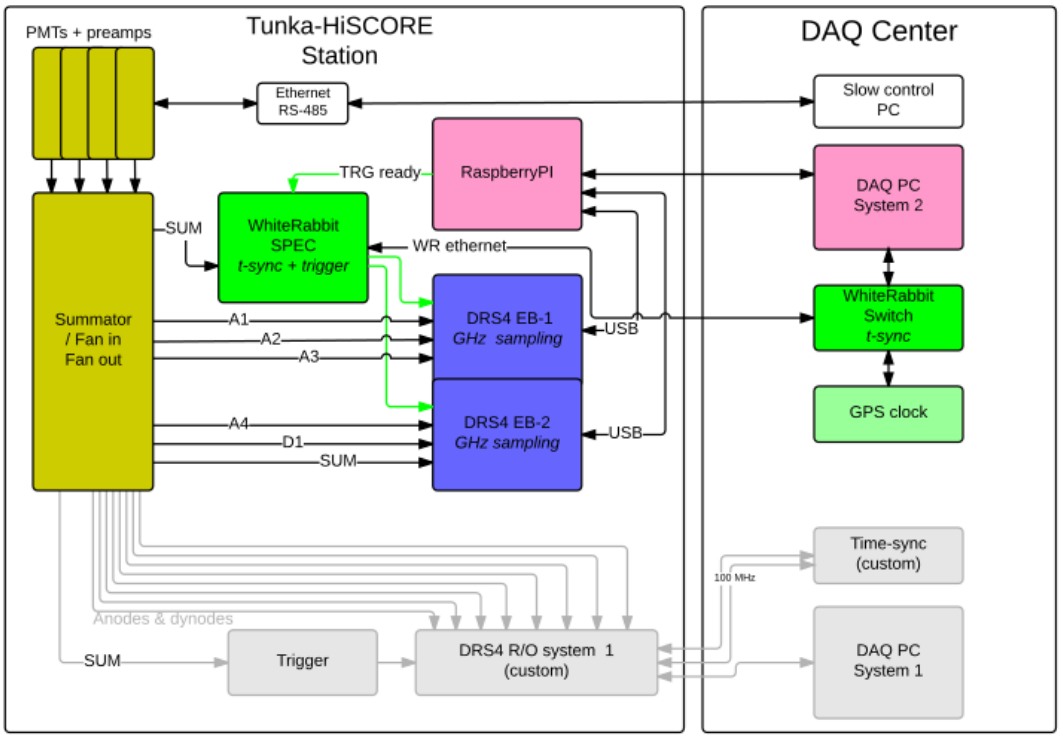

FIGURE 5.3: Schematics of the setup: DAQ-1 (*gray*) and DAQ-2 (*color*) [77].

The HiSCORE-9 array is operated under two independent data acquisition systems (Fig. 5.3). Both systems are based on the DRS4 chip [78]. DRS4 (Domino Ring Sampler) is a 9-input waveform digitizer, sampling signals simultaneously from 0.7 GSPS to 5 GSPS with 1024 sampling points. The array time synchronization is done by a custom system in DAQ-1 and by the ethernet-based White-Rabbit [79] system in DAQ-2. A summary of both systems is given in the following table:

	DAQ-1	DAQ-2
channel configuration	8+1(sync)	(3+1(sync))×2
recorded channels	$A_{1..4}$, $D_{1..4}$, sinc	$A_{1..4}$, D_1, sinc, sinc
DRS4 amplitude range	–0.5..+0.5 V	0..+1 V
maximum count rate	180 Hz	50 Hz
dead time	0.5 ms	20 ms
time granularity (station)	0.5 ns	1 ns
time granularity (sync)	0.2 ns	1 ns
discriminator time	10 ns	9 ns

5.2.1 DAQ-1

Data acquisition. The signal digitizing unit was build with the DRS4 chip. It allows to use nine inputs: 4 anode signals, 4 dynode signals, 1 synchronization signal (sync). Anode and dynode signals are dumped by a factor of 4 and digitized with a step of 500 ps in 1024 points. The sync signal is digitized with a step of 200 ps. The DRS4 operates in bipolar mode from –0.5 V to +0.5 V. The amplitude is digitized with a range of 8096 codes.

Time synchronization. The synchronization unit (Fig. 5.4) is made on the basis of a commercially available evaluation board FPGA Spartan-6 SP605 [80]. The time synchronization operates in the following way [52].

The HOST has a master clock (100 MHz) defining a frequency of the entire system. The HOST also comprises a timer, which generates the sync pulse. The base clock and the sync are input to a modulator, where sync is admixed to the clock. This signal is then transmitted via optical fiber to DAQ.

In the station the signal arrives at the demodulator. Here, the base clock is restored and the sync is detached. The admixed signal is sent back via optical fiber to the HOST.

In the HOST, the received signal arrives also at the demodulator, where in a similar way the base clock is restored, and the sync is detached. A rough calculation of the phase shift is made by a phase difference of the received sync and the transmitted sync with an accuracy of the base frequency 10 ns. Besides that, both the base and the restored clocks are transmitted to the phase detector based on the DRS4

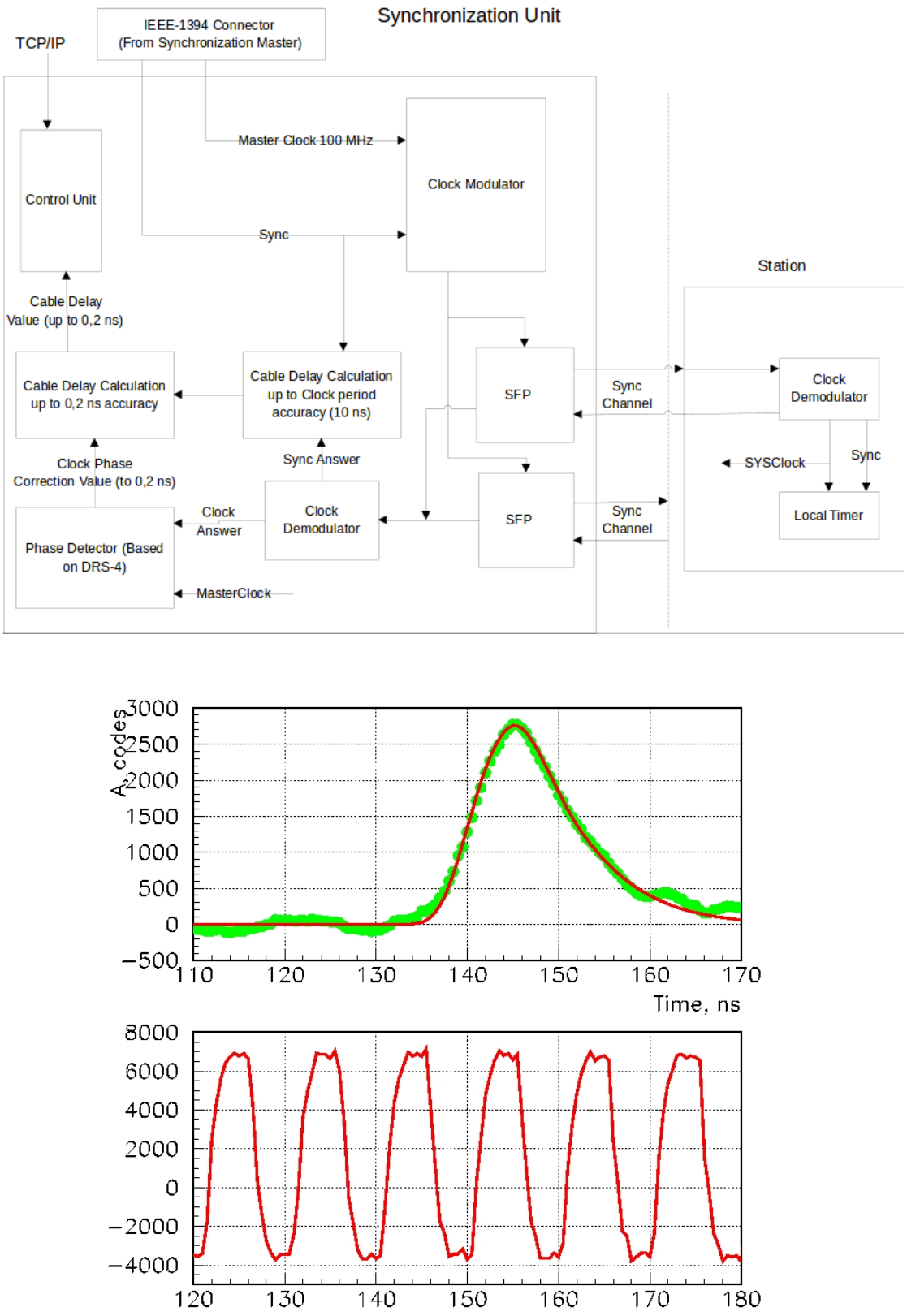

FIGURE 5.4: *Top*: Synchronization unit of DAQ-1 [52]. *Bottom*: Anode pulse (0.5 ns step) and 100 MHz clock recorded by the DRS4.

chip. Both clocks are digitized there, and the phase difference is determined with an accuracy of the digitization of the DRS4 (∼200 ps). Finally, after summing the phase differences of the rough clock and the fine clock, taking into account the signal transmission via optical fiber in both directions, the absolute phase of the local clock in the appropriate station is calculated.

5.2.2 DAQ-2

Data acquisition. The second data acquisition system (Fig. 5.5) is made with two DRS4 evaluation boards and the White Rabbit time synchronization system. Each evaluation board has four inputs. Such a configuration stores 4 anode signals, 1 dynode signal, 1 sum signal and 2 syncs. Every signal is digitized with a step of 1 ns. The DRS4 operates in unipolar mode from 0 V to +1 V.

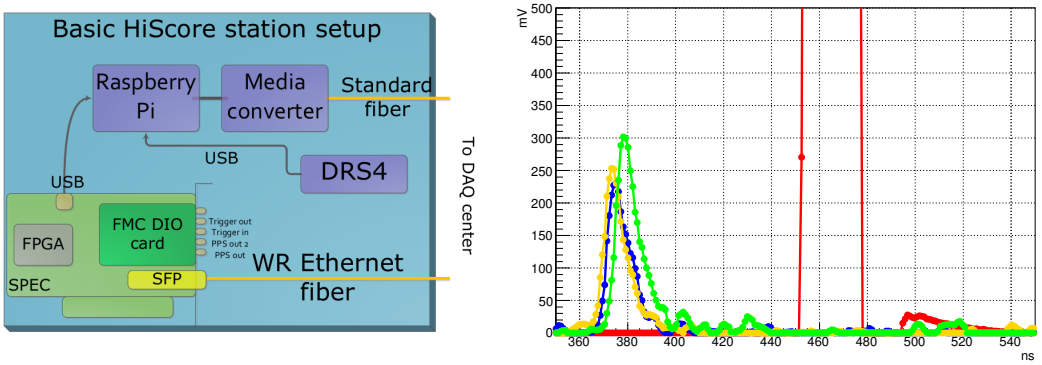

FIGURE 5.5: *Left*: The basic White Rabbit setup [81] WR-node (SPEC card) with WR-fiber, Raspberry Pi and DRS4 evaluation board. *Right*: Three anode pulses (1 *ns* step) and the WR strobe recorded by the DRS4 evaluation board.

Time synchronization. White Rabbit [81] is a new standard for time- and clock-transfer using the extended PTP standard (IEEE 1588) and commercially available basic components. The sum of four PMT signals is sent to a comparator on the WR-SPEC card for a trigger. It generates a trigger if the signal stays above an adjustable threshold for 9 ns [77]. The WR-clock value is latched with ns-resolution and a trigger message is sent via the WR-fiber. When evaluation boards are ready, synchronous SPEC trigger strobes are sent to both DRS4 evaluation boards initiating their readout. The status of the board is indicated by the *ready flag* implemented in the DRS4 readout software. The WR trigger signal is written

to the fist channel of each board, thus the signals in the other three channels can be synchronized relatively to the WR trigger signal.

5.3 Winston cone

5.3.1 Light concentrator

The Winston cone is used as a light concentrator to increase the light sensitive area of the PMT. Such a cone is optimised to collect as much light as possible at angles below the cut-off angle Θ [82]. The cut-off angle depends on the ratio of the upper and lower opening radii R_1 and R_2:

$$\sin\Theta = \frac{R_1}{R_2}. \tag{5.1}$$

Such a light concentrator is characterized by a maximal concentration factor of

$$C_{max} = \frac{1}{\sin^2\Theta}. \tag{5.2}$$

The height of the cone is given by

$$H = \frac{R_1 + R_2}{\tan\Theta}. \tag{5.3}$$

A Winston cone with viewing angle 30° is used now. It has upper and lower opening radii $R_2 = 10\,\text{cm}$ and $R_1 = 20\,\text{cm}$, which results to a height of $H = 52\,\text{cm}$ in this case. Since the ratio of the radii is two, the light sensitive area will be increased by factor four.

5.3.2 Angular acceptance

Preliminary laboratory studies of the cone acceptance show that the supposed cone acceptance does not explain the data well and the acceptance is very sensitive to the PMT position inside the cone. A new ray tracing program was developed, and simulations of angular acceptance of the cone were performed.

For each angle of incident light, 10^4 parallel light rays were scattered uniformly across the upper opening and propagated through the cone. The intensity of a light ray is reduced at each reflection from the surface inside the cone. The cone reflectivity is chosen to be 0.9 independent of angle. The normalised intensity of the light rays at the PMT surface is used to obtain the angular acceptance of the cone. Now, the program includes realistic hemispherical shape of the PMT and the PMT position can be varied. There are three main effects involved.

PMT position variation. Position of the PMT inside the cone can by varied relatively to the cone. According to the PMT datasheet (Appendix B) the height of the PMT cathode is suppose to be 4 cm. There four different positions of the PMT are considered (Figure 5.7): "bottom", "top", "bottom+x", "top–x":

- ▷ "bottom" – bottom of the cathode layer is flushed with the cone bottom,
- ▷ "top" – top of the cathode layer is flushed with the cone bottom,
- ▷ "+x" or "–x" – an additional shift by x relatively to a nominal position,
- ▷ "middle" – somewhere between "top" and "bottom".

Cathode uniformity. Cathode efficiency is not uniform (Fig. 5.6). Here, the cathode efficiency is averaged over the azimuth angle so that only a radial dependence remains.

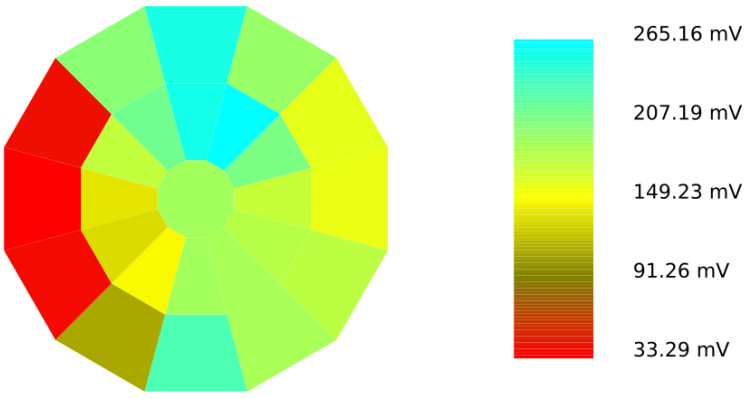

FIGURE 5.6: Photocathode uniformity of the R5912 multiplier [83].

Fresnel losses. Light losses when the rays come from different angles and are reflected from the PMT surface made of glass.

Figure 5.7 shows the predicted angular acceptance of the Winston cone and cumulative solid angle for various positions of the PMT relative to the cone. The effective solid angle Ω can be calculated from the angular acceptance $\varepsilon(\theta)$ using the formula

$$\Omega = 2\pi \int \varepsilon(\theta) \sin\theta d\theta. \tag{5.4}$$

It is clearly seen how the angular acceptance is "sensitive" to such a focusing. Two main remarkable features were observed: a "dip" ($\theta = 0°$) and a "kink" ($\theta > 30°$).

In an extreme case, when the PMT is deeply inside the cone ("bottom + x") the kink is located much above 30° and the dip is prominent. Moving the PMT from "bottom" to "top" improves the situation. The dip flattens and the kink is less prominent. In the opposite extreme case ("top – x"), the solid angle becomes much smaller and the PMT is positioned outside the cone, which is not recommended too.

The solid angle lies within the range from 0.3 sr to 0.7 sr for both extreme cases. And only in a "middle" position the solid angle results in the expected value of 0.58 sr. Thus, some middle position (somewhere between "top" and "bottom") seems to be ideal. This rule, place a PMT in the middle position, should be followed when the PMT is deployed into the Winston cone.

5.4 Photomultiplier

The array is built on the basis of 8-inch photomultipliers with hemispherical bialkali (K_2CsSb) photocathode. There are two PMT models which are available now: 9352KB by Electron Tubes and R5912 by Hamamatsu (Appendix B). The photomultipliers are designed for using in Cherenkov and scintillation experiments in cosmic ray physics. At the first stage, the HiSCORE-9 array was fully equipped with Hamamatsu PMTs. Next optical stations will be built from the Electron Tube PMTs.

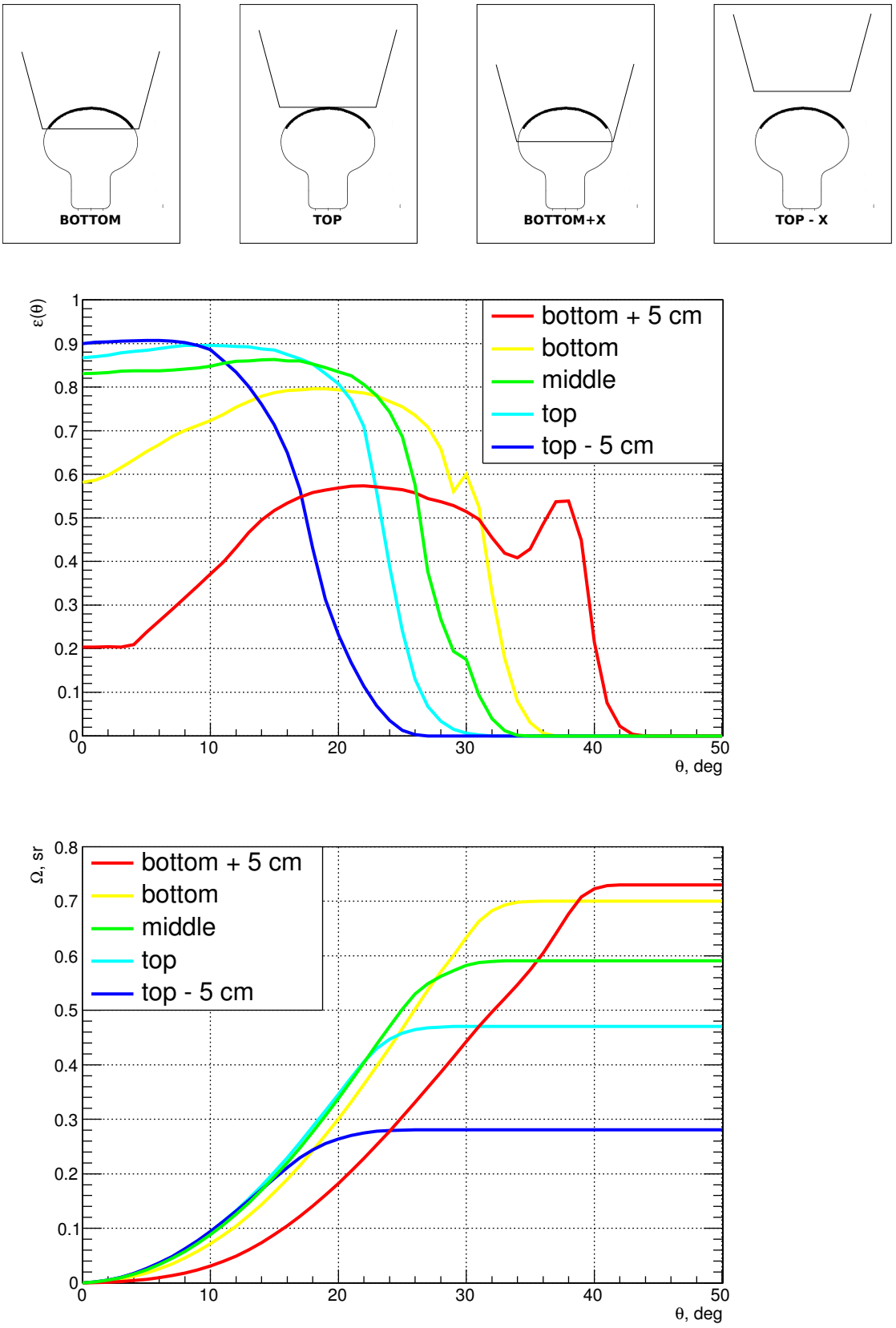

FIGURE 5.7: Angular and cumulative acceptance of the Winston cone for various PMT positions.

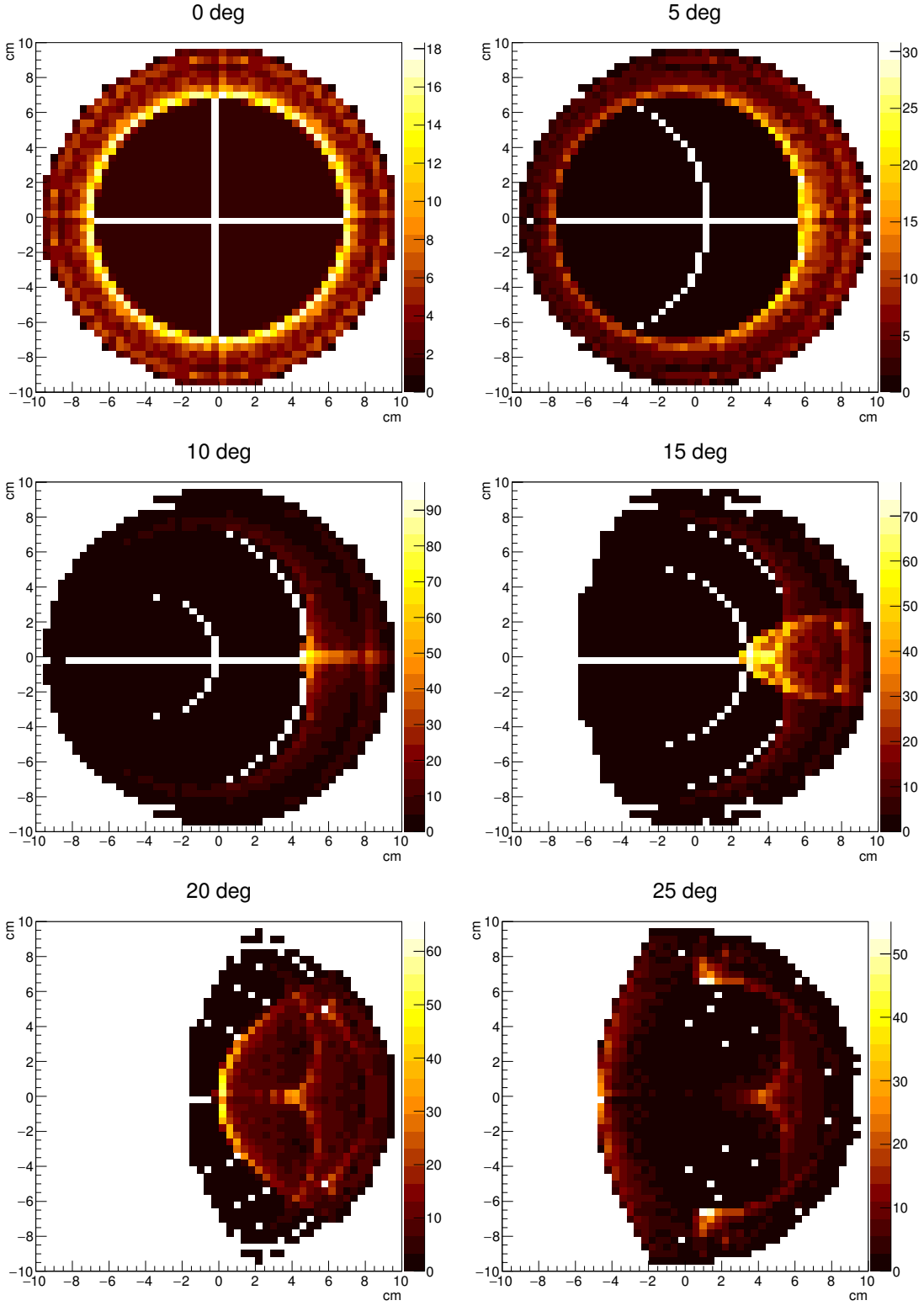

FIGURE 5.8: Simulated intensity distribution of light at the surface of the PMT intside the Wistone cone for various incident angles. The intensity is given by a relative color scale.

The photomultiplier tube is made of borosilicate glass. These photomultipliers contain high-performance box-like first dynodes with large area and the subsequent trough-shaped dynode systems with linear focusing.

The first dynode of the photomultiplier R5912 is made of sprayed CsSb material with a high coefficient of secondary emission larger than 10. The remaining dynodes are emitters made of CuBe alloy. The surface area of the last dynodes is increased in order to ensure stability of a photomultiplier under the light background from the night sky as well as to ensure high linearity of the photomultiplier. The total number of dynodes in the device is 10, which allows to get a gain of G$\sim 10^7$. R5912 has excellent single photoelectron characteristics. The peak/valley ratio of the single photoelectron spectrum is not less than 2.5. The transit time of photoelectrons through the PMT has a width at half-maximum of 3 ns.

The number of stages in the dynode system of ET9352KB is limited to 6. All dynodes are made of CuBe alloy. For reliable operation under the background light from the night sky, thin conductive strips of aluminium with a width of 1 mm are sprayed under the photocathode. The gain of the photomultiplier G$\sim 10^4$ is achieved at an operating voltage of 1400 V. The small number of dynodes leads to a good response time of the photomultiplier. The anode pulse rise time is less than 5 ns. Even with this PMT a good single photoelectron characteristic can be also achieved using fast trans-impedance amplifiers.

Both models work reliably under constant anode currents up to 100 μA. The ET9352KB model has less gain due to low number of dynodes and will be less vulnerable to the night sky background light.

5.4.1 Quantum efficiency

A typical quantum efficiency of the PMT with bialkali photocathode is shown in Fig. 5.9. The quantum efficiency reaches a maximum at $\lambda = 340 - 400$ nm and drops sharply to almost zero at $\lambda = 280$ nm due to the light transmission of the PMT glass. Above 400 nm the quantum efficiency extends smoothly up to 650 nm.

The Cherenkov spectrum at the ground level drops above 300 nm as λ^{-2}. At short wavelengths, the spectrum is modulated by the light attenuation in the atmosphere. Some of the emitted Cherenkov light at short wavelengths remains unregistered, that leads to an increase of the energy threshold of the detector. This

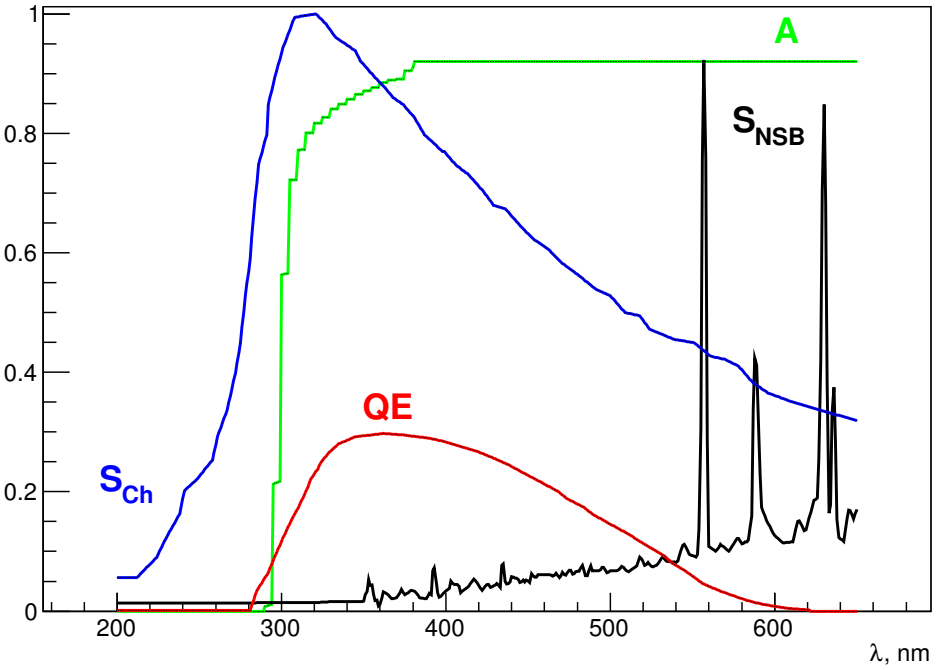

FIGURE 5.9: Quantum efficiency $QE(\lambda)$ of the 9352KB photomultiplier as a function of wavelength of the incident light. $A(\lambda)$ represents the acrylic glass transmission. The spectrum of the night sky $S_{\mathrm{NSB}}(\lambda)$ and the attenuated Cherenkov spectrum $S_{\mathrm{Ch}}(\lambda)$ are shown as well.

can be improved by using wavelength shifters, which absorb shorter wavelength photons in $200 - 300\,\mathrm{nm}$ and emit longer wavelength photons within the PMT sensitive range.

Two average quantum efficiencies, for Cherenkov light and for the night sky background, were calculated here. These quantum efficiencies were found by averaging the quantum efficiency QE of ET9352KB (see Appendix B) over the sensitive wavelength range of the PMT and the spectrum of the corresponding light source: the Cherenkov light spectrum (S_{Ch}) [55] or the spectrum of the night sky background light (S_{NSB}) [84]. In addition, the light transmission by the acrylic glass of the detector entrance window (A) [52] is taken into account as an additional reducing factor:

$$\overline{QE}^{\mathrm{ET}}_{\mathrm{Ch}} = \frac{\int_\lambda QE(\lambda) S_{\mathrm{Ch}}(\lambda) A(\lambda) d\lambda}{\int_\lambda S_{\mathrm{Ch}}(\lambda) A(\lambda) d\lambda} = 0.19 \text{ p.e./ph}, \tag{5.5}$$

$$\overline{QE}^{\mathrm{ET}}_{\mathrm{NSB}} = \frac{\int_\lambda QE(\lambda) S_{\mathrm{NSB}}(\lambda) A(\lambda) d\lambda}{\int_\lambda S_{\mathrm{NSB}}(\lambda) A(\lambda) d\lambda} = 0.08 \text{ p.e./ph.} \tag{5.6}$$

The quantum efficiency of both PMT models are quite similar except the maximal quantum efficiency (ET9352KB – 0.30 p.e./ph, Hamamatsu R5912 – 0.22 p.e./ph). Thus, a simple scaling of the found average quantum efficiencies can be applied for the R5912 model, that gives the following results: $\overline{QE}^{\mathrm{Ham}}_{\mathrm{Ch}} = 0.14$ p.e./ph and $\overline{QE}^{\mathrm{Ham}}_{\mathrm{NSB}} = 0.06$ p.e./ph.

5.4.2 Collection efficiency

One other important parameter of photomultiplier is the *collection efficiency* (CE). The collection efficiency is defined as the probability that a produced photo-electron reaches the active area of the first dynode. This is usually better than 0.8–0.9 [85]. In our case, the PMT of such a type with the large photocathode of hemispherical shape is expected to collect electrons less efficiently than small flat PMTs. In this work, the collection efficiency is assumed to be 0.8 within the relevant photomultiplier wavelength range, that seems to be realistic.

5.4.3 Afterpulsing

Despite the fact that the photomultiplier tube is an excellent photodetector with high characteristics, it has a parasitic effect, called *afterpulsing* or *ion feedback*. Afterpulses are spurious pulses with the same pulse shape, but increased amplitude that appear after the true ones with the rate

$$R_{a.p.} \propto e^{-c_a A} \tag{5.7}$$

at the threshold A.

An electron from the photocathode may collide with the rest of the gas which is contained in the volume or is adsorbed on the surface of the dynode material. Formed in this way ions will be accelerated towards photocathode where they will release many photoelectrons. Afterpulses typically have the same amplitudes as the normal ones, but with a pulse delay. Their delay with respect to the ionising

electron is in the range from a few hundred ns to a few μs [86]. Thus, afterpulses do not affect the trigger system behaviour for air showers, but they increase the trigger rate due to night sky background.

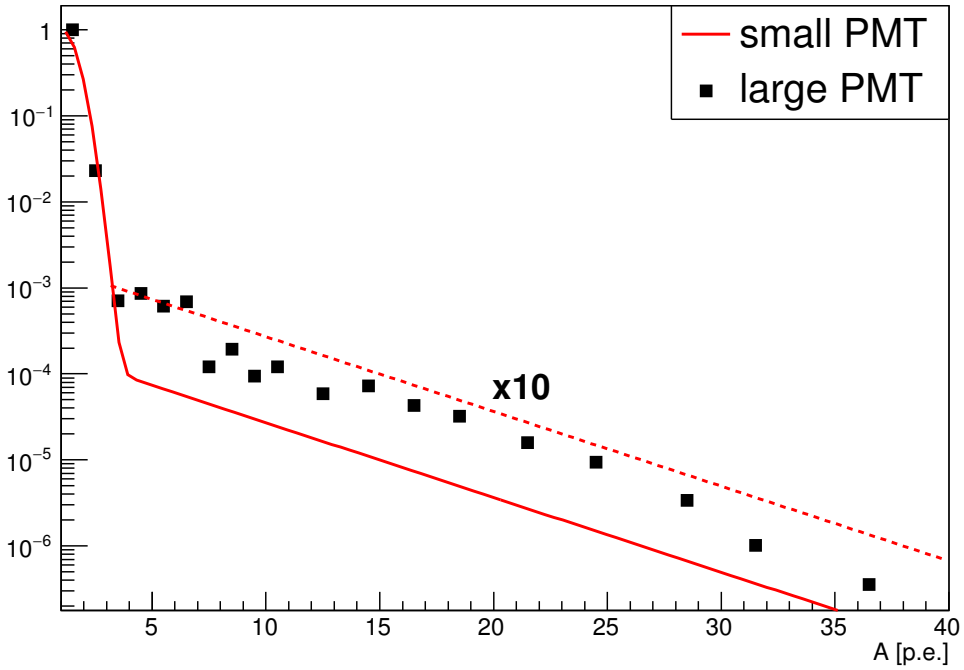

FIGURE 5.10: Single photoelectron pulse amplitude distribution including afterpulse probability. The comparison is given for small [55] and large [87] PMTs.

Figure 5.10 shows the amplitude distribution of the photo-electron pulses and its afterpulses, i.e. the probability that a single photoelectron causes an amplitude A. Following the approach of sim_telarray [88] this probability can be approximated by a Gaussian function ($\mu = 1\,\text{p.e.}$, $\sigma = 0.6\,\text{p.e.}$) with an exponential tail, characterizing the afterepulsing. However, the afterpulsing rate applied to small PMTs in this original approach is underestimating reality, and for a large PMT it has to be enlarged by a factor of 10 [87], resulting in:

$$P(A) = \exp\left(-\frac{1}{2}\left(\frac{A-1}{0.6}\right)^2\right) + 2 \cdot 10^{-3} \exp\left(-\frac{A}{5}\right). \tag{5.8}$$

5.4.4 Dark current

DC current through the anode of the photomultiplier caused by night sky background light must be kept below respective maximum ratings of the PMT. For

both PMT models, R5912 and 9352KB, being used for HiSCORE the maximum allowed current is 100 μA. Six stages of the PMT should provide a gain of $10^4 - 10^5$ at the nominal applied voltage.

Dark current corresponding to the night sky background rate R_{NSB} will be

$$I_{\mathrm{NSB}} = R_{\mathrm{NSB}} \cdot e = 15 \text{ GHz } \cdot 1.6 \cdot 10^{-19}\ C \simeq 2.4 \text{ nA}. \tag{5.9}$$

Thus, the gain must be less than

$$G_{max} = 100\ \mu\text{A}/2.4 \text{ nA} = 4.2 \cdot 10^4. \tag{5.10}$$

If the anode is connected through the coupling capacitor to a transmission line terminated in 50 Ω, the voltage developed across this load is given by:

$$U_{\mathrm{NSB}} = I_{\mathrm{NSB}} \cdot R = 100\ \mu\text{A} \cdot\ 50\ \Omega = 5 \text{ mV (or 0.33 mV/p.e.)}, \tag{5.11}$$

Finally, signal fluctuations caused by NSB fluctuations with a standard deviation of $\sigma = \sqrt{15}$ p.e./ns can be found as:

$$\delta U_{\mathrm{NSB}} = 1.24 \text{ mV}. \tag{5.12}$$

Using an pre-amplifier with an amplification factor of 20, signal fluctuations of 25 mV are expected to be registered. This estimate is very close to the experimental value, where the noise with a magnitude of 50–100 mV were typically observed. The difference may be explained by additional electronic noise.

5.5 Detector response

Each photoelecton emitted from the photocathode of the PMT produces a characteristic voltage pulse, called photomultiplier response. The present today PMTs are very fast and such a response is typically 3–5 ns. In addition, the detector readout system, mostly due to cables and pre-amplifiers, contributes in the response as well. Following this, the total response can be called *detector response*.

The resulting detector response is shown in Fig. 5.11. The characteristic voltage pulse was measured with the oscilloscope using a fast LED source (0.5 ns) in the laboratory during the regular PMT calibration before its deployment on Tunka site. The set-up included the PMT R5912, the pre-amplifier and 5 m cable.

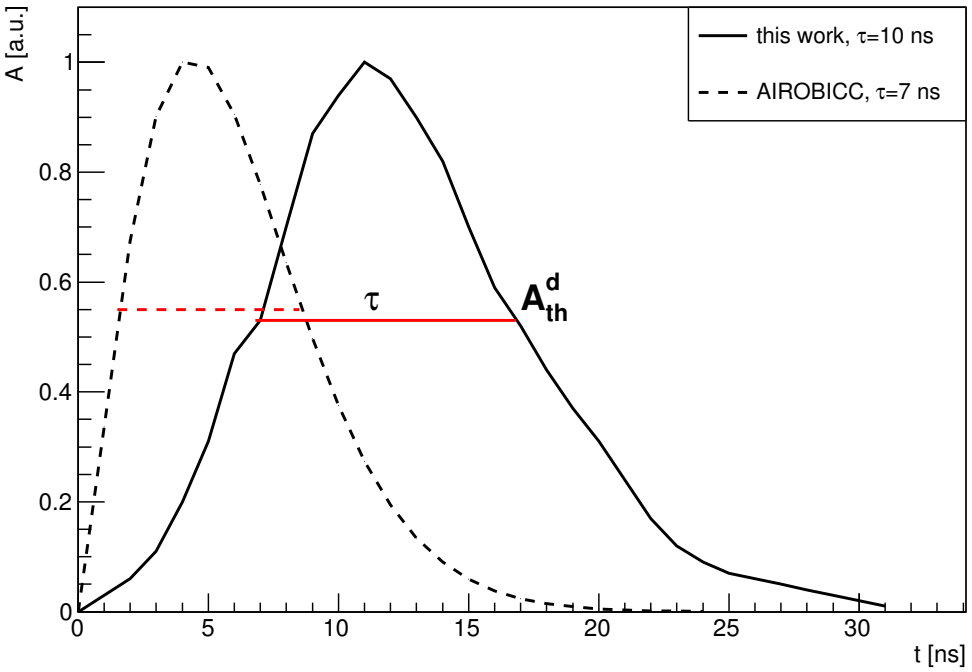

FIGURE 5.11: The HiSCORE detector response. Signal shape was measured with the oscilloscope using a fast LED source. The AIROBICC response [89] is shown as well.

The pulse shape can be described by the following parametrization:

$$f(t) = Ct^a e^{-bt}, \tag{5.13}$$

with

$$C = 6.3 \cdot 10^{-4},$$

$$a = 5.3,$$

$$b = 0.48 \text{ ns}^{-1}.$$

The detector response plays an important role in Monte Carlo studies and usage of this characteristic has some important peculiarities.

First, if the peak value of the response is scaled to 1, all pulse amplitudes will be measured in physical related units (e.g. photoelectrons). In comparison, if the integral of the response pulse is normalised to 1, integral quantities in turn become physical. Thus, the normalisation factor I_n, which is the integral of the pulse, should be known to transform one formulation to another.

The second major parameter of the detector response is associated with the trigger logic of the detector. Every discriminator has a minimal time for triggering. It requires for a signal to stay above the threshold during this time. For both our data acquisition systems (DAQ-1 and DAQ-2) this time is about 10 ns. It leads to a more realistic definition of the detector threshold – *discriminator threshold*, which is $A^d_{th} = C_\tau \cdot A_{max}$. The pulse constants I_n and C_τ for both shown detector responses are summarised in the following table:

	AIROBICC [89]	this work
I_n	7.94	11.74
C_τ	0.55 (7 ns)	0.53 (10 ns)

It should be noted, that the measurements were done with the bright LED source, illuminating many photons. The detector response in the single photoelectron mode remains unknown and may be different. Thus, this problem must be investigated in future.

5.6 Detector calibration

A preliminary detector calibration was carried out in February and March 2014 [77, 90]. It included 5 runs during three days: 22.02, 25.02, 07.03. A bright wide-angle LED light source was positioned outside the array perimeter ($\sim$ 200 m), emitting light pulses with a frequency of 6 Hz towards all the 9 stations. The light was collected by reflectors placed at an angle of 45 degrees on top of each station.

5.6.1 Time calibration

The timing performance of both data acquisition systems (DAQ-1 and DAQ-2) was studied at first. The method is pretty simple and consists in the following.

By knowing the position of the source relatively to the array and applying an approximation of signal propagation by a spherical front model, front residuals will provide a time resolution of the system. The results obtained in both cases are shown in Fig. 5.12. DAQ-1 exhibits a time jitter of 190 ps, whereas DAQ-2 has a time jitter of 460 ps.

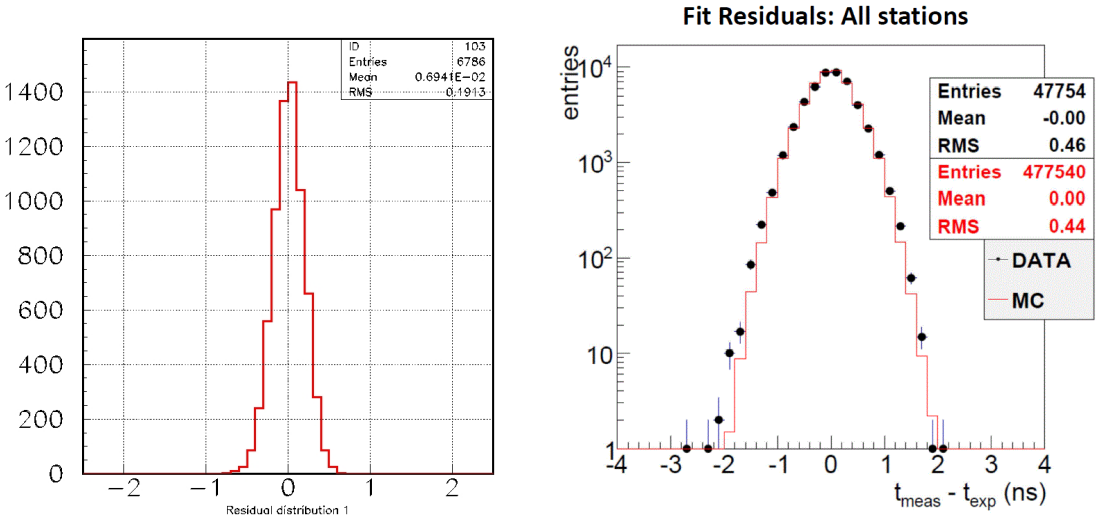

FIGURE 5.12: LED time calibration: DAQ-1 (*left*) [75] and DAQ-2 (*rigth*) [77]. Time residuals with respect to geometrical front are shown.

A possible explanation for the difference between two synchronization systems might be, that in case of DAQ-1 the constant fraction discriminator has been used. Constant fraction discriminator means, that the exact trigger time of the pulse is assigned always to a certain moment within the pulse rise, which is usually the half maximum. This results to a more accurate timing.

5.6.2 Amplitude calibration

The absolute amplitude calibration was done with the *excess noise factor* method [91]. Amplitude of the pulse in the evaluation board resulting from the LED source varies. Such an amplitude distribution obtained from the variation of the signal height allows to extract the number of photoelectrons in this distribution. Assuming that the number of photons falling on the photocathode has a Poisson variance and noise variance is negligible, one can derive the conversion factor:

$$C = F\frac{\mu}{\sigma^2}\ \text{[p.e./a.u.]}, \tag{5.14}$$

where F is the excess noise factor of the PMT, σ is the measured variance and μ is the mean of the LED amplitude distribution in units (a.u.) of the data acquisition system[1](see Figure 5.13).

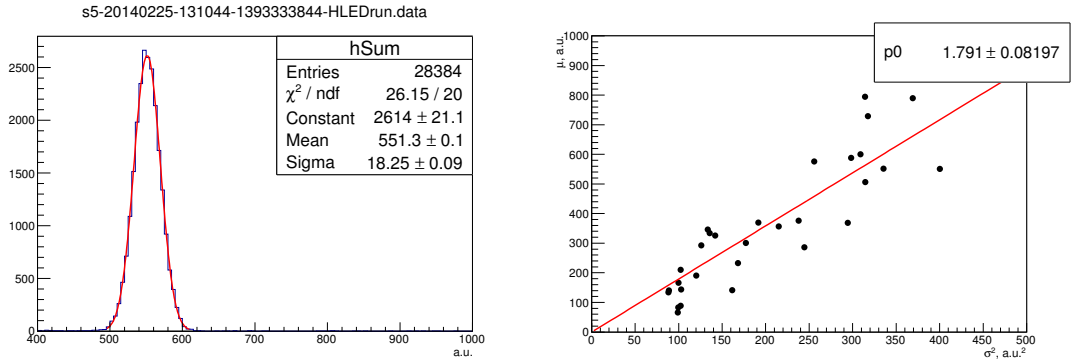

FIGURE 5.13: An example of the LED amplitude distribution and its fit by Gaussian (*left*). Summary scatter plot of σ^2 and μ of sum-channels (*right*). The data of all runs are shown.

The mean μ_1 and the standard deviation σ_1 of the single photoelectron spectrum (with subtracted pedestal) is related to the excess noise factor of the PMT by the following definition [92]:

$$F = 1 + \frac{\sigma_1^2}{\mu_1^2}. \tag{5.15}$$

Direct measurements of F in the laboratory using our PMTs are difficult due to their low gain. An alternative developed in this work would be to use the gain for an estimate of F [90]. Let us try to determine the F value.

The excess noise factor is related to the collection efficiency of the photomultiplier CE and the secondary emission ratio δ [85] (Eq. 4-25):

$$F = \frac{1}{CE}\left(1 + \frac{1}{\delta_1} + \frac{1}{\delta_1\delta_2} + ... + \frac{1}{\delta_1\delta_2...\delta_n}\right), \tag{5.16}$$

where δ_i is the secondary emission ratio of the i-th dynode and n is total number of dynodes.

The secondary emission ratio is proportional to inter-dynode voltage [85] (Eq. 4-3),

$$\delta_i = const \cdot (U_i)^{\kappa}, \tag{5.17}$$

[1]All channels are measured in millivolts (mV) except the sum signal which is dumped by a factor of 2.2 in the summator (mV/2.2). 8.192 codes of DAQ-1 correspond to 1 mV of DAQ-2.

where U_i is the voltage between the $(i-1)^{th}$ and the i^{th} dynode, κ is an exponent varying from 0.7 to 0.8, and the constant is inferred from the gain:

$$G = CE \cdot \prod_{i=1}^{N} \delta_i, \tag{5.18}$$

where N is the total number of stages. Thus the mean value of the secondary emission coefficient is a function of gain, ratio of resistors and exponent κ [93]

$$\delta_i = \left(\frac{G}{CE \cdot \left(\prod_{i=1}^{N} R_i \right)^{\kappa}} \right)^{1/N} \cdot (R_i)^{\kappa}, \tag{5.19}$$

where the ratio of resistors $R_1 : R_2 : \ldots R_n$ is the same like the ratio of the applied voltages $U_1 : U_2 : \ldots U_n$. Using this equation we can find the secondary emission coefficient for each dynode and, thus, the noise factor F.

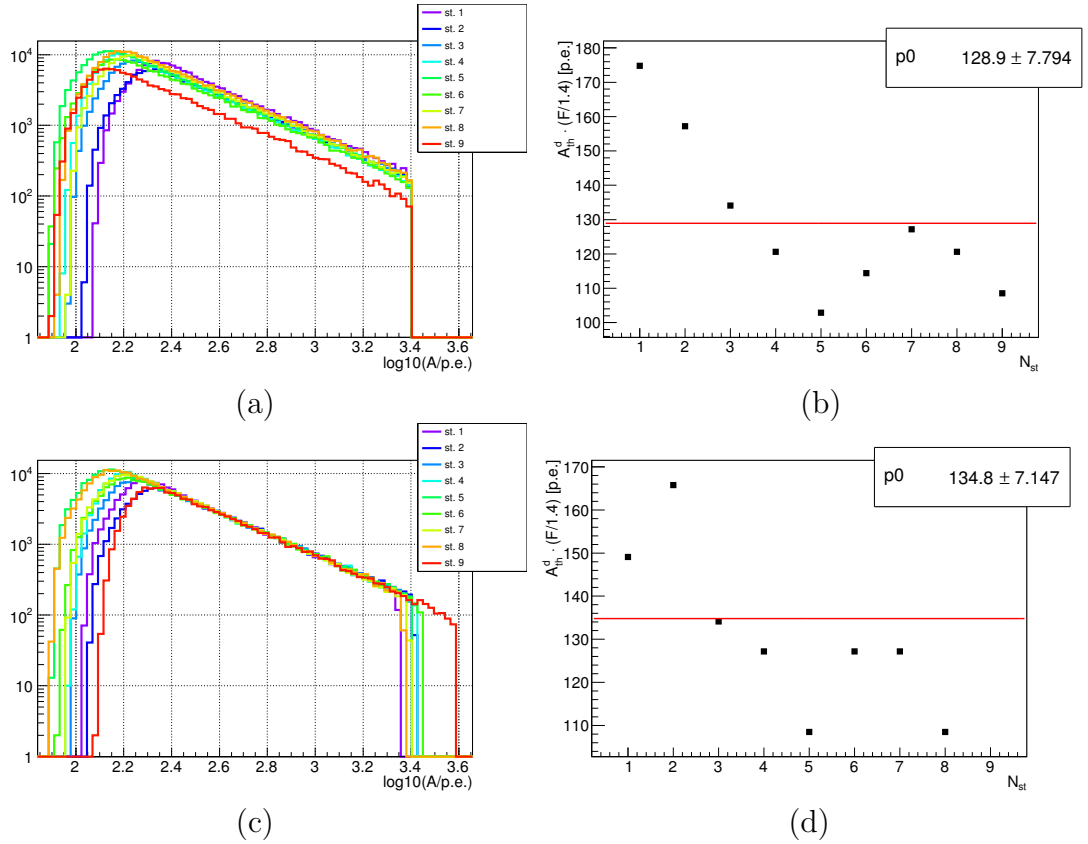

FIGURE 5.14: Raw integral spectra of sum-channels calibrated from units of the DAQ-2 to photoelectrons (*left*) and average discriminator thresholds A^d_{th} for nine stations (*right*). (a, b) Spectra after applying the common conversion factor C=2.5 p.e./a.u. (c, d) Spectra after applying the same conversion factor C and the additional relative calibration. Station threshold is defined at the level of 1/2 from the maximum of the spectrum.

The results of the calculation of the factor F for realistic parameters ($\kappa = 0.75$, $G = 10^4$, CE=0.8) are given in the table below. The ratio of resistors is taken from datasheets of both PMTs (Appendix B). For PMT ET9352KB an applied voltage of 1.4 kV is assumed.

R5912 (first 6 stages)	ET9352KB
$R : 11.3 : 0.6 + 3.4 : 5 : 3.33 : 1.67 : 1$	$R : 4.5 : 1 : 1 : 1 : 1 : 1$
$\delta_1 = 12.2$ $\delta_2 = 5.6$ $\delta_3 = 6.6$ $\delta_4 = 4.9$ $\delta_5 = 2.9$ $\delta_6 = 2.0$	$\delta_1 = 11.9$ $\delta_{2..6} = 3.8$
$F = 1.37$	$F = 1.39$

The results of absolute amplitude calibration are shown in Fig. 5.14.The panels *a* and *b* represent spectra with the common conversion factor 2.5 [p.e./a.u.]. Here, the average ratio $\mu/\sigma^2 = 1.8$ was used and the F factor was assumed to be 1.4. As it clearly can be seen, the amplitude spectra are still not well calibrated and some additional relative calibration might be applied (*c*, *d*). The spectra were additionally calibrated relatively to a mean spectrum. Nevertheless, both approaches give similar average detector thresholds (the asterisk marks the additional relative calibration):

$$\begin{aligned} A_{th}^{d} &= (129 \pm 8)\left(\frac{F}{1.4}\right) \text{ [p.e.]}, \\ A_{th}^{d*} &= (135 \pm 7)\left(\frac{F}{1.4}\right) \text{ [p.e.]}. \end{aligned} \tag{5.20}$$

A preliminary detector threshold of 130–135 p.e. obtained in this analysis probably gives only a lower estimate on the threshold, since the absolute value strongly depends on F and in reality it can be higher than 1.4. Moreover, both involved in the analysis quantities, μ/σ^2 and F, must be measured reliably for every run. Although accurate measurements of μ/σ^2 are not a problem, measurements of F is still technically difficult.

5.7 Array performance

In this section, an analysis of the data collected during the first season of operation of the HiSCORE-9 array (2013–2014) will be given. The analysis includes results of the preliminary data reconstruction and the array performance done with the chessboard method will be shown.

DAQ-2 was build specifically to explore the White-Rabbit synchronization system and to provide necessary data cross-checks. Unfortunately, the data from this system are not suitable for fully reconstruction due to technical reasons. However, this can be done with the data collected by DAQ-1.

5.7.1 Data processing

Statistics. The experimental statistics of DAQ-1 consists of 84 hours of data collected during 13 nights in February, March and April 2014 [94]: 21.02, 25.02, 26.02, 27.02, 28.02, 05.03, 06.03, 26.03, 27.03, 29.03, 30.03, 02.04, 03.04.

Calibration. For data from DAQ-1, a *composite sum* was used for reconstruction. This composite sum was built offline from individual signals of four channels of each optical station. First, the relative inter-channel amplitude and the time calibration were applied (these methods were already described in Sect. 4.2). Finally, individual channels were summed up and proceed to a reconstruction.

Fig. 5.15 exhibits the ratio between composite sums of dynodes and anodes of the stations over days. It shows an average anode/dynode ratio of 29 ± 2, that is very close to the expected value 30. Average slope of the integral spectrum is about -1.6. The obtained values are stable with time except station 4 (5th night, 28.02). During this night it seems that the station had problems with the high voltage.

Reconstruction. The data were reconstructed with a program `ang_his4aa`, which is based on the same algorithms used for Tunka-133 (see Sect. 4.3). Its structure is given in Fig. 5.16. The events were selected with the zenith angle $\theta < 25^\circ$ and with the core position inside four cycles with a radius of 75 m inside each quadrant of the 9-station array. As a result, about 145,000 events were selected.

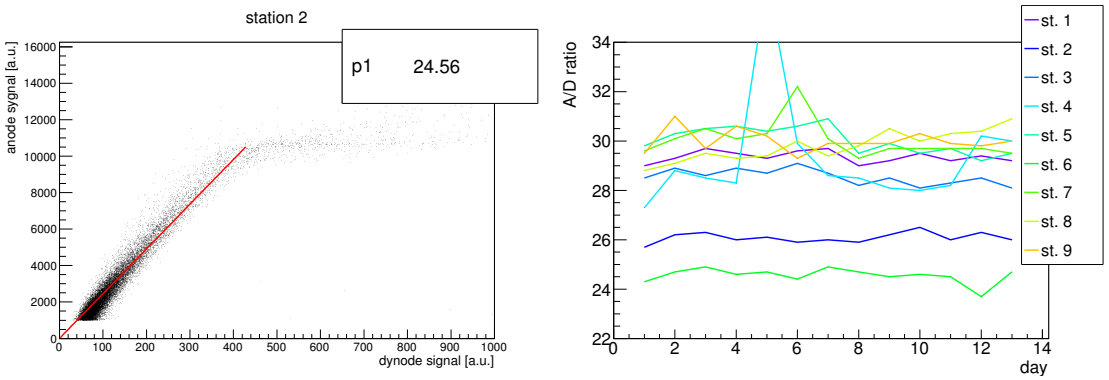

FIGURE 5.15: *Left*: Anode/dynode ratio of the composite sum for a single station. *Right:* Anode/dynode ratios of the 9 stations for various days.

The resulting differential spectrum is shown in Fig. 5.17 [95]. The array reaches 100% efficiency at 300 TeV: 21,000 events above 1 PeV and 200 events above 10 PeV. The spectrum below the knee can be fit by a power-law with $\gamma = -2.65$, and also represents the compound knee (see Sect. 4.4.2). The results obtained with HiSCORE-9 are in good agreement with the Tunka-25 spectrum shown before (Fig. 4.8) and with other CR experiments.

It should be noted, that the reconstruction procedure demonstrates excellent characteristics (Fig. 5.18): front residuals $\sim$ 470 ns and the shower cores inside the chosen cycles are uniformly distributed. Besides that, the cone shows a very good angular acceptance up to 30°, which is the expected cut-off angle of the cone.

5.7.2 Chessboard method

The accuracy in determination of shower parameters can be estimated using the well known *chessboard* method [8]. The method consists in the following. The experimental array is divided into two subarrays of equal size. Parameters of a given shower are determined independently with each of the two subarrays. The accuracy of determination of one of the parameters is given by the difference between the two reconstructed values divided by $\sqrt{2}$ because they represent two independent determinations of the same shower parameter. Finally the accuracy of a parameter x is given by

$$\sigma_x = \delta x/\sqrt{2}. \tag{5.21}$$

In our case, the 9-station array was divided into two quasi-independent subarrays in the following way (see Fig. 5.19):

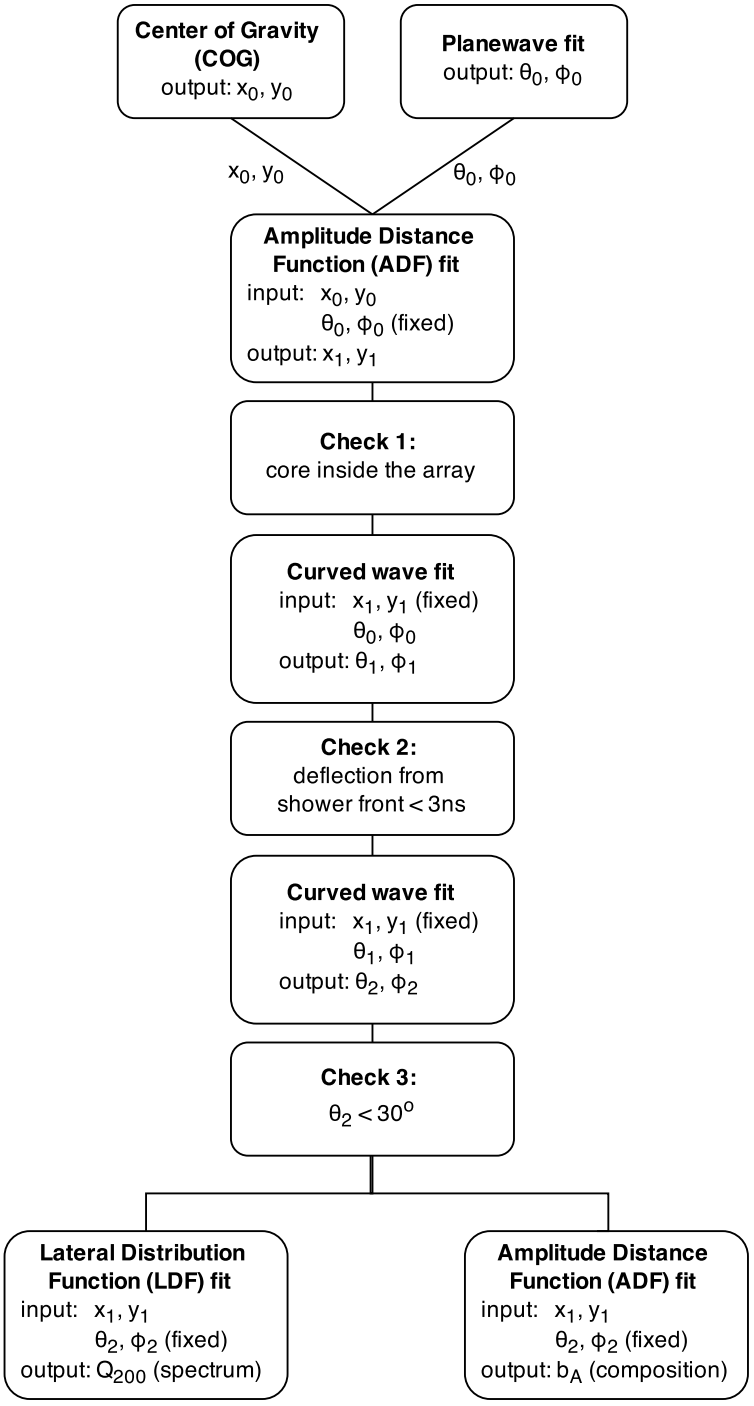

FIGURE 5.16: Reconstruction strategy used in the `ang_his4aa` program.

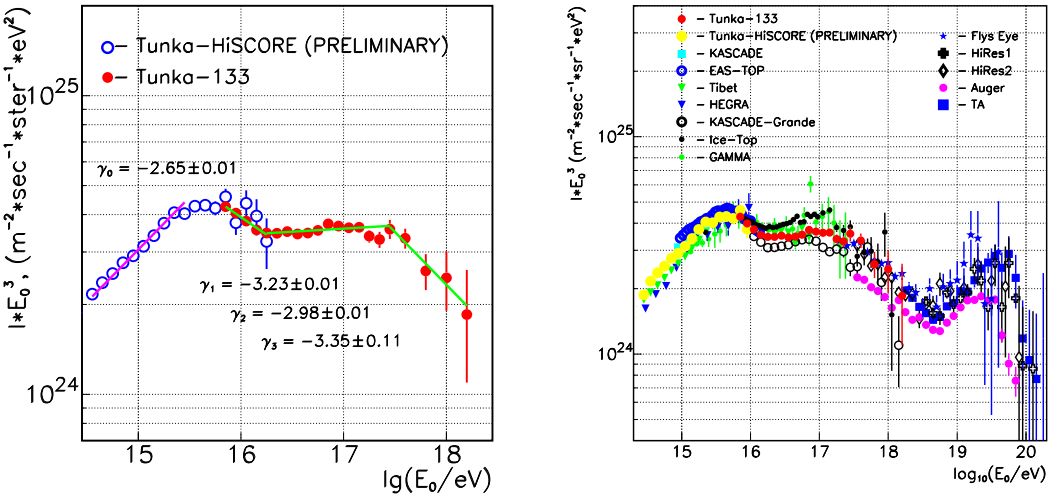

FIGURE 5.17: Differential primary energy spectrum of cosmic rays obtained with the HiSCORE-9 array [95]. *Left*: 1 year of HiSCORE-9 data in comparison with 5 years of Tunka-133 data. *Right*: Comparison with other CR experiments.

Subarray 1: 1, 6, 7, 9, 5 stations,

Subarray 2: 1, 3, 4, 8, 2 stations.

Such a dividing seems appropriate. It allows to keep a similar spacing between detectors of 150 m as for the full array and to divide the array in a symmetric way with the common central detector.

Data of each subarray were reconstructed with the reconstruction program `ang_his4aa`. The results obtained with the chessboard method are shown in Fig. 5.20. It represents the accuracy in determination of the four main shower parameters: core position, arrival direction, energy and depth of the shower maximum.

An additional cut, $b_A > 6$, on the parameter of the steepness of the amplitude distance function was applied here. It permits to control the goodness of fit when the ADF is used. As a result, about 3,100 matched events were found. The analysis revealed the following accuracies: arrival direction – 0.04°, core – 3 m, energy – 5%, and shower maximum – 27 g/cm^2. The obtained distributions look good except the distribution of the shower depth. It is not centered and this may hint that two subarrays are not fully identical.

When disable cut on b_A, the number of matched events becomes about 12,400 and the accuracies in this case are: arrival direction – 0.12°, core – 12 m, energy – 18%. However, the form of the obtained distribution for energy is questionable. It has

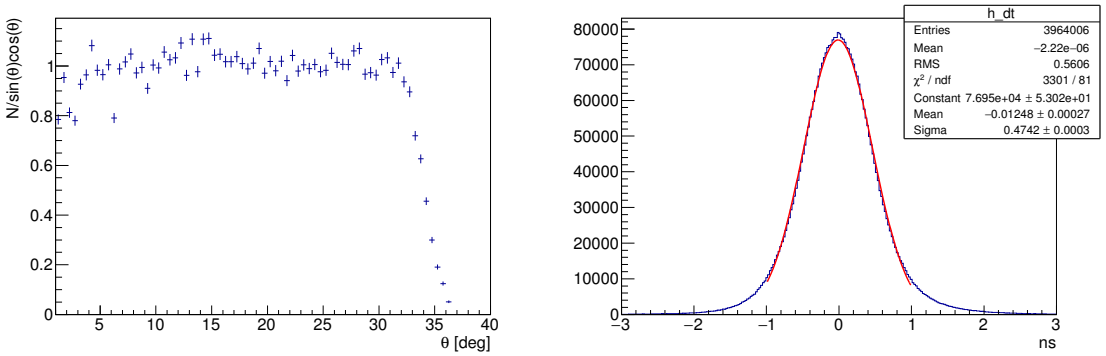

(a) (b)

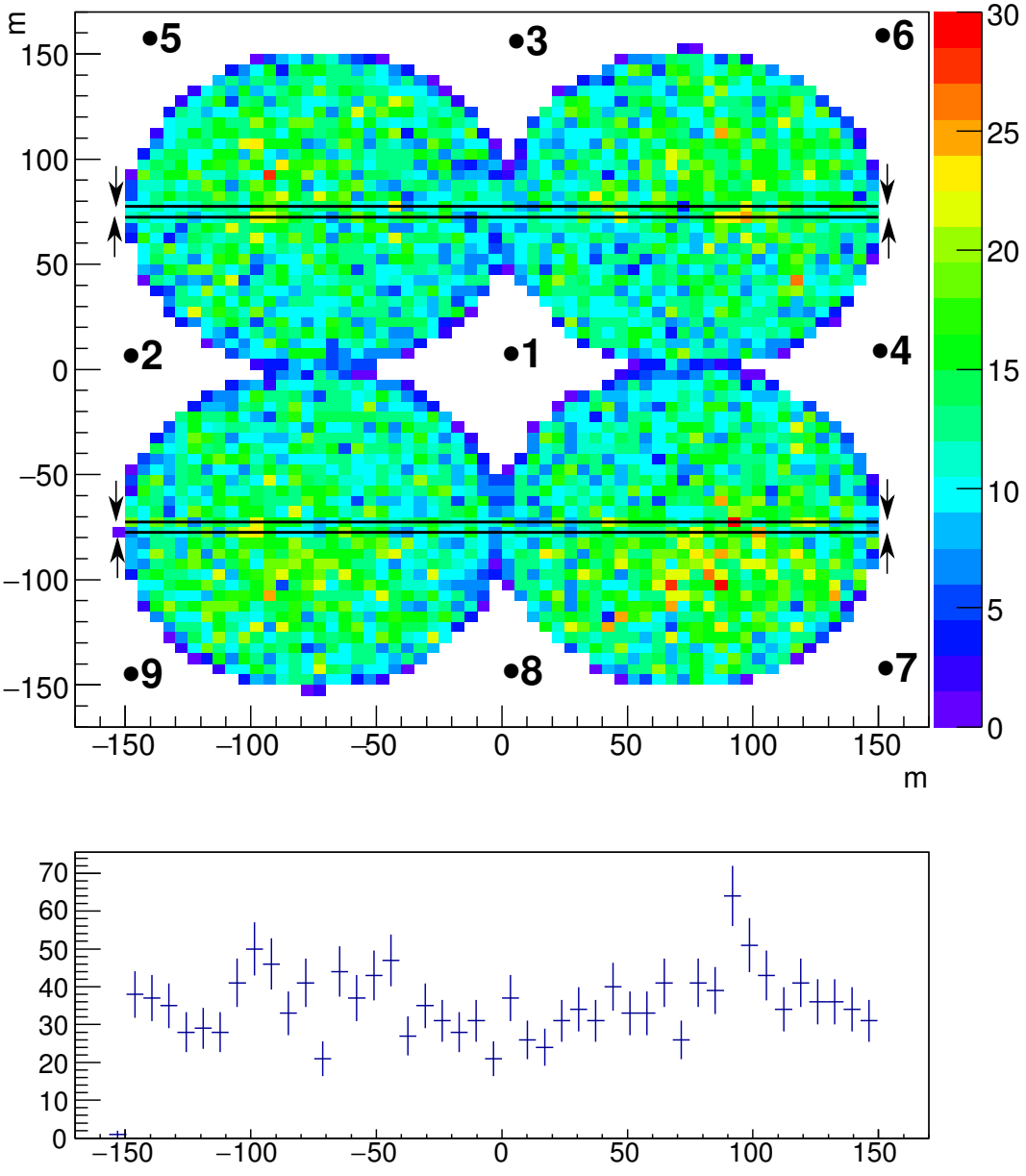

(c)

FIGURE 5.18: (a) Distribution of showers over the zenith angle ($E > 1$ PeV). (b) Front residuals (all data). (c) Reconstructed shower cores and the slice along the horizontal axis ($E > 1$ PeV).

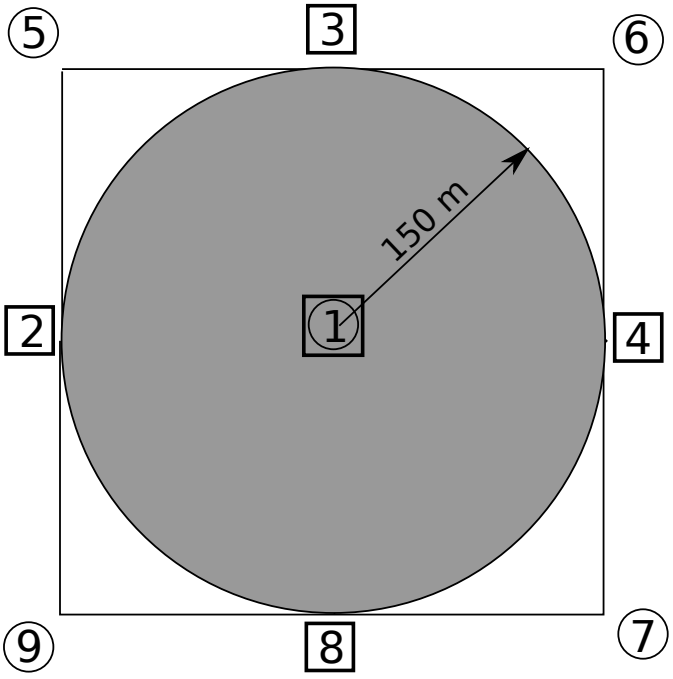

FIGURE 5.19: Array dividing scheme.

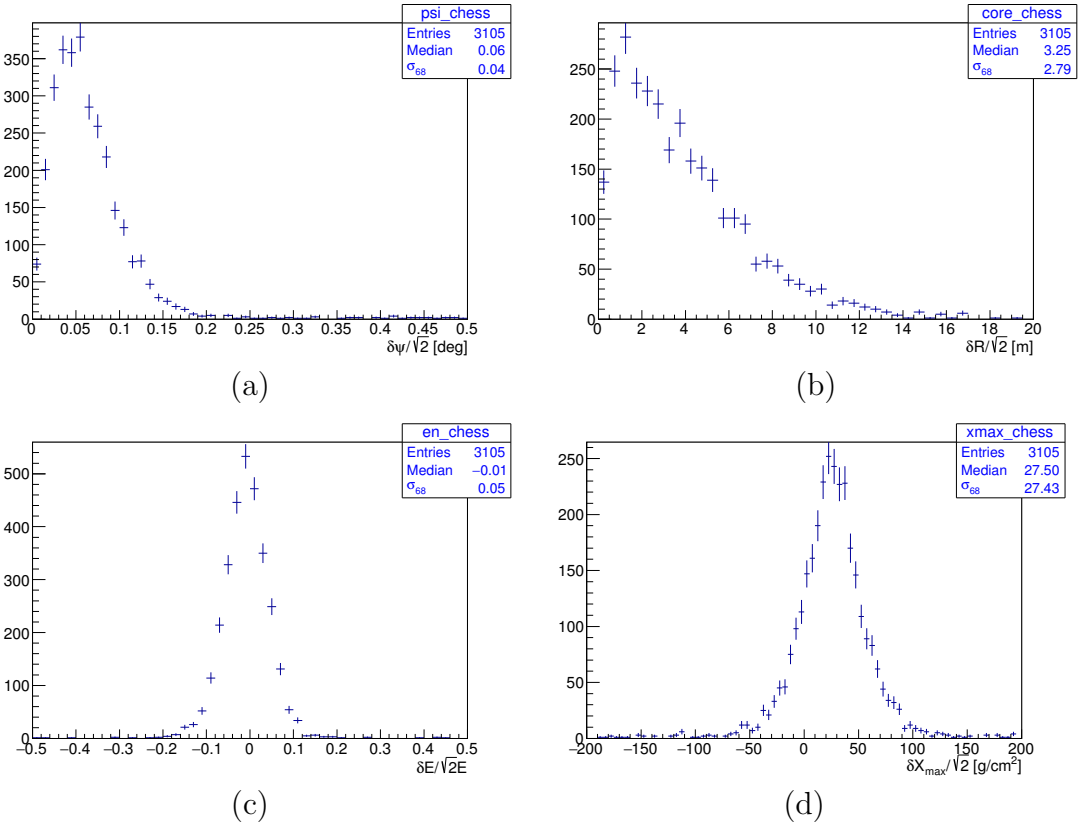

FIGURE 5.20: Results obtained with the chessboard method. Arrival direction (a). Core position (b). Energy (c). Depth of the shower maximum (d).

two peaks. Due to absence of the cut on b_A the resolution of shower maximum is not present, because the position of the shower maximum for most of these events was reconstructed poorly.

The differential energy spectrum shows in the second case (12,400 showers) a threshold energy of 100 TeV (Fig. 5.21), which is defined at a level of 1/2 of the spectrum maximum. Under the assumption, that the integral spectrum has a slope of –1.7, the first case (3,100 showers) should correspond to an energy of $E = 100 \cdot (12400/3100)^{1/1.7} = 220\,\mathrm{TeV}$.

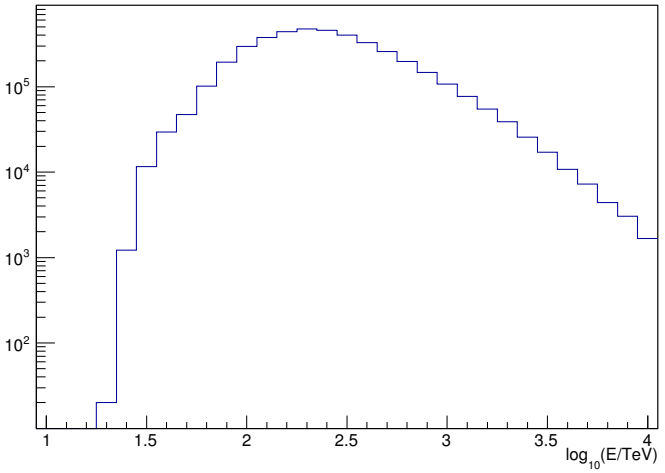

FIGURE 5.21: The reconstructed with HiSCORE-9 differential spectrum.

All these calculations can be translated directly to gamma quanta. According to their effective areas (see Sect.6.4), the equivalent energy for them is two times lower than for protons. Thus, we can expect, that the gamma quanta will be reconstructed with the same accuracies at the corresponding energies 50 TeV and 110 TeV, if they are reconstructed roughly with the same power.

On the one hand, the electromagnetic shower initiated by a gamma is expected to have less fluctuations than hadronic shower and, thus, the shower parameters can be determined better. On the other hand, the shower maximum in case of gamma rays is located further away from the ground and the central part of the lateral distribution function will be flatter. It leads to a worse reconstruction. This two opposite effects may balance each other and give roughly the same reconstruction power in case of gamma rays.

Chapter 6

Monte Carlo studies for HiSCORE-9

6.1 Monte Carlo data set

Gamma and hadron showers to study the HiSCORE-9 array were generated by the program CORSIKA 7.37 [96]. CORSIKA is a detailed Monte Carlo program to simulate the development of extensive air showers in the atmosphere initiated by various primaries such as gammas and hadrons.

Hadronic interactions were treated with the high-energy model QGSJET01c and with the low-energy model GHEISHA. Showers initiated by four nuclei (proton, helium, nitrogen, iron) and gamma in the energy range from 1 TeV to 1000 TeV with a total statistics of ~ 1 million events were generated. The energy range was divided into 31 bins on a logarithmic scale. Each bin within a decade of energy had equal statistics. The IACT add-on was used to output the Cherenkov photons data. In this approach, detectors are assumed to be spheres with certain radii. Cherenkov photons are bounded into bunches. Bunches crossing simulated spheres are stored to a binary *iact*-file. An example of a CORSIKA input-card used for the simulation can be found in Appendix C.

A 9-station Cherenkov array at the Tunka level 675 m with an inter-station spacing of 150 m was simulated, resulting in an instrumented area of 0.07 km^2. At the detector positions, Cherenkov photons were stored in spheres with a radius of 1 m. Every shower was used once and the core position was scattered inside a

700×700 m^2 area. Cherenkov light was generated within the wavelength range 200–700 nm and the photon bunch size was 10. The Earth's magnetic field at the Tunka cite has the following components: $B_x = 18.869$ μT; $B_z = 57.283$ μT (according to Geomag [97]). In addition, the default CORSIKA atmospheric light transmission was taken into account.

Two data sets, for two detector modes, in the vertical mode and with the tilting by 30 degrees, have been performed. For detectors without tilting, gamma rays come from the zenith $\theta = 0°$, and hadron showers were simulated within the cone acceptance range $\theta \in [0°, 30°]$ and with the random azimuth angle $\phi \in [0°, 360°]$. For detectors with tilting, gamma rays come also from a fixed position in the sky ($\theta \equiv \theta_t = 30°$, $\phi \equiv \phi_t$), whereas cosmic rays were simulated with $\theta \in [\theta_t - 30°, \theta_t + 30°]$ and with a fixed ϕ_t.

Most important CORSIKA parameters used to perform the Monte Carlo data set are summarized in the following table:

CORSIKA version	7.37
Basic options:	
Hadronic interaction model	QGSJETII-04/GHEISHA
Primaries	gamma, proton, helium, nitrogen, iron
Energy range	from 0 to 3 $\log_{10}$ TeV with step 0.1
Statistics	10,000 showers/bin/primary (1..100 TeV)
	1,000 showers/bin/primary (100..1000 TeV)
Array options:	
Observation level	675 m
Magnetic field	B_x=18.869 μT, B_z=57.283 μT
Atmosphere	3 (central Europe, winter)
Cherenkov options:	
Output	IACT output, detector with $R = 1$ m
Core scattering	once inside 700×700 m^2 area
Wavelength range	200..700 nm
Bunch size	10
Light reducing	atmospheric transmission

6.2 Detector simulation

Each iact-file given by CORSIKA contains shower information and Cherenkov photon bunches that hit the detectors at the ground level. All iact-files were processed by a program of detector simulation that is based on the standard HiSCORE simulation program *sim_score* [98]. The full detector simulation was implemented on the basis of the *sim_skeleton* program from the IACT package [88]. The program *sim_score* computes the signals seen by each station, taking into account the cone acceptance, the PMT quantum efficiency, PMT afterpulses, the signal shaping by the response of the acquisition system, and the noise in the system, which is dominated by light from night sky brightness [59].

A new program brunch *sim_9station* following this philosophy was developed to obtain effective areas and produce particle rates in a fast way for various trigger conditions. Besides that, the program allows to simulate the detector tilting. A distinctive feature of the modification, that the program does not use a predefined detector threshold, but it scans each pulse for a maximal allowed threshold and stores it in an ascii output file. What is more, the output files were complemented with energy, core position, and directional angles of shower as well as individual pulse parameters: integral, maximal amplitude, and pulse delay.

The following predefined simulation parameters were used:

- ▷ acrylic glass transmission $A(\lambda)$ (Sect. 5.4.1);
- ▷ Winston cone acceptance, PMT is in the middle position (Sect. 5.3.2);
- ▷ quantum efficiency of ET 9352KB, $CE = 0.8$ (Sect. 5.4.1);
- ▷ detector response (Sect. 5.5);
- ▷ trigger time duration 10 ns.

A photon bunch from CORSIKA is given by the following parameters: direction (three directional cosines c_x, c_y, c_z), coordinates at the ground level (x, y), height of production (h), wavelength (λ) and time since first interaction (t_0). Cherenkov photons that passed a station are gathered into a pulse in several steps.

6.2.1 Detector in standard mode

Photons enter inside one of the four cones when they hit the station. First, they are attenuated by the acrylic glass plate, which is the station input window, and reach the PMT after some reflections inside the cone with a probability defined by the angular acceptance $\varepsilon(\theta)$. Second, photons are converted into photoelectrons with the tabulated quantum efficiency of the photomultiplier and collected at the first dynode given by the collection efficiency CE. Third, each pulse is convoluted with the detector response, four pulses are summed up and the detector pulse is formed. Finally, trigger conditions are applied. A maximum accepted threshold for every pulse is output to ascii-files. This approach allows to built affective areas and, thus, particle rates for any desired threshold.

6.2.2 Detector in tilting mode

In case of tilting, most steps are the same except the ray-tracing of the photons where the tilting should be taken into account.

First, the projected distance between cones becomes smaller ($2R_c \cos\theta_t$) and the circle transforms into an ellipse with the semi-axes:

$$\begin{aligned} a &= R_c \\ b &= R_c \cos\theta_t \end{aligned} \tag{6.1}$$

Second, the cone normal is a vector

$$\overrightarrow{n}_{cone} = \{\sin\theta_t \sin\phi_t; \sin\theta_t \cos\phi_t; \cos\theta_t\}.$$

In the simplest case ($\phi_t = 0$) the vector $\overrightarrow{n}_{cone}$ will have coordinates $(0; \sin\theta_t; \cos\theta_t)$.

Third, one can obtain the angle between the cone axis and the particle direction defined with directional cosines (c_x, c_y, c_z) as:

$$\psi = \mathrm{acos}(-\overrightarrow{p}_{par} \cdot \overrightarrow{n}_{cone}). \tag{6.2}$$

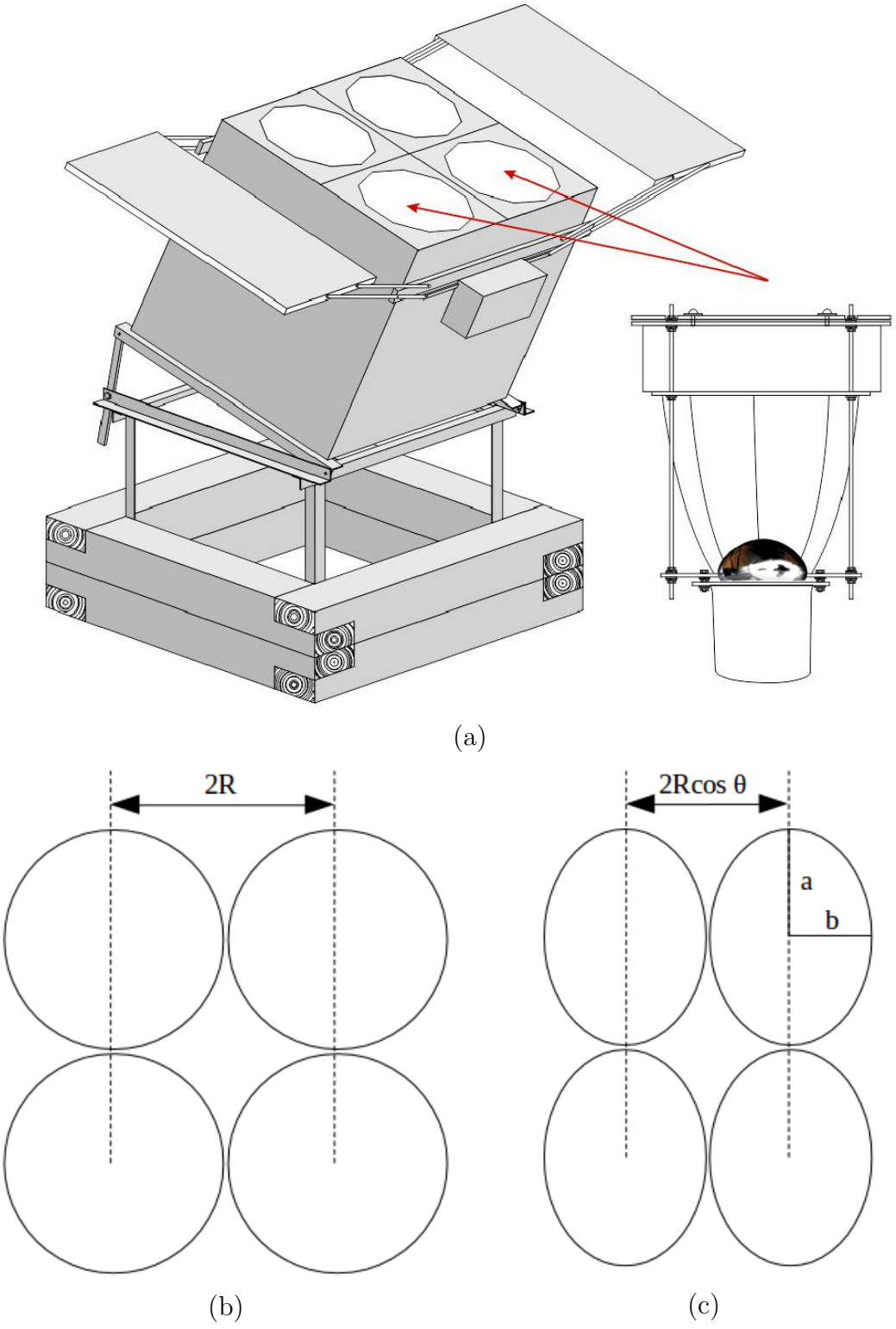

(a) (b) (c)

FIGURE 6.1: Detector in tilting mode (a). Projection of the detector face onto the horizontal plane: with (b) and without tilting (c).

Finally, the cone acceptance is obtained from the angular acceptance as $\varepsilon(\psi)$ and other steps, described in the previous subsection, remain the same.

6.3 Detector threshold

6.3.1 Discriminator threshold

The detector threshold is one of most crucial parameters of the system and has to be investigated first. A minimal detector threshold, which can be set, is related to a minimal energy threshold, which can be achieved with the instrument. As a rule, the detector threshold is limited by night sky background. Here, the threshold has been investigated in three different ways: LED calibration (Sect. 5.6.2), single station rate (Sect. 6.5), and detector multiplicity (Sect. 6.6).

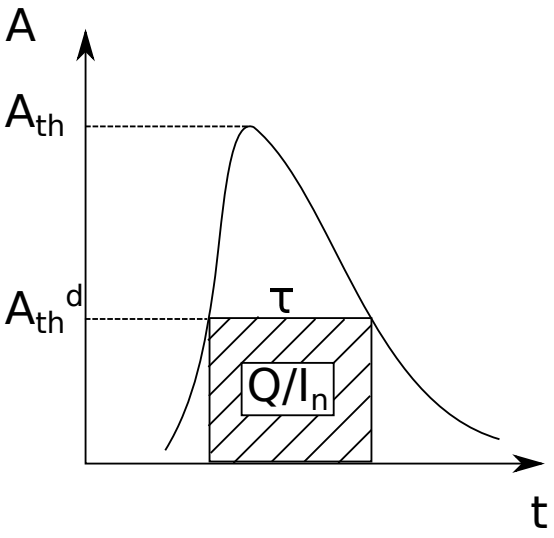

FIGURE 6.2: Various threshold definitions.

In previous HiSCORE studies [55], the threshold was supposed to be 180 p.e. This threshold corresponded to a peak value of pulse. Here the *discriminator threshold* A^d_{th} is used as a threshold definition. This definition of the threshold is more technical and reflects plausibly the logic of the real discriminator used in practice. The discriminator threshold defines as a level above which Cherenkov pulses can be registered. One additional condition is imposed here: the pulse must stay above the level during a certain time (time-over-threshold). Particularly, this duration τ is roughly 10 ns for both DAQ systems used for data taking in HiSCORE-9 (Sect. 5.2).

6.3.2 Alternative threshold definitions

There are two definitions of the detector threshold used sometimes alternatively: peak amplitude threshold and integral threshold. Amplitude threshold defines a peak amplitude of Cherenkov pulse needed to give a trigger. In case of the integral threshold the Cherenkov pulse must have a minimal pulse area, which can be registered. Amplitude level is typically expressed in terms of photons or photoelectons, whereas the integral threshold has to be expressed in terms of light density, i.e. either photons or photoelectons per meter squared. The relation between various definitions of the threshold can be found from Fig. 6.2. They strongly depend on the parameters of the chosen detector response (Sect. 5.5). Here is given an example how to recalculate discriminator threshold A^d_{th} for a value of 100 p.e. to the peak value of the pulse and its integral.

Threshold peak amplitude. According to Sect. 5.5, the peak value A_{th} is roughly two time larger that A^d_{th} ($C_\tau = 0.53$):

$$A_{th} = A^d_{th}/0.53 = 100 \text{ p.e.}/0.53 = 189 \text{ p.e.} \tag{6.3}$$

Threshold light density. The threshold light density can be defined as an integral under the A^d_{th} level during the system response time τ. There the normalisation coefficient I_n from Sect. 5.5 should be used and the light density can be expressed in photons per meter squared:

$$\begin{aligned} Q^d_{th} = & \frac{A^d_{th} \cdot \tau}{I_n \cdot CE \cdot \overline{QE}^{\text{Ch}} \cdot 4 \cdot S_c} = \\ & \frac{100 \text{ p.e.} \cdot 10 \text{ ns}}{11.74 \cdot 0.8 \cdot 0.19 \text{ p.e./ph} \cdot 4 \cdot 0.126 \cdot 10^4 \text{ cm}^2} = 0.11 \text{ ph/cm}^2. \end{aligned} \tag{6.4}$$

CE (Sect. 5.4.2) and $\overline{QE}^{\text{Ch}}$ (Sect. 5.4.1) are the collection efficiency and the average quantum efficiency of the PMT, S_c is the cone area.

Sometimes the threshold light density is preferred to be integrated using the A_{th} level [99], and thus A^d_{th} should be replaced with A_{th}:

$$Q_{th} = \frac{A_{th} \cdot \tau}{I_n \cdot CE \cdot \overline{QE}^{\mathrm{Ch}} \cdot 4 \cdot S_c} = \frac{189 \text{ p.e.} \cdot 10 \text{ ns}}{11.74 \cdot 0.8 \cdot 0.19 \text{ p.e./ph} \cdot 4 \cdot 0.126 \cdot 10^4 \text{ cm}^2} = 0.21 \text{ ph/cm}^2. \tag{6.5}$$

The last estimate 0.21 ph/cm^2 is in good agreement with the early obtained value 0.3 ph/cm^2 [99], where the effective quantum efficiency $CE \cdot \overline{QE}^{\mathrm{Ch}}$ was assumed slightly less than here.

6.4 Collection area and trigger rate

The integral rate Γ of events induced by a single type of primary particle is given by:

$$\Gamma = \int_E \frac{dN}{dE} A_{eff}(E) dE. \tag{6.6}$$

The integrand includes the spectrum dN/dE of the primary and the collection area A_{eff}. The collection area describes the efficiency of the array for detecting the primary and has units of area. A_{eff} is the area, in which the core position of a shower initiated by a particular primary with some energy has to be located in order to trigger the array. The collection area is derived from Monte Carlo simulations for different primaries, that are fully propagated through the detector simulation, met trigger conditions and applied cuts. The effective area can be calculated for each bin with energy E from Monte Carlo data sample simply as:

$$A_{eff} = \frac{N_{tr}}{N_{tot}} A_{sim}, \tag{6.7}$$

where A_{sim} is the simulated area, N_{tr} is the number of triggered events, and N_{tot} is the total number of simulated events. In particular, the effective area will depend on the energy, the detector mode (tilting), the type of primary particle, the detector threshold and acceptance cuts.

Gamma rate. The rate of gamma rays from a point source can be calculated as:

$$R_\gamma \equiv \frac{dN}{dt} = \int_E \Phi_\gamma(E) A_\gamma(E) dE \tag{6.8}$$

where $A_\gamma(E)$ is the effective area for gamma rays and $\Phi_\gamma(E)$ is the flux of the gamma ray source.

Hadronic rate. Hadronic rate is calculated in a similar way except that hadrons come within a field of view Ω of the detector:

$$R_h = \int_E \Omega(E) \sum_h \Phi_h(E) A_h(E) dE, \tag{6.9}$$

where, in that case, $A_h(E)$ is the effective area for hadron of type h, and $\Phi_h(E)$ is its flux parametrized by the polygonato model [71] (see Appendix A).

Affective area can be calculated for various trigger conditions of the HiSCORE-9 array. When it is required to have a trigger from one of the stations for a certain detector threshold, it results in the single station rate (Sect. 6.5). In contrast, when the affective areas are computed for a minimal required number of triggered stations N, it gives an opportunity to investigate the detector multiplicity (Sect. 6.6). Finally, when it is assumed, that the events will be processed further for a reconstruction, acceptance cuts are applied.

Computed collection areas of the 9-station array as a function of primary energy for various primaries and two detector modes is shown in Fig. 6.3. The collection areas have been obtained under the standard assumptions: A^d_{th}=100 p.e., at least four triggered stations, and the acceptance cut (shower cores inside the array, zenith angle $\theta < 30^\circ$). Such a minimal number of triggered stations is required to start the event reconstruction in the zero-approximation mode: planar wave front and centre of gravity. In most cases, a five-station trigger is required to do the full reconstruction involving the curved wave front and the lateral distribution function. However, even with four stations it is possible to proceed to the analysis of the shower data. The discriminator threshold A^d_{th}=100 p.e. corresponds to a conventional threshold value of 180 p.e [55]. The array energy threshold is defined as the energy at which the trigger efficiency reaches 50%. Under these standard conditions, Monte Carlo shows that the energy threshold of the array is about 30 TeV. This result mostly repeats the first estimate [55].

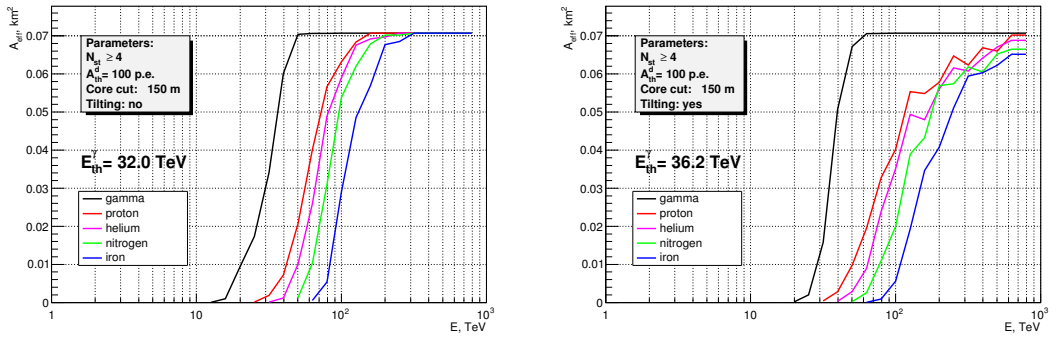

FIGURE 6.3: Effective areas of the simulated 9-station array for gamma rays and four nuclear mass groups versus MC energy under the standard assumptions. Two detector modes are present: without tilting (*left*) and with tilting (*right*).

6.5 Single station rate

A minimal detector threshold can be derived from simulations of the single station rate and the night sky background. Amplitude where the night sky curve intersects the cosmic ray rate curve will determine the desired detector threshold (Fig. 6.4). In the same way, the detector threshold is determined experimentally.

For a wide-angle (∼1 sr) Cherenkov detector the night sky flux is expected to be $\Phi_{\rm NSB} = 3.2 \cdot 10^{12}\,{\rm ph/m^2\,s\,sr}$ (Sect. 3.3). In this case, the NSB rate in each of four channels can be estimated as:

$$R_{\rm NSB} = \Phi_{\rm NSB} \cdot A_{det} \cdot \Omega \cdot CE \cdot \overline{QE}_{\rm NSB}, \tag{6.10}$$

where A_{det} is the cone area, Ω is the detector solid angle (Sect. 5.3.2), CE is the collection efficiency (Sect. 5.4.2), and $\overline{QE}_{\rm NSB}$ is the average quantum efficiency (Sect. 5.4.1).

This results in:

$$R_{\rm NSB} = 3200\ {\rm ph/m^2\ ns\ sr}\ \cdot\ 0.126\ {\rm m^2}\ \cdot\ 0.58\ {\rm sr}\ \cdot\ 0.8\ \cdot\ 0.08\ {\rm p.e./ph} = 15\ {\rm p.e./ns}. \tag{6.11}$$

In the same way, when the detector operates in the tilting mode, the flux should drop to a value of $\Phi_{\rm NSB}^{30^\circ} = 2.7 \cdot 10^{12}\,{\rm ph/m^2\,s\,sr}$, and, thus, the NSB rate will be $R_{\rm NSB}^{30^\circ} = 13$ p.e./ns.

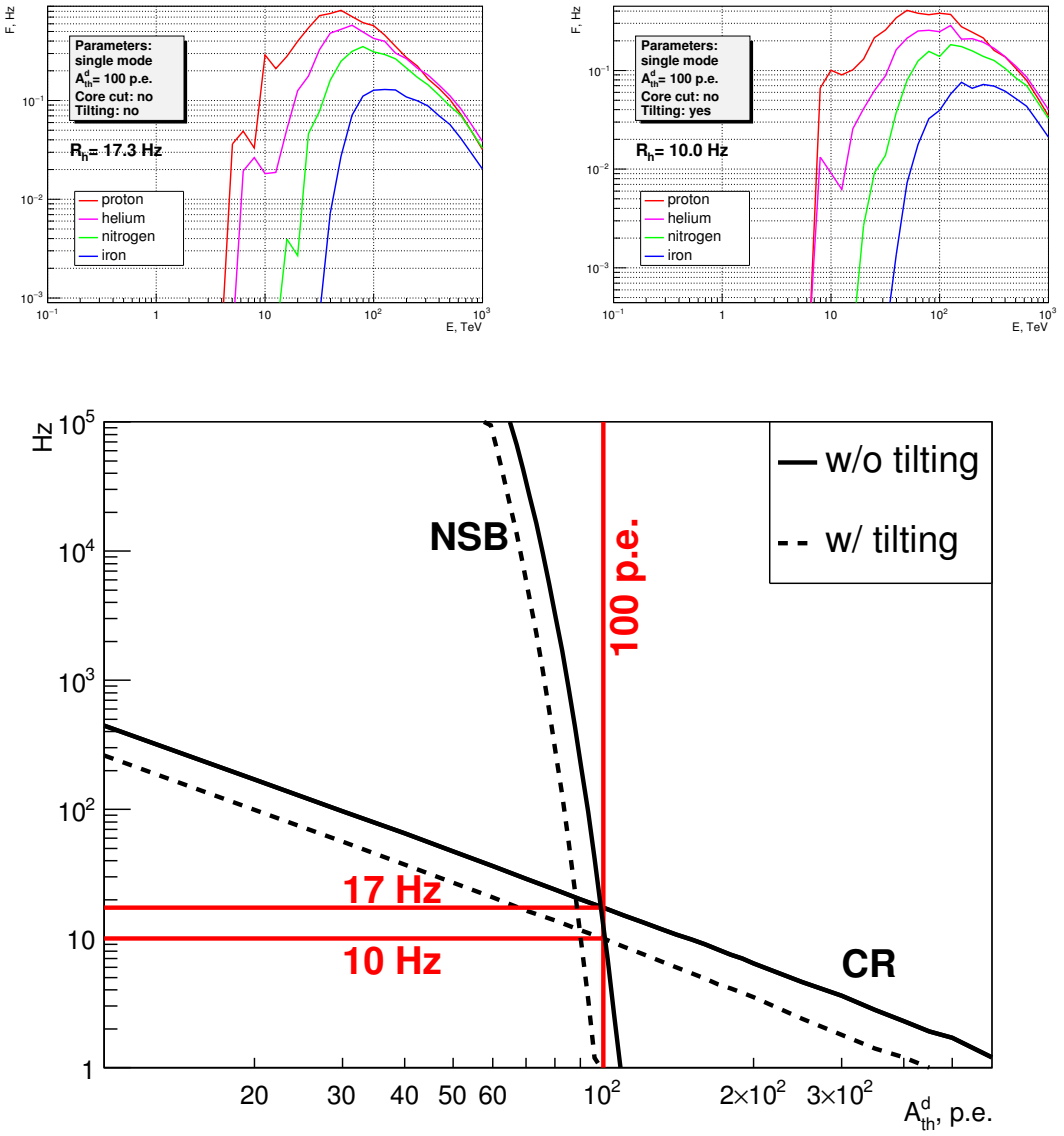

FIGURE 6.4: Single station rates as it predicted by Monte Carlo.

Single photo-electron pulses in a channel were simulated in the time bins of 1 ns according to Poisson statistics. Each channel was simulated separately, and then all four channels were summed up and discriminated.

In each time bin with bin center t_0 for R_{NSB} photo-electrons per ns:

- ▷ a pulse amplitude A_0 was chosen randomly according to the amplitude distribution (Sect. 5.4.3),
- ▷ the amplitude at the specific time for each pulse is computed according to $A(t0 + t) = A_0 f(t)$, where $f(t)$ is the normalised pulse shape (Sect. 5.5),

▷ the pulse amplitudes are added to the trace.

The results on modelling the single station rate are shown in Fig. 6.4. The night sky curve intersects both cosmic ray curves at a threshold of 100 p.e. The corresponding rates are 17 Hz (without tilting) and 10 Hz (with tilting). CR rates can be well approximated by a single power-law:

$$\begin{aligned} R(A^d_{th}) &= 17.3 \cdot 10^{-1.44 \cdot \log_{10}(A^d_{th}/100 \text{ p.e.})} \text{ Hz} \\ R(A^d_{th})^{tilt} &= 10.0 \cdot 10^{-1.54 \cdot \log_{10}(A^d_{th}/100 \text{ p.e.})} \text{ Hz.} \end{aligned} \tag{6.12}$$

These results are in a good agreement with the previous study, where a single rate of 12.8 Hz was predicted [10], and with the experiment. Currently observing rates are 12–15 Hz without the detector tilting and 6–8 Hz with the detector tilting [99].

6.6 Detector multiplicity

Alternatively, the detector multiplicity allows to investigate array performance and compare its with real data. Fig. 6.5 shows such results. Here, a date of the first season under the best weather conditions is used for comparison. As seen from the figure, for a station threshold of 100 p.e. the real data and the Monte Carlo are not well in agreement. Most probably, the effective threshold of the array as a composition of multiple detectors is slightly higher. A good agreement is observed at a threshold of 180 p.e. The explanation for that might be, that during the first season, the 9-station array was not completely equipped, so that one or two stations had less than four PMTs (station 3 and station 9 for example). Furthermore, one can have additional light losses unaccounted for in the detector simulation. These factors may lead to a different slope of the detector multiplicity curve and different absolute values of the multiplicities.

6.7 Crab Nebula sensitivity

The Crab Nebula is a "standard candle" and it will be tried to be detected as a first gamma ray source by HiSCORE. The array sensitivity to the Crab Nebula is studied in this section.

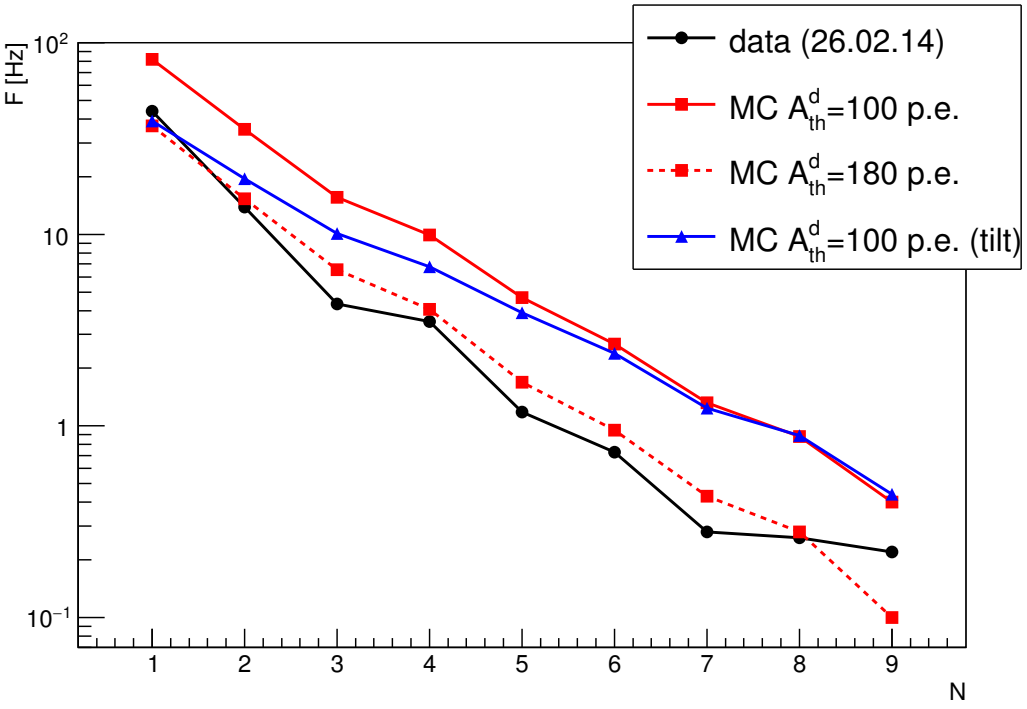

FIGURE 6.5: Detector multiplicity of the 9-station array as a function of the number of triggered stations. The data from 26.02.14 are shown for comparison.

A gamma ray source is classified as a detected one if the signal in the source region exceeds the homogeneous background level from cosmic rays. The excess above at least five standard deviations and a minimal number of positive gamma ray events are usually required.

The significance of the source detection can be approximated following Li & Ma [100] (Eq. 5) by

$$S = \frac{N_{on} - N_{off}}{\sqrt{N_{on} + \alpha^2 N_{off}}}, \tag{6.13}$$

where N_{on} is the number of the events in the source region and N_{off} is the number of events in the background region of equal area. Suppose that the background is estimated fairly well ($\alpha = 0$) and the source is faint ($N_\gamma \ll N_h$). In that case, if the number of events in the source region is given by a sum of background events N_h and signal events N_γ, one can set that $N_{on} = N_\gamma + N_h \approx N_h$ and $N_{off} = N_h$.Then Eq. 6.13 results in:

$$S = \frac{N_\gamma}{\sqrt{N_h}}. \tag{6.14}$$

This equation can be additionally written in terms of rates to determine the time that is required to observe the source at some significance level:

$$S = \frac{R_\gamma}{\sqrt{R_h}}\sqrt{T} \tag{6.15}$$

or

$$T = \frac{R_h}{R_\gamma^2}S^2. \tag{6.16}$$

The hadronic rate R_h and the gamma rate R_γ are calculated in the way that was introduced in Sect. 6.4.

As seen, the observation time decreases with the instrument area as $\sim A^{-1}$ since $R \sim A$ and with the required detection significance as $\sim S^2$. The observational time is reduced by applying an algorithm of the gamma-hadron separation. This background rejection characterises by the *quality factor* Q given by:

$$Q = \frac{\varepsilon_\gamma}{\sqrt{\varepsilon_h}}, \tag{6.17}$$

where ε_γ and ε_h are the probabilities for gamma ray events and background events to survive the quality cut. The quality factor has a linear impact on the instrument sensitivity and if $N_\gamma \ll N_h$ the observation time will decrease as $\sim Q^2$. We expect that the planned hybrid array within a framework of the TAIGA experiment combined with imaging telescopes will provide a quality factor of 2 [101]. Apart from that, the quality of the pure HiSCORE reconstruction will achieve a Q-factor of 1 at the threshold and approaches 2 at several hundreds of TeV [98].

The Crab Nebula flux approximation up to 20 TeV is given by the most comprehensive spectrum to date measured by the MAGIC experiment [102] (Fig. 6.6). Following this approach, the spectrum of the Crab Nebula is approximated by a logarithmic parabola:

$$\Phi_\gamma(E) = 3.23 \cdot 10^{-11}\,(E/\mathrm{TeV})^{-2.47-0.24\log_{10}(E/\mathrm{TeV})}\,(\mathrm{TeV}^{-1}\mathrm{cm}^{-2}\mathrm{s}^{-1}). \tag{6.18}$$

The background hadronic rate is always limited by the angular resolution of the instrument $\delta\theta$. Investigation of the single station rate shown a minimal adjustable detector threshold of A_{th}^d=100 p.e. (Sect. 6.5), which corresponds to a peak value of 190 p.e. (Sect. 6.3.2). The obtained detector threshold 190 p.e. and the energy

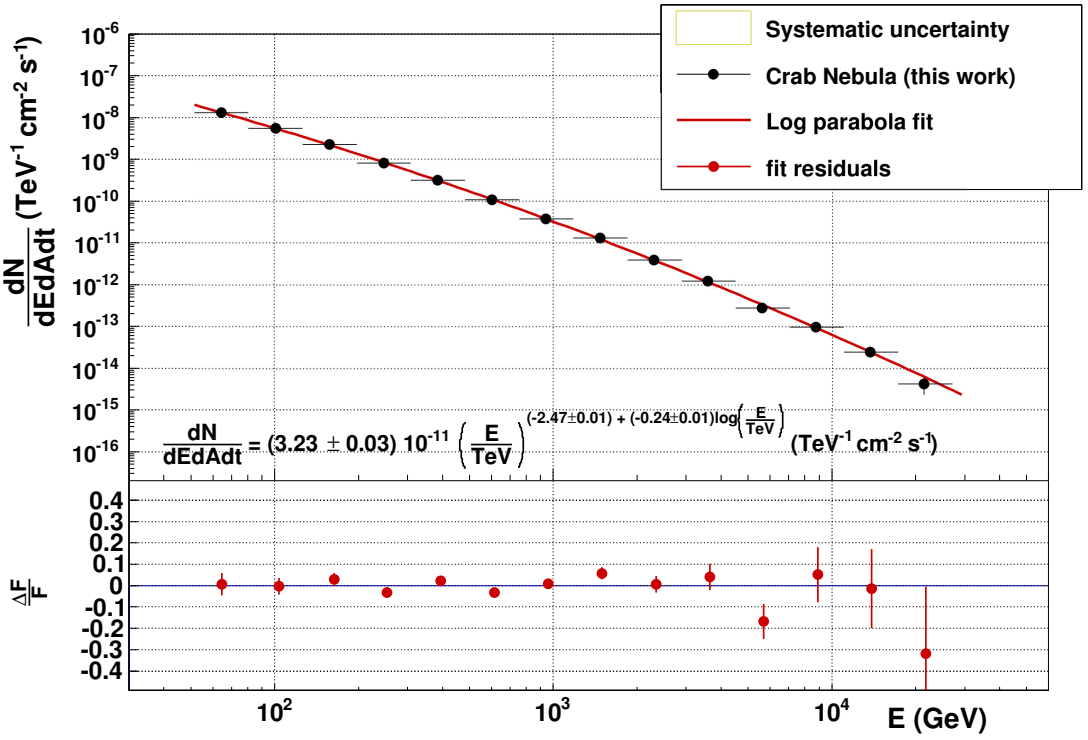

FIGURE 6.6: Differential energy spectrum of the Crab Nebula obtained by the MAGIC Collaboration [102].

threshold 30 TeV (Fig. 6.3) under the standard conditions are similar to the first studies on the performance of the HiSCORE instrument [98]. Thus, the predicted earlier angular resolution $\delta\theta$ should also be valid here (Fig. 6.7).

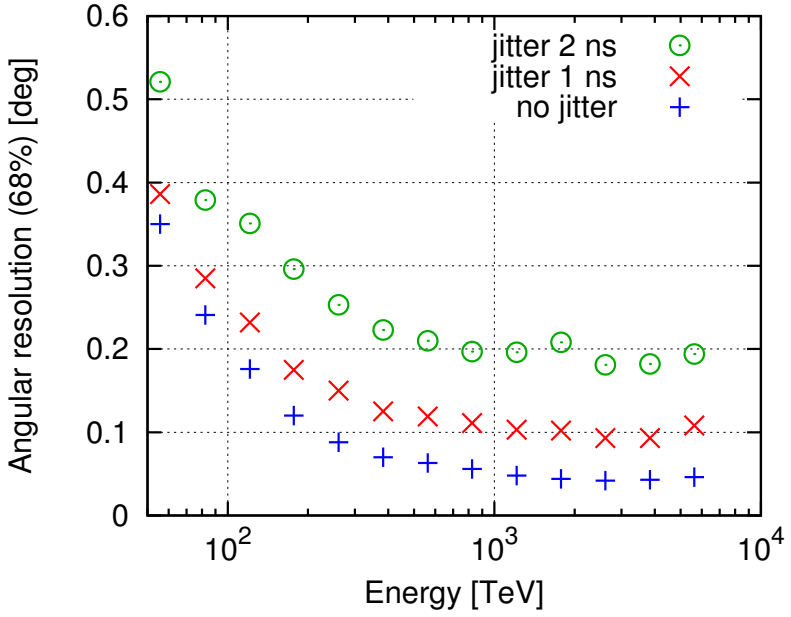

FIGURE 6.7: Angular resolution of the HiSCORE instrument [98].

The angular resolution for jitter 0 was used since a close system resolution of 200 ps was obtained after the LED calibration (Sect. 4.2). The angular resolution (σ_{68}) approaches from 0.35° at 60 TeV to 0.05° above 1 PeV. Under any different conditions, the angular acceptance can be simply biased according to the energy threshold for gamma rays.

The solid angle ω corresponding to the angular resolution $\delta\theta$ is calculated simply as for a cone with the opening angle $\delta\theta/2$:

$$\omega = 2\pi \left(1 - \cos\frac{\delta\theta}{2}\right). \tag{6.19}$$

Since 1-σ range (percentile 68%) of the one-dimensional normal distribution is used to characterize the angular resolution, the expected R_γ from the source has to be multiplied by a factor of 0.39, that corresponds to a 1-σ range for the bidimensional normal distribution [103].

Results on the Crab Nebula sensitivity are summarized in Table 6.1. Here is assuming, that the source will be observed 200 hours per year [99]. Therefore, to observe the Crab Nebula after one year at a level of 5-σ the array with an area of 4 km^2 is needed. In case of a combination of the data analysis with the background rejection technique, say with a quality factor of $Q = 2$, the area that is required reduces to a scale of 1 km^2.

TABLE 6.1: Detection sensitivity of the Crab Nebula for different array configurations. Stations are in the tilting mode (30°), detector spacing is 150 m, A^d_{th}=100 p.e., $N_{st} \geq 4$, acceptance cut is applied (shower cores inside the array, $\theta < 30°$).

Array configuration	$T_{3\sigma}$, y	$T_{5\sigma}$, y	R_γ, y^{-1}	R_h, y^{-1}
9-station array, 0.07 km^2	22	62	4	41
1 km^2-array	1.5	4.3	57	586
1 km^2-array + $Q = 2$	0.4	1.1	57	147

Finally, the time required to observe the Crab Nebula for various parameters was generalized (Fig. 6.8):

$$T_s^{tilt} = 46 \left(\frac{A_{eff}}{0.07\ \mathrm{km}^2}\right)^{-1} \left(\frac{S}{5}\right)^2 Q^{-2} \left(\frac{E^\gamma_{th}}{30\ \mathrm{TeV}}\right)^{1.5+0.5\log_{10}\left(\frac{E^\gamma_{th}}{30\ \mathrm{TeV}}\right)} \ [\mathrm{y}], \tag{6.20}$$

where

$$E_{th}^{\gamma} = 32 \cdot \left(\frac{N}{4}\right)^{2.17} \frac{A_{th}^{d}}{100 \text{ p.e.}} \text{ [TeV]}. \tag{6.21}$$

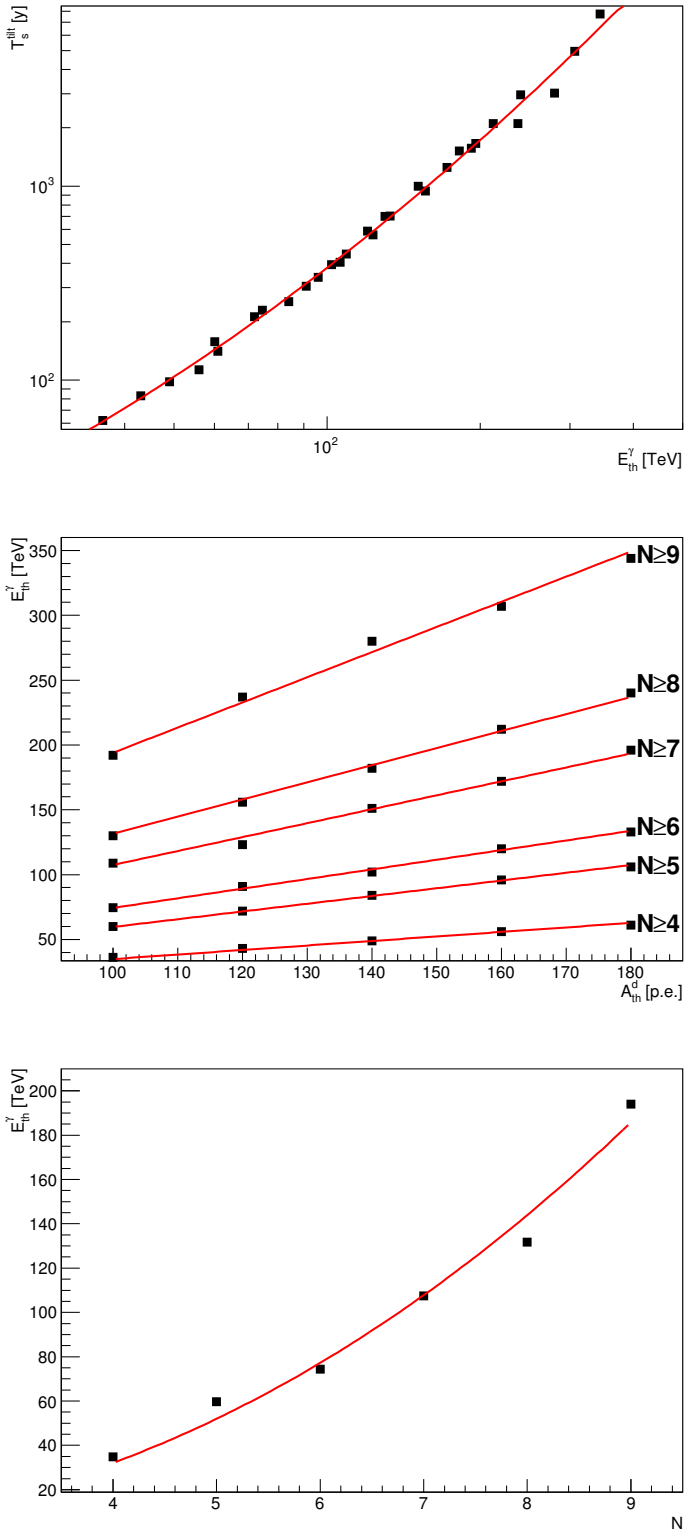

FIGURE 6.8: Parametrization of functions (from top to bottom): $T_s^{tilt}(E_{th}^{\gamma})$, $E_{th}^{\gamma}(A_{th}^{d})$ and $E_{th}^{\gamma}(N)$.

Chapter 7

The CHERRY program

A simulation of extensive air showers is an important task to interpret the data from ground-based arrays and reconstruct shower parameters. During the past two decades the Monte Carlo package CORSIKA became a world standard tool for simulating air showers induced by cosmic rays in the atmosphere. CORSIKA provides a detailed simulation of interaction, propagation, and decay of particles inside the shower initiated by high-energy primaries. The program allows to reproduce not only the mean values of the measurable shower observables but also their fluctuations and correlations with the primary shower parameters. Unfortunately complete shower simulation takes much time and requires much storage space. Processing time and the size of output files grow exponentially with energy of primary particle. The situation is worse with the production of Cherenkov light, that needs even more time than pure simulation of charged particles. As illustrated by Fig. 7.1, the simulation of the single shower with optionally enabled Cherenkov light generation takes typically one-two days for an energy of 10^{16} eV, two weeks for an energy of 10^{17} eV, and more than two months for an energy of 10^{18} eV. Moreover, the size of the iact-file used for the Cherenkov output becomes larger than 1 Gb above an energy of 10^{16} eV. Thus, complete air-shower simulations of cosmic rays at these energies become a very difficult task and must be somehow optimized.

One of the methods to reduce the time consumption is the so-called *thinning* algorithm [104]. The statistical thinning reduces the number of secondary particles tracked replacing particles, that have energies below an adjustable fraction of the primary energy, with a single particle which is assigned a weight. Unfortunately

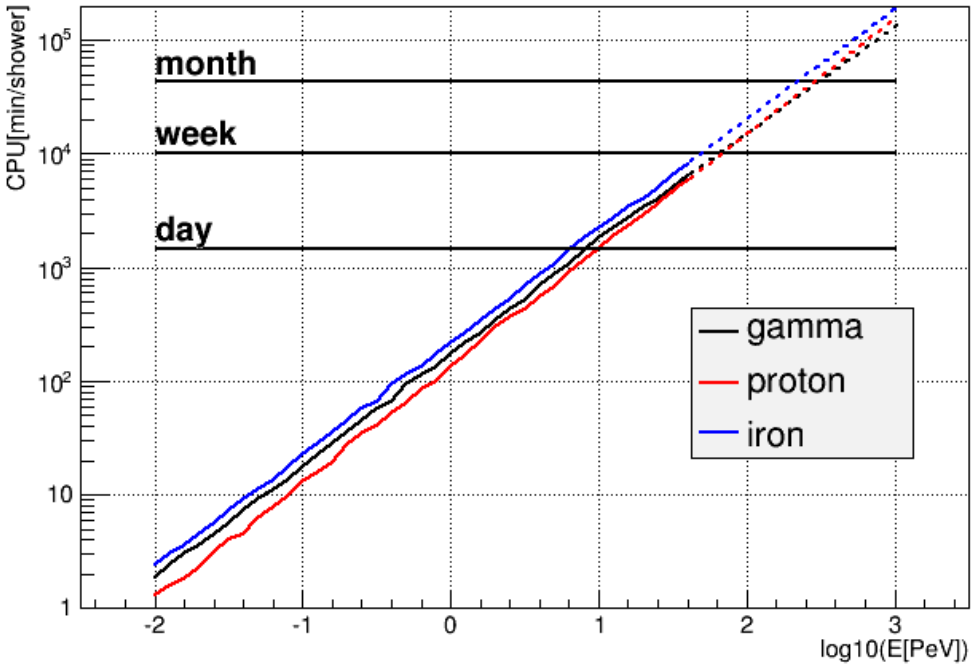

FIGURE 7.1: CPU time required to generate a single shower in CORSIKA with enabled Cherenkov light production.

this algorithm introduces additional artificial fluctuations and systematic biases to observable shower quantities, which are very difficult to avoid afterwards. Most likely, that neither the un-thinning algorithm [105] nor the de-thinning [106] will solve this problem in case of Cherenkov light because the light pulse in the detector must be reproduced very accurate. Experience shows, that for Cherenkov light production this drawback is crucial and, thus, the thinning method would not be recommended.

Another way in some sense is the parallelization of the code CORSIKA to treat independent sub-showers by different CPU cores in parallel [107]. Unfortunately, such an optimization aimed at Cherenkov light is not implemented yet in CORSIKA.

In order to simulate Cherenkov light in a reasonable time, a new fast code named **CHERRY** (**CH**erenkov a**RR**a**Y** simulator) has been developed. CHERRY is the program designed to simulate Cherenkov light distribution at the ground level from air showers initiated by gamma rays or nuclei with energies above 10 TeV. CHERRY allows to reproduce accurately Cherenkov pulses in optical non-imaging detectors inside an arbitrary array configuration. The program simulates the pulse

including a realistic detector response as well as the quantum efficiency of the photomultiplier and other characteristics. The noise caused by night sky background is added to the trace of the pulse and simplistic trigger conditions can be applied.

CHERRY is a very fast program. It takes roughly 10 seconds for a single shower irrespective of energy. CHERRY neither treat nuclear interactions nor track Cherenkov photons. The Cherenkov pulses at a distance R from the shower core were parametrized by a common empirical shape, which parameters were associated with one single shower parameter – *distance to the shower maximum* ΔX_{max}. Cherenkov pulses are approximated by means of the exponentially modified Gaussian (EMG). With this function pulses can be successfully parametrized for a wide range of distances from shower core and for any type of primary.

7.1 Program structure

CHERRY has a small main program `cherry.cpp` written in C++. It reads an input-card and creates an output *root*-file with pulse traces and shower parameters (Fig. 7.2). It can be launched with the following command:

```
./cherry INPUT OUTPUT
```

Two configurational blocks are initialized at first: array configuration and optical detector configuration. These dat-files are located in the folder `dat/`. The array configuration consists of a file `det_list.dat` with three columns of detector coordinates and one column with the radius of each detector. The number of detectors is not limited and the radius of each detector can be set independently. Detector configuration consists of three files: detector angular acceptance (`ang_acc.dat`), detector response (`det_resp.dat`) and photomultiplier quantum efficiency (`qe_table.dat`). In addition, the detector configuration includes the transmission of the input window of the detector made of acrylic glass (`plex_trans.dat`).

7.1.1 Input-card

The input-card has several fields with key words that must be filled to start the simulation. Below the structure of the input card is given:

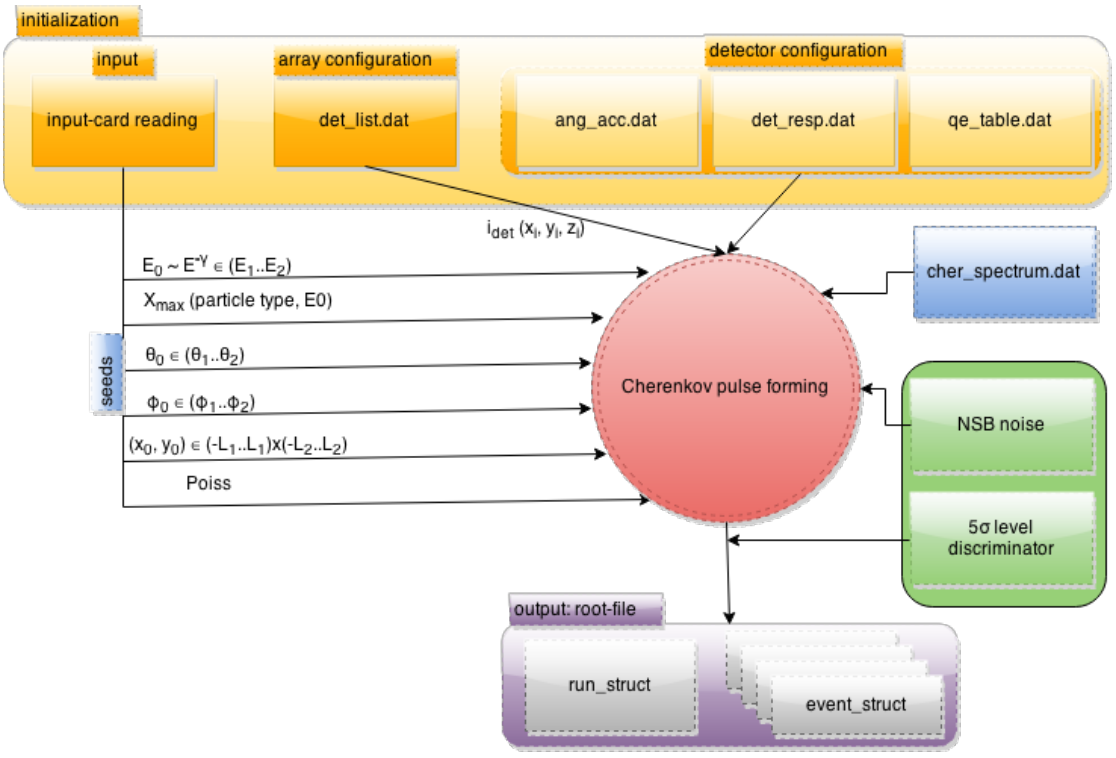

FIGURE 7.2: Schematic of the CHERRY program.

`PRMPAR` A //primary particle mass

A=0 – gamma

A=1 – proton

A=56 – iron

`ERANGE` γ E_1 E_2 //energy range ($\log_{10}$ TeV)

E_1 – lower limit

E_2 – upper limit

γ – slope

`THETAP` θ_1 θ_2 //zenith angle range (deg)

`PHIP` ϕ_1 ϕ_2 //azimuth angle range (deg)

`NSHOW` N_{sh} //number of showers

`OBSLEV` H_{lev} //observation level (m)

`CSCAT` L_1 L_2 //simulation area $L_1 \times L_2$ (m^2)

`SEED` seed$_i$ $i = 1, 6$ // random generator seeds

seed$_1$ – energy generator

$seed_2$ – shower maximum generator
$seed_3$ – zenith angle generator
$seed_4$ – azimuth angle generator
$seed_5$ – shower core generator
$seed_6$ – main program generator (signal fluctuations)

7.1.2 Output file

Output-file is a root-file containing a run header (`run_struct`) common for all events in the run and an event structure (`event_struct`) for each simulated event. The run header includes mostly parameters of the simulation from the input-card. Event block consists of event parameters such as energy, depth of shower maximum, core position, zenith and azimuth angles. For each detector that had a trigger four pulse parameters (integral, amplitude, width, and time delay) and the distance to the shower core are stored.

7.2 Monte Carlo data set

In order to parametrize the CHERRY model a CORSIKA data set was generated. Showers from 10 TeV to some tens of PeV initiated by three type of primaries (gamma, proton and iron) were simulated. The particles come with two fixed zenith angles of 0° and 45° to cover a large ΔX_{max} range. The array location corresponding to the Tunka site was chosen. All of these CORSIKA parameters are listed in the following table:

CORSIKA version	7.37
Basic options:	
Hadronic interaction model	QGSJETII-04/FLUKA
Primaries	gamma, proton, iron
Energy range	from –2 to 1.5 $\log_{10}$ PeV with step 0.1
Zenith angle range	0° (fixed), 45° (fixed)
Statistics	10 showers/bin/primary/angle

Array options:	
Observation level	675 m
Magnetic field	B_x=18.869 μT, B_z=57.283 μT
Atmosphere	3 (central Europe, winter)
Cherenkov options:	
Output	non-imaging output, 1×1 m^2 detector
Wavelength range	200..700 nm
Bunch size	10
Light reducing	atmospheric transmission

7.3 Exponentially modified Gaussian

As a universal model describing a Cherenkov pulse the exponentially modified Gaussian function (EMG) has been chosen, which is derived by convolution of the Gaussian function with a truncated exponential [108] and given by:

$$f_{\mathrm{EMG}}(t) = \frac{Q}{2\tau} \exp\left(\frac{1}{2}\left(\frac{\sigma}{\tau}\right)^2 - \frac{t-t_c}{\tau}\right)\left(1 - \mathrm{erf}\left(\frac{1}{\sqrt{2}}\left(\frac{\sigma}{\tau} - \frac{t-t_c}{\sigma}\right)\right)\right), \quad (7.1)$$

where Q is the peak area, t_c and σ are the mean and the standard deviation of Gaussian respectively, τ is the time constant of the exponential.

The function describes well Cherenkov pulses produced by a primary within a wide range of core distances from 50 m to 1 km (Fig. 7.3). The parameters Q, t_c, σ and τ of this function vary with the distance to the shower core R and will be called *lateral functions*. Every lateral function was parametrized by its own function with a single variable parameter ΔX_{max} (Fig. 7.4).

Lateral functions $t_c(R)$ and $\sigma(R)$ were parametrized here with a similar parabolic approximation used for the shower front approximation (Sect. 4.3.2). The function $\tau(R)$ can be described with the parametrization used for the fit of pulse widths earlier [89]. And finally the function $Q(R)$ is the lateral distribution function from Sect. 4.3.3.

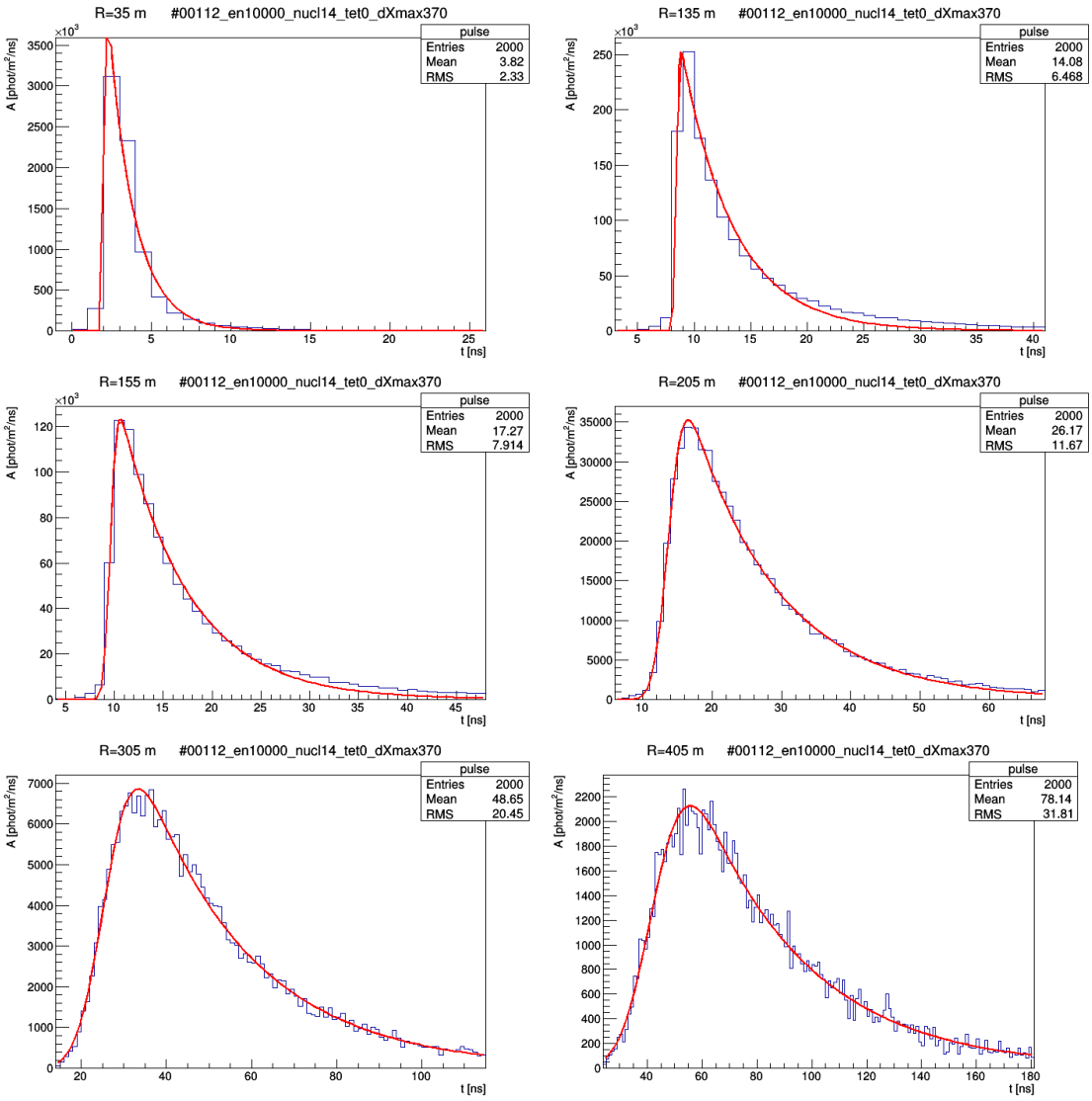

FIGURE 7.3: Parametrization of Cherenkov pulses at different distances from the shower core with the EMG function.

In the next subsection the parametrization of all these lateral functions is given. If necessary, lateral functions are optimized at short distances from the shower core.

7.4 Lateral functions

7.4.1 Function $t_c(R)$

The expression for the function $t_c(R)$ (Fig. 7.5) is given by

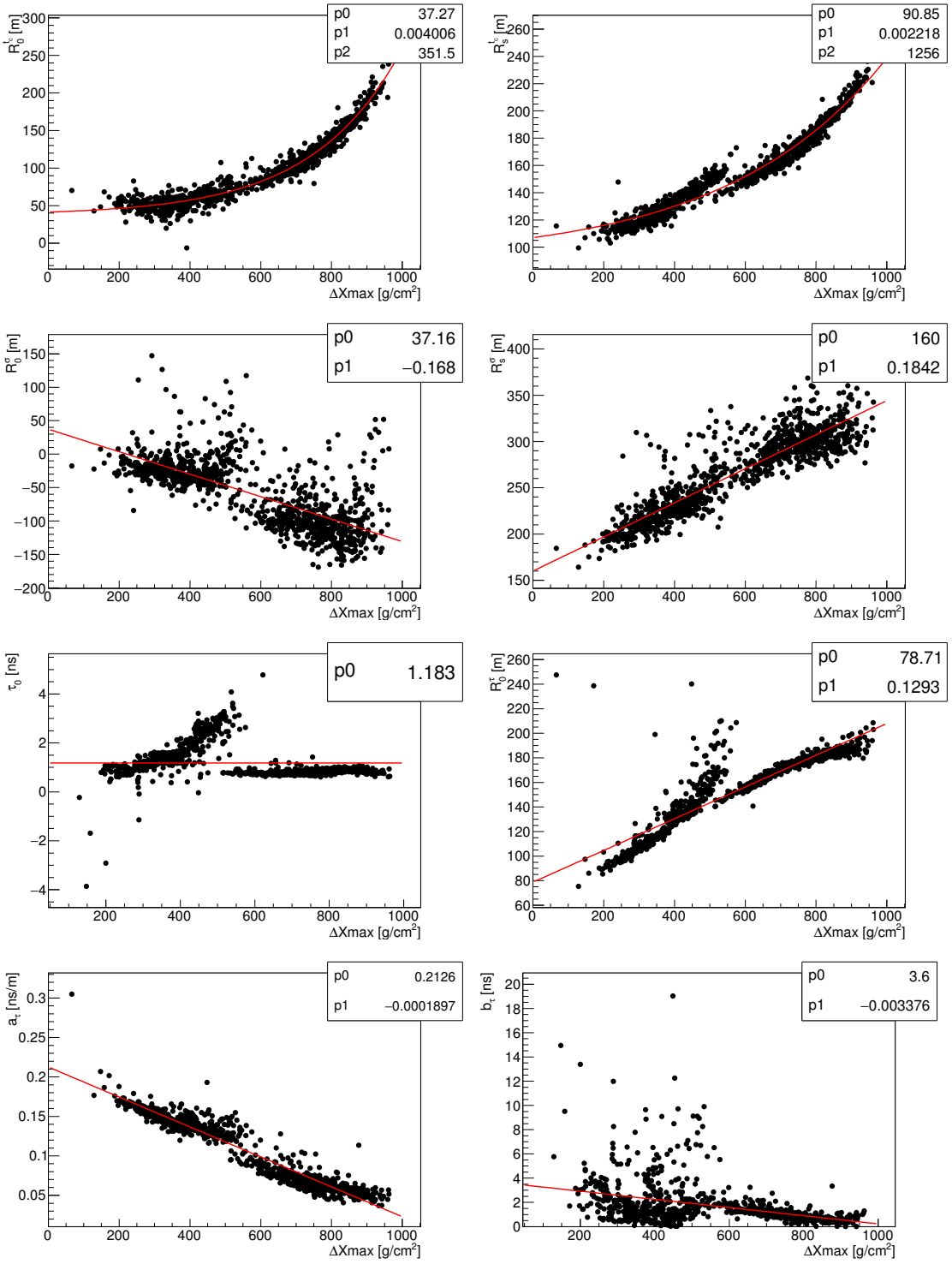

FIGURE 7.4: Correlation of lateral parameters with ΔX_{max}.

$$t_c(R) = \begin{cases} \frac{\left(R_0^{tc}+R\right)^2}{R_s^{tc}} \frac{1}{c_{air}} \text{ [ns]}, & R > 150 \text{ m} \\ \frac{\left(R_0^{tc}+150\right)^2}{R_s^{tc}} \frac{1}{c_{air}} \frac{R}{150} \text{ [ns]}, & R \leq 150 \text{ m}, \end{cases} \tag{7.2}$$

where

$$R_0^{tc} = 37.3 + (4.01 \cdot 10^{-3} + 1)^{\Delta X_{max}+352} \text{ [m]},$$

$$R_s^{tc} = (90.9 + (2.22 \cdot 10^{-3} + 1)^{\Delta X_{max}+1256})^2 \text{ [m]}.$$

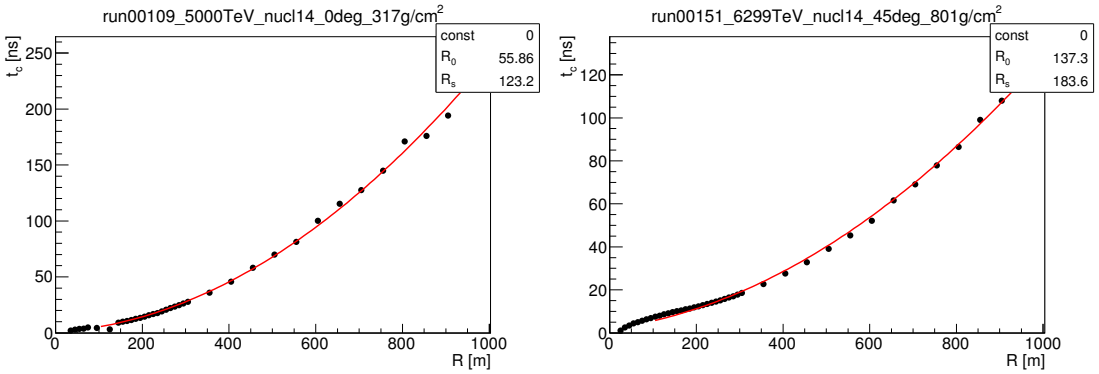

FIGURE 7.5: Lateral function $t_c(R)$: 0° (*left*), 45° (*right*).

7.4.2 Function $\sigma(R)$

Similar to $t_c(R)$, the expression for the function $\sigma(R)$ (Fig. 7.6) is given by

$$\sigma(R) = \sigma_0 + \frac{(R_0^{\sigma} + R)^2}{R_s^{\sigma}} \frac{1}{c_{air}} \text{ [ns]}, \tag{7.3}$$

where

$$\sigma_0 = \begin{cases} 0 \text{ [ns]}, & \theta = 0°, \\ 0.8 \text{ [ns]}, & \theta = 45°, \end{cases}$$

$$R_0^{\sigma} = 37.2 - 0.168 \cdot \Delta X_{max} \text{ [m]},$$

$$R_s^{\sigma} = (160. + 0.184 \cdot 10^{-3} \cdot \Delta X_{max})^2 \text{ [m]}.$$

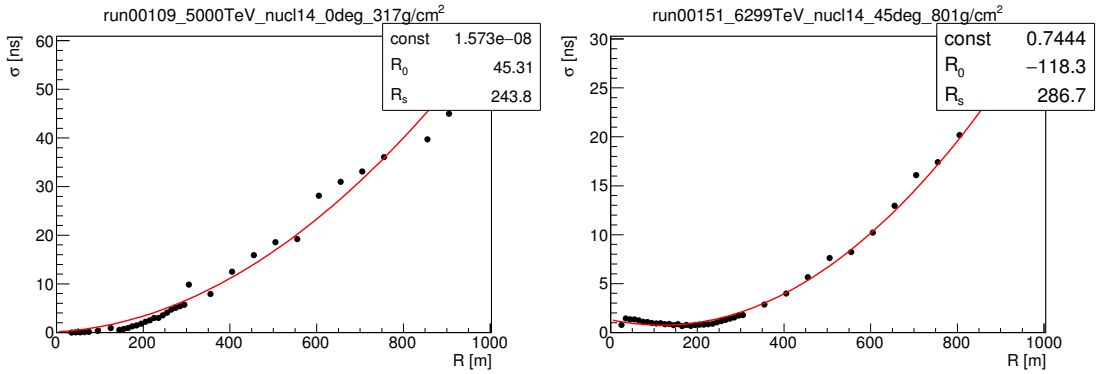

FIGURE 7.6: Lateral function σ: 0° (*left*), 45° (*right*).

7.4.3 Function $\tau(R)$

The parametrization for $\tau(R)$ (Fig. 7.7) was adopted from [89], where such a function was used to describe dependence of pulse width with distance:

$$\tau(R) = \begin{cases} \tau_0 + a_\tau \left(R - R_0^\tau\right) + b_\tau \log_{10}\left(1 + \exp\left(-\frac{a_\tau}{b_\tau}\right)\left(R - R_0^\tau\right)\right) \text{ [ns]}, & R > 100 \text{ m}, \\ 10^{\frac{\log_{10}(\tau(100)-0.2)}{100}\cdot R + 0.2} \text{ [ns]}, & R \leq 100 \text{ m}, \end{cases} \tag{7.4}$$

where

$$\tau_0 = 1.2 \text{ [ns]},$$

$$R_0^\tau = 78.7 + 0.129 \cdot \Delta X_{max} \text{ [m]},$$

$$a_\tau = 0.213 - 1.9 \cdot 10^{-4} \cdot \Delta X_{max} \text{ [ns/m]},$$

$$b_\tau = 3.6 - 3.38 \cdot 10^{-3} \cdot \Delta X_{max} \text{ [ns]}.$$

7.4.4 Function $Q(R)$

The lateral function $Q(R)$ is the well-known lateral distribution function (LDF). The LDF parametrization used in Tunka experiment is applicable to the purposes of this model too (Sect. 4.3.3). Only the correlation of the parameters has to be slightly modified (Fig. 7.8). The function with two variable parameters, density at a distance of 200 m Q_{200} and steepness b_Q, is defined as follows:

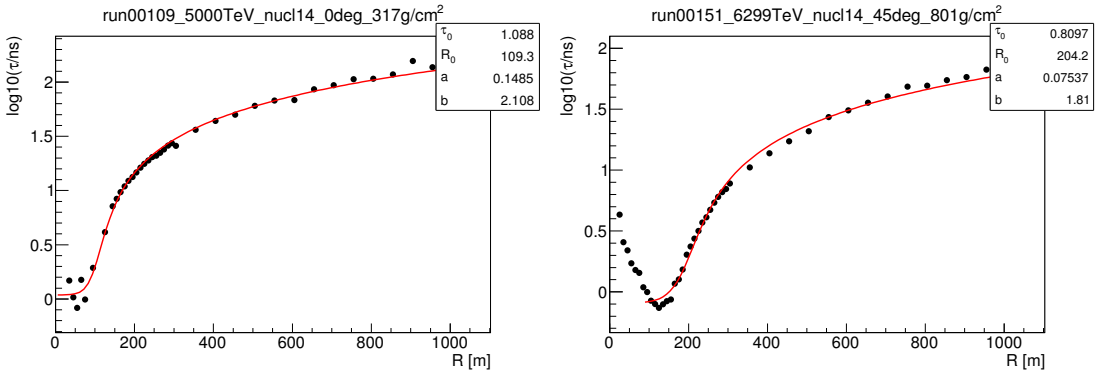

FIGURE 7.7: Lateral function $\tau(R)$: 0° (*left*), 45° (*right*).

$$Q(R) = Q_{kn} \times \begin{cases} \exp\left(\frac{R_{kn}-R}{R_0}\left(1+\frac{3}{R+3}\right)\right), & R < R_{kn}, \\ \left(\frac{R}{R_{kn}}\right)^{-a_Q}, & R_{kn} \le R < 300 \text{ m}, \\ \left(\frac{300}{R_{kn}}\right)^{-a_Q}\left((\frac{R}{300}+1)/2\right)^{-b_Q}, & R \ge 300 \text{ m}, \end{cases} \tag{7.5}$$

Four of these variables are strictly connected with the main parameters Q_{200} and b_Q:

$$Q_{kn} = Q200\left(\frac{200}{R_{kn}}\right)^{a_Q},$$

$$R_{kn} = 324 - 52.5 \cdot b_Q \text{ [m]},$$

$$R_0 = 10^{2.13-1.16\cdot\log 10(b_Q-2.6)} \text{ [m]},$$

$$a_Q = 0.99 + 0.26 \cdot b_Q.$$

Steepness b_Q. The steepness, in turn, is correlated with the depth of the shower maximum,

$$b_Q = 10^{(934-\Delta X_{max})/1470} + 2. \tag{7.6}$$

Density Q_{200}. As before, the Q_{200} parameter can be parametrized by a linear function on a double log-scale (Fig. 7.9):

$$\log_{10}(Q_{200}) = (\log_{10}(E_0) + a_q)/b_q, \tag{7.7}$$

The fit parameters are given in Table 7.2.

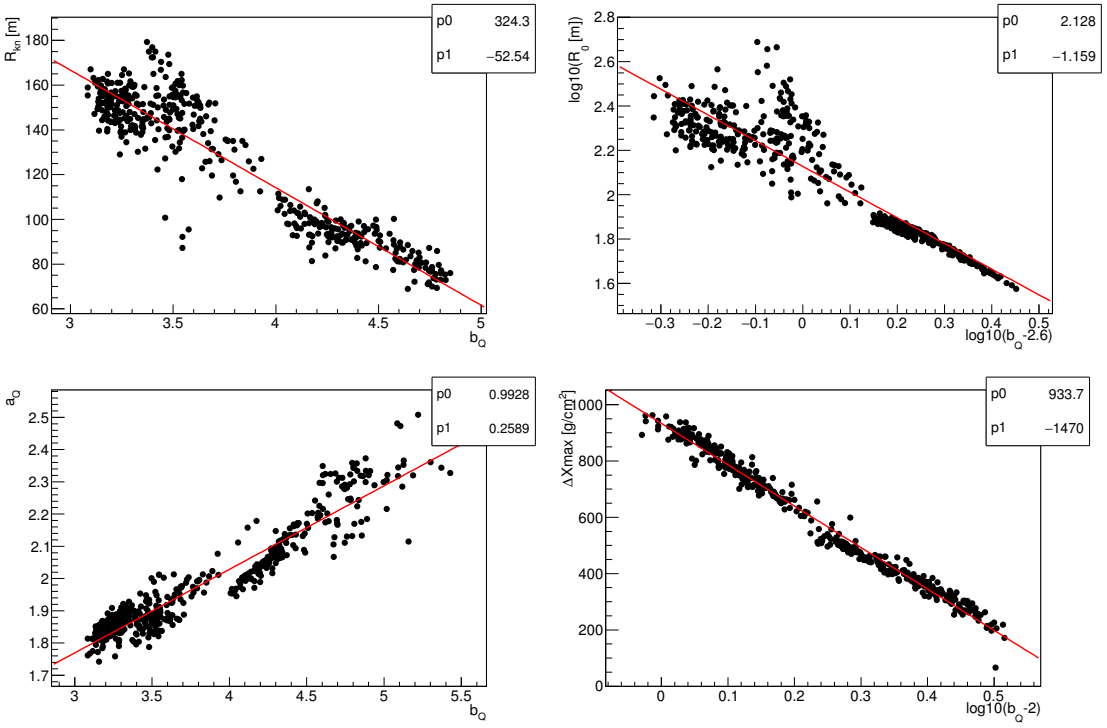

FIGURE 7.8: Correlation of the LDF parameters with the steepness b_Q and correlation of b_Q with the depth of the shower maximum ΔX_{max}.

TABLE 7.2: Q_{200} parametrization. Q_{200} in ph/m^2. E_0 in PeV.

	a_q	b_q
gamma	4.64	0.986
proton	4.26	0.936
iron	3.79	0.866

There are two additional aspects on Q_{200} which were not investigated yet:

- **Dependence of Q_{200} on X_{max}.** According to this model, Q_{200} is the parameter, which is a function of the primary energy and the particle type only. Most likely, Q_{200} for a fixed energy is scattered around the mean value and the parameters of the distribution depend again on ΔX_{max}. Thus, such an effect will broaden the predicted energy resolution.

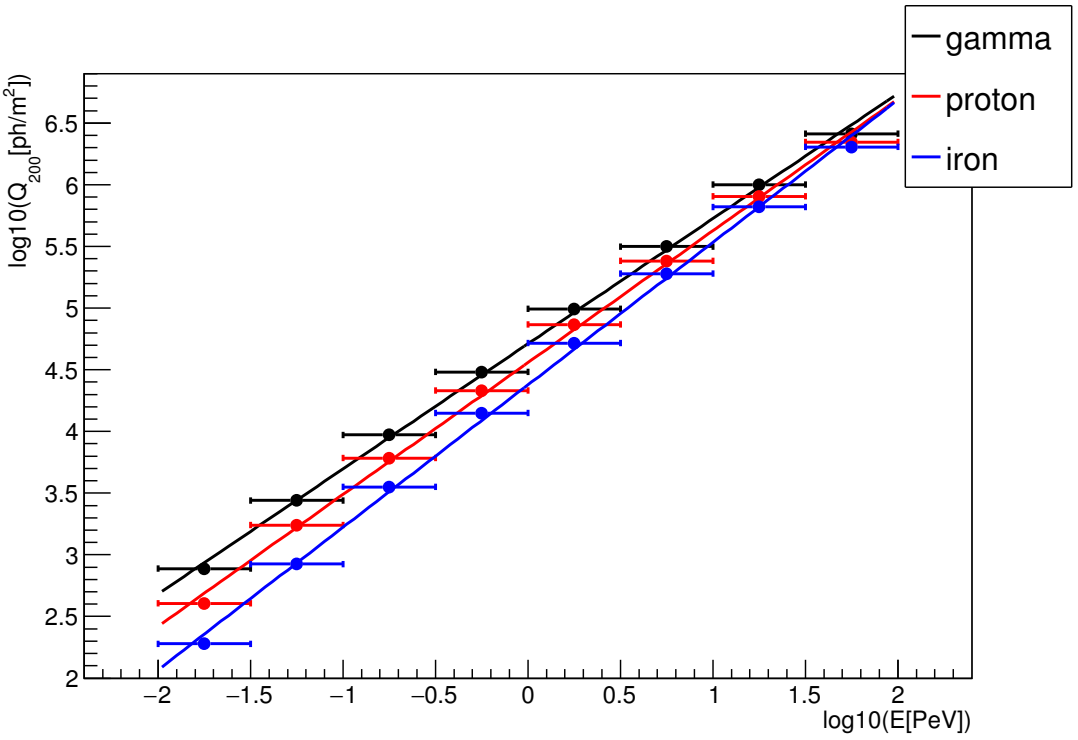

FIGURE 7.9: Q_{200} as a function of energy.

- **Dependence of Q_{200} on observation level h_{obs}.** The Monte Carlo data have been produced for the altitude of 675 m a.s.l. (Tunka altitude). Generally speaking, the shape of the LDF should be transformed accordingly with altitude. One can assume naively, that the LDF shape remains the same and only Q_{200} is a function of h_{obs}. In the most complex case, it could be that the LDF parameters transform accordingly with h_{obs}.

7.4.5 Parametrization of X_{max}

X_{max} distributions for each type of the primary particle were simulated by CORSIKA 7.35 (2013) [96] with the recently revised high-interaction model QGSJETII-04 [109]. Five sets were produced for logarithmically equidistant energies from $10^{15.5}$ to $10^{17.5}$ eV and for five various representative primaries: gamma, proton, helium, nitrogen and iron. Each energy bin for each mass group contains 10,000 showers. The simulation was optimised using the statistical thinning $\epsilon = 10^{-4}$ with the weight $w = \epsilon \cdot E/\text{GeV}$.

Each X_{max} distribution approximates by a shifted Gamma distribution with the following p.d.f:

$$P_\gamma(x) = \frac{(x - x_0)^{\gamma-1}}{\Gamma(\gamma)\beta^\gamma} \exp\left(-\frac{x - x_0}{\beta}\right) \tag{7.8}$$

for $x \geq x_0$ and $\gamma, \beta > 0$.

The mean and the standard deviation of this distribution can be expressed as follows:

$$\overline{x} = \beta\gamma + x_0;$$

$$\sigma = \beta\sqrt{\gamma}.$$

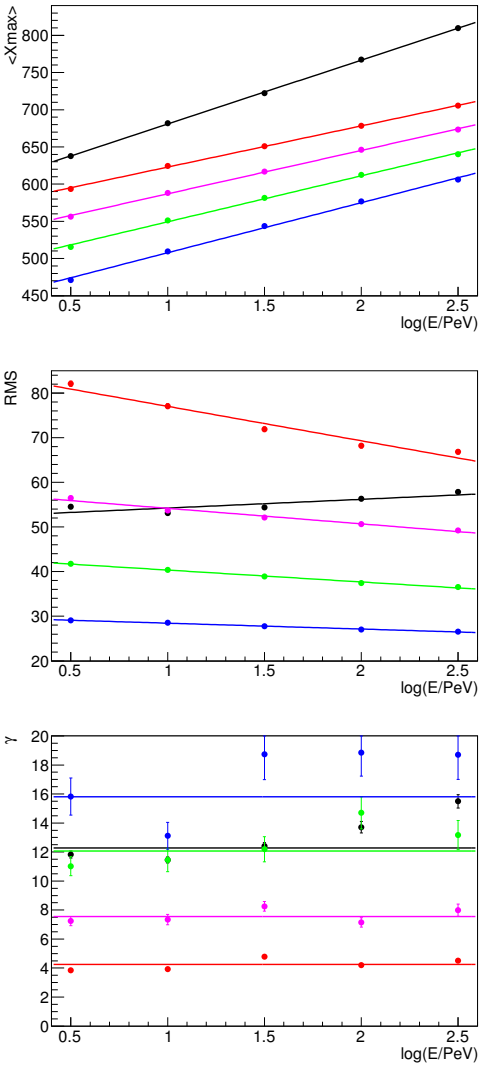

FIGURE 7.10: Parameters of Gamma distribution as a function of energy. In different colors are shown: gamma (*black*), proton (*red*), helium (*magenta*), nitrogen (*green*), iron (*blue*).

The parameters $\overline{x}$, σ and γ were chosen to describe the Gamma distribution. Here, the following linear interpolation with energy was used:

$$\overline{x} = a_1 \log_{10}(E/\text{PeV}) + a_2;$$

$$\sigma = b_1 \log_{10}(E/\mathrm{PeV}) + b_2;$$

$$\gamma = c_1.$$

TABLE 7.3: X_{max} parametrization

	a_1	a_2	b_1	b_2	γ
gamma	595	85.8	52.3	1.96	12.3
proton	568	55.5	84.7	-7.83	4.27
helium	529	58.5	57.7	-3.54	7.52
nitrogen	488	62.1	42.9	-2.69	12.4
iron	441	67.4	29.6	-1.31	16.7

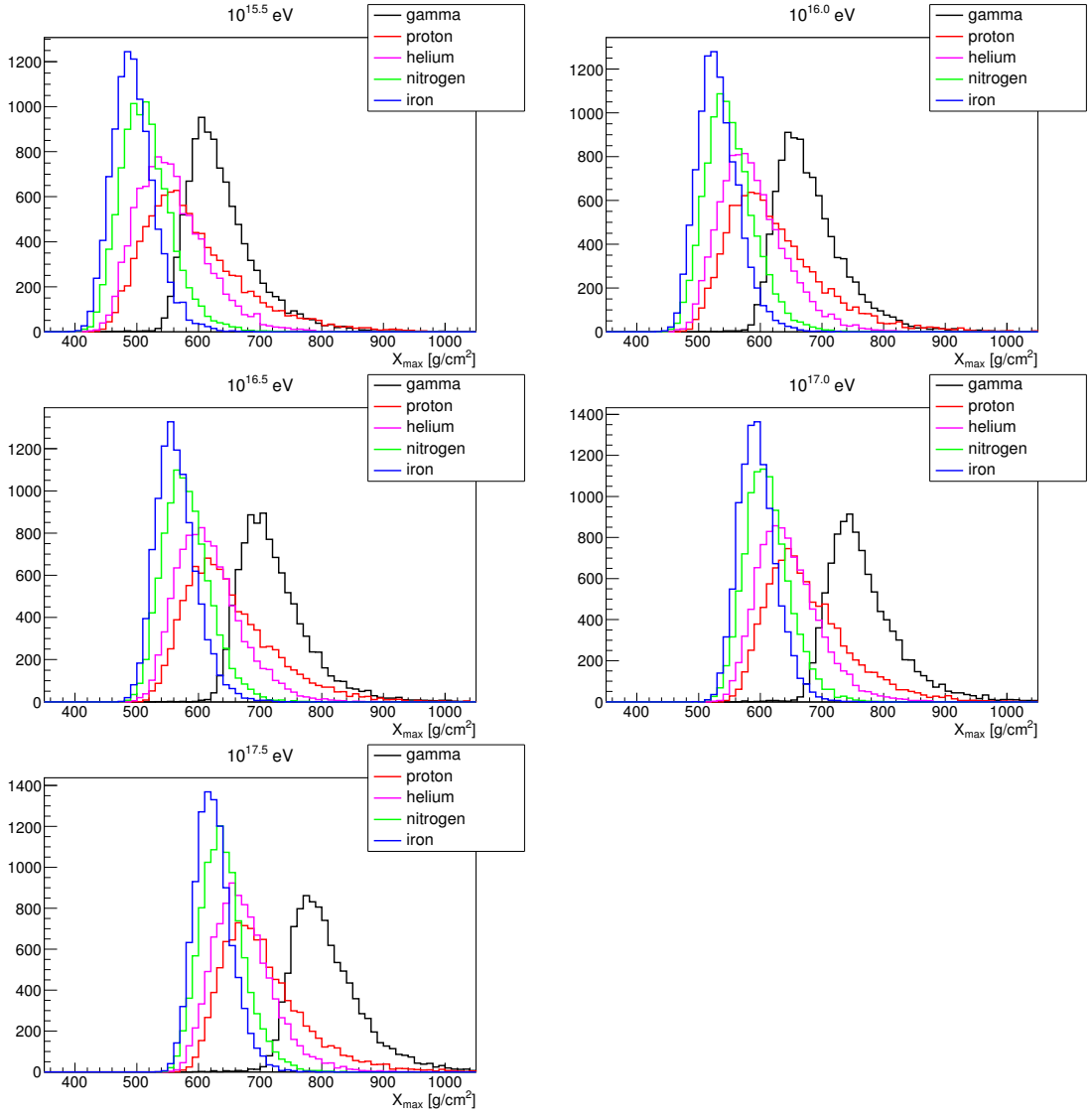

FIGURE 7.11: Distributions of X_{max} for various primaries and energies.

7.5 Performance of the Tunka-133 array

The CHERRY program was tested first on the detector layout of the Tunka-133 array and the performance of such an array was investigated. The simulation included a realistic Tunka detector response (100 m RG-58 + 8-inch PMT + pre-amplifier), the detector angular acceptance and the transmission of the acrylic input window of the detector (Sect. 4.1). The trigger was simulated under the conditions: 5σ level above average fluctuations of the NSB, time gate is 20 ns. Parameters that were used to perform the data set for this analysis are listed in the following table:

Primaries	proton, helium, nitrogen, iron
Energy range	from 0 to 3 $\log_{10}$ PeV with step 0.1
Zenith angle range	0°..45°
Azimuth angle range	0°..360°
Statistics	10,000 showers/bin/primary
Array	1100×1100 m^2

The showers were reconstructed with two basic programs `t133_14at` and `spe_14` used for the reconstruction of the real data. Uncertainties for the four main shower parameters were estimated: direction, core position, energy and depth of the shower maximum. The results are shown in Fig. 7.12. The contribution of different nuclei groups was given by the polygonato model [71] (Appendix A) and the resolution represents 68% containment.

Under the standard radial cut $R < 450$ m (Sect. 4.4.2), the array reaches 100% efficiency at an energy of $3 \cdot 10^{15}$ eV, roughly at the position of the knee in the spectrum of cosmic rays. At these energies the array resolution is predicted as follows: shower direction – 1°, core position – 3 m, energy – 13%, depth of the shower maximum – 18 g/cm^2. Above 10^{17} eV the array resolution becomes better: shower direction – 0.3°, core position – 2 m, energy – 4% and depth of the shower maximum – 14 g/cm^2. Systematic uncertainties above $3 \cdot 10^{15}$ eV do not exceed 10% for energy and 2 m for core. Systematic uncertainties for the depth of the shower maximum in turn may reach 30–40 g/cm^2 and must be carefully taken into account in the data analysis.

With an increase of the radial cut the uncertainties becomes larger. Under the radial cut $R < 800$ m, the array reaches 100% efficiency at an energy of $8 \cdot 10^{15}$ eV.

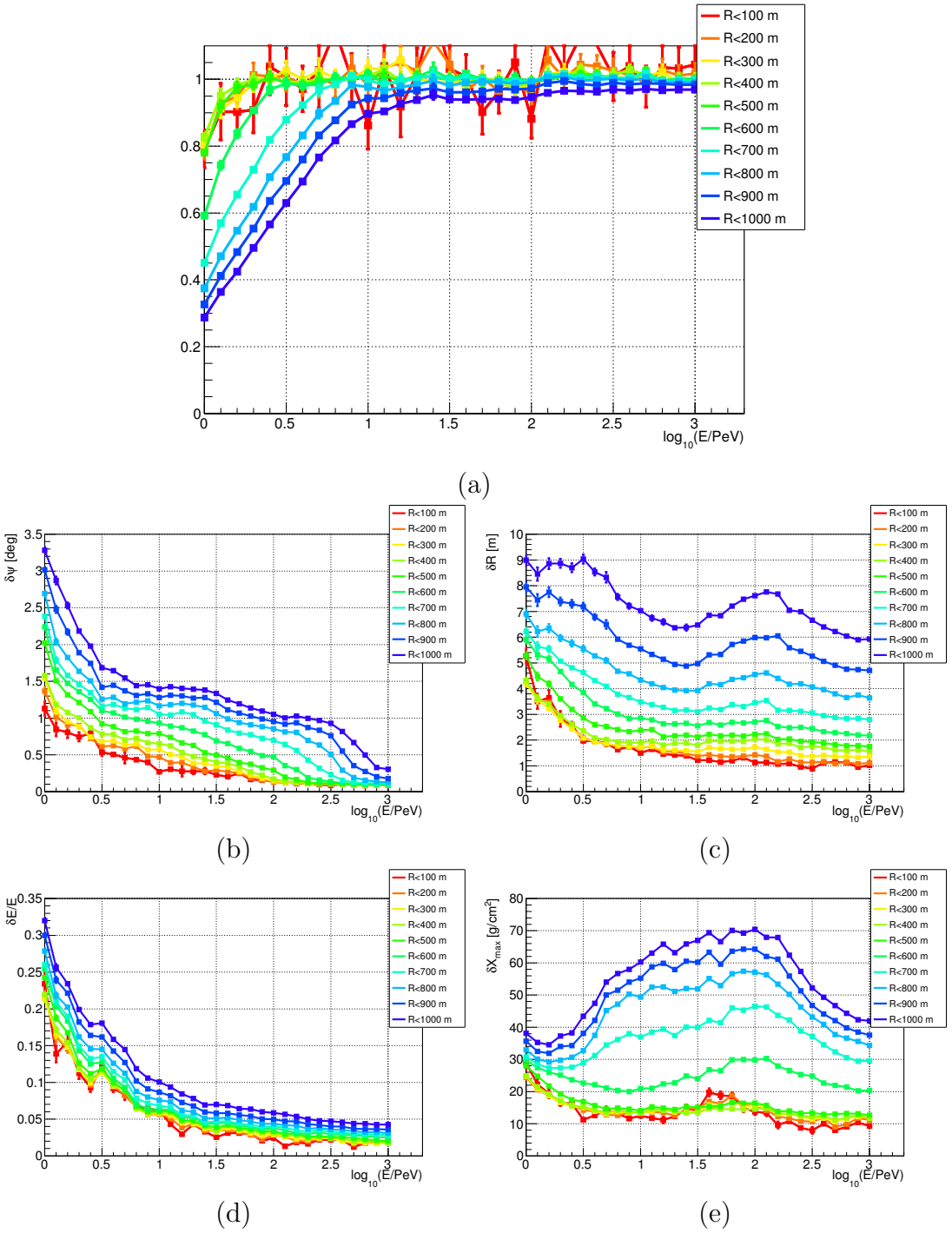

FIGURE 7.12: Simulation results of the Tunka-133 array performance: the array efficiency (a), the arrival direction resolution (b), the core resolution (c), the energy resolution (d), the shower maximum resolution (e). Colour scale represents different radial cuts applied on the shower core: from 100 m to 1000 m from the array center with a step of 100 m.

At these energies the angular resolution is 1.2°, the core resolution is 4.5 m, the energy resolution is 8%, and the resolution of the shower depth is 50 g/cm^2.

With the radial cuts $R < 800 - 1000$ m the core resolution and the resolution of the shower depth behave quite different. At some energy both resolutions start to deteriorate again. Most probably this effect reflects the gap between the inner part of the array and the outer clusters.

However, the CHERRY predictions seem a little optimistic. In the following table the comparison of the CHERRY results with the results obtained using the chessboard method [95] are summarized:

	chessboard	CHERRY
array M: $R < 450$ m		
$E > 10^{16}$ eV	$\delta E/E = 8\%$	$\delta E/E = 6\%$
	$\delta R = 8$ m	$\delta R = 2$ m
$E > 5 \cdot 10^{16}$ eV	$\delta E/E = 4\%$	$\delta E/E = 4\%$
	$\delta R = 6$ m	$\delta R = 2$ m
array L: $R < 800$ m		
$E > 5 \cdot 10^{16}$ eV	$\delta E/E = 12\%$	$\delta E/E = 5\%$
	$\delta R = 13$ m	$\delta R = 6$ m

An explanation of differences in the results of two methods can be the following. The internal shower fluctuations are not simulated property yet and at large distances from the shower core pulse fluctuations are probably underestimated. Nevertheless, the program has a great potential. Even at this stage it provides realistic results and can be improved in future.

Chapter 8

Summary and outlook

Cosmic rays were discovered more than hundred years ago and their properties are still subject of intense research. However, the origin of cosmic rays remains unknown. To examine this question neutral particles are perfectly suited as messengers.

In the last decade a great success in the gamma ray astronomy has been achieved. Despite a significant number of gamma ray sources detected in the TeV range the gamma ray sky above 10–100 TeV is not well studied yet. However, this range is of great interest: there must be local sources that accelerate cosmic rays up to PeV energies (pevatrons). Such hypothetical objects will have gamma ray spectra up to several 100 TeV. Detection of a source with such a spectrum continuing up to these energies will support the hypothesis of the hadronic acceleration scenario.

The HiSCORE experiment was designed to study the gamma ray sky above 30 TeV and to measure the spectrum and the mass composition of cosmic rays above 100 TeV. In 2013 the 9-station array was successfully deployed at the Tunka site in Russia, where the existing Cherenkov experiment Tunka-133 operates for many year.

Basic technical methods and algorithms used in the Tunka-133 experiment to reconstruct showers parameters were introduced. The recent results has been achieved in the all-particle spectrum reconstruction and the mass composition analysis of cosmic rays in the PeV range were shown.

The knee in the spectrum of cosmic rays seems to have a compound structure and the spectrum can be fitted by a power law with 3 indices:

$$\gamma = \begin{cases} 3.23 \pm 0.01, & 6 \cdot 10^{15} < E \leq 2 \cdot 10^{16} \text{ eV}, \\ 3.00 \pm 0.01, & 2 \cdot 10^{16} < E \leq 3 \cdot 10^{17} \text{ eV}, \\ 3.33 \pm 0.15, & 3 \cdot 10^{17} < E \leq 10^{18} \text{ eV}. \end{cases}$$

The spectrum before the knee was complimented with the recent HiSCORE-9 data. A spectral index of -2.65 ± 0.01 was observed. The spectrum in this region consists with the results obtained by the Tunka-25 experiment.

The mass composition analysis developed in this work shows that the composition becomes heavier ($\ln A$ from 2.0 to 2.7) up to 10^{17} eV and then becomes lighter again ($\ln A$=2.1 at $6 \cdot 10^{17}$ eV). Moreover similar to KASCADE-Grande a knee-like structure in the spectrum of the heavy components was observed at an energy of $7 \cdot 10^{16}$ eV.

To achieve a required angular resolution of 0.1°, detectors must be synchronized with the sub-ns precision. The LED calibration revealed the perfect timing for both DAQs: 190 ps (DAQ-1), 460 ps (DAQ-2).

The data collected by DAQ-1 were analysed and the chessboard method demonstrated the following performance of the HiSCORE-9 array:

$$\begin{array}{ll} \text{at } E^{\gamma}_{th} = 50 \text{ TeV} & \delta\psi = 0.12^{\circ} \\ & \delta R = 12 \text{ m} \\ & \delta E/E = 18\% \\ \text{at } E^{\gamma}_{th} = 110 \text{ TeV} & \delta\psi = 0.04^{\circ} \\ & \delta R = 3 \text{ m} \\ & \delta E/E = 5\% \\ & \delta X_{max} = 27 \text{ g/cm}^2 \end{array}$$

The reconstruction procedure also demonstrates excellent characteristics: front residuals ~ 470 ns and uniformly distributed shower cores. Besides that, the cone shows very good angular acceptance up to 30°, which is the cut-off angle.

The detector parameters play an important role in Monte Carlo simulations. The major parameter is the detector threshold. It was estimated in three different ways and the results can be summarized as follows:

$$A^d_{th} = 130 \left(\frac{F}{1.4} \right) \text{ [p.e.] (LED calibration)},$$
$$A^d_{th} = 100 \text{ [p.e.] (single station rate)},$$
$$A^d_{th} = 180 \text{ [p.e.] (detector multiplicity)}.$$

The pure Monte Carlo predicts a discriminator threshold of 100 p.e., which is probably too optimistic. Two other methods based on the real data provide much closer values of 130 p.e. and 180 p.e. The obtained difference in the last case is caused by the unknown noise factor F, which was only estimated and probably is also underestimated.

The most comprehensive Monte Carlo simulations shown, that to observe a Crab-like source by HiSCORE with a significance of 5σ after one year an area of $4\,\text{km}^2$ is needed. When a background rejection is used, the area can be reduced to a scale of $1\,\text{km}^2$. We expect that the Tunka site will allow to cover an area up to $5\,\text{km}^2$ using HiSCORE detectors. It seems that the predicted array sensitivity in case of HiSCORE-9 is quite low and an array optimisation probably will be required for further array extensions. The following parameters might be changed accordingly: the detector spacing ($< 150\,\text{m}$) and the number of PMTs per station (>4). The PMT can be also enlarged (up to 12-inch in diameter) and covered by UV-wavelength shifters. Deployment additionally of cheap wide-angle IACT telescopes and charged particles detectors will also help to improve the background rejection.

In 2014 the number of HiSCORE detectors was increased. Now the array includes 28 stations. It covers an area of $0.25\,\text{km}^2$ and has a dense core with a spacing of 75 m. The HiSCORE detector concept found its place in the project of the complex array TAIGA. The new array will be additionally complemented with IACT telescopes and scintillation detectors.

The new fast code CHERRY to simulate Cherenkov non-imaging arrays was developed. The program was tested and the Tunka-133 performance was studied. The analysis shown a good agreement with results obtained using the chessboard method. However, it seems that predicted uncertainties are low. Most probably this is due to the fact that fluctuations of Cherenkov light were underestimated. Thus, this problem should be investigated in future.

Appendix A

Polygonato model

The all-particle energy spectrum and the knee can be successfully interpreted with a phenomenological model, named *polygonato* model [71]. The model describes the *knee* in the all-particle energy spectrum as a result of subsequent cut-offs for individual elements, starting with the proton component at 4.5 PeV, and the second change of the spectral index around 0.4 EeV as due to the end of stable elements ($Z = 92$). The rigidity dependent cut-off $\hat{E_Z} = \hat{E_p} \cdot Z$ with the hypothesis of a common difference in spectral slope $\Delta\gamma = \gamma_Z - \gamma_c$ is the best choice to describe the all-particle spectrum:

$$\frac{d\Phi_Z}{dE_0} = \Phi_Z^0(E_0) E_0^{\gamma_Z} \left[1 + \left(\frac{E_0}{\hat{E_Z}} \right)^{\epsilon_c} \right]^{-\frac{\Delta\gamma}{\epsilon_c}} , \tag{A.1}$$

where $\hat{E_p}$=4490 TeV, $\Delta\gamma$=2.10, ϵ_c=1.90.

The absolute flux Φ_Z^0 and the spectral index γ_Z quantify the power law. The flux above the cut-off energy is modelled by a second and steeper power law. γ_c and ϵ_c characterize the change in the spectrum at the cut-off energy $\hat{E_Z}$. Both parameters are assumed to be identical for all spectra, γ_c being the hypothetical slope beyond the knee and ϵ_c describes the smoothness of the transition from the first to the second power law.

Fig. A.1 represent the all-particle measured by different experiments as a superposition of elements with Z from 1 to 92.

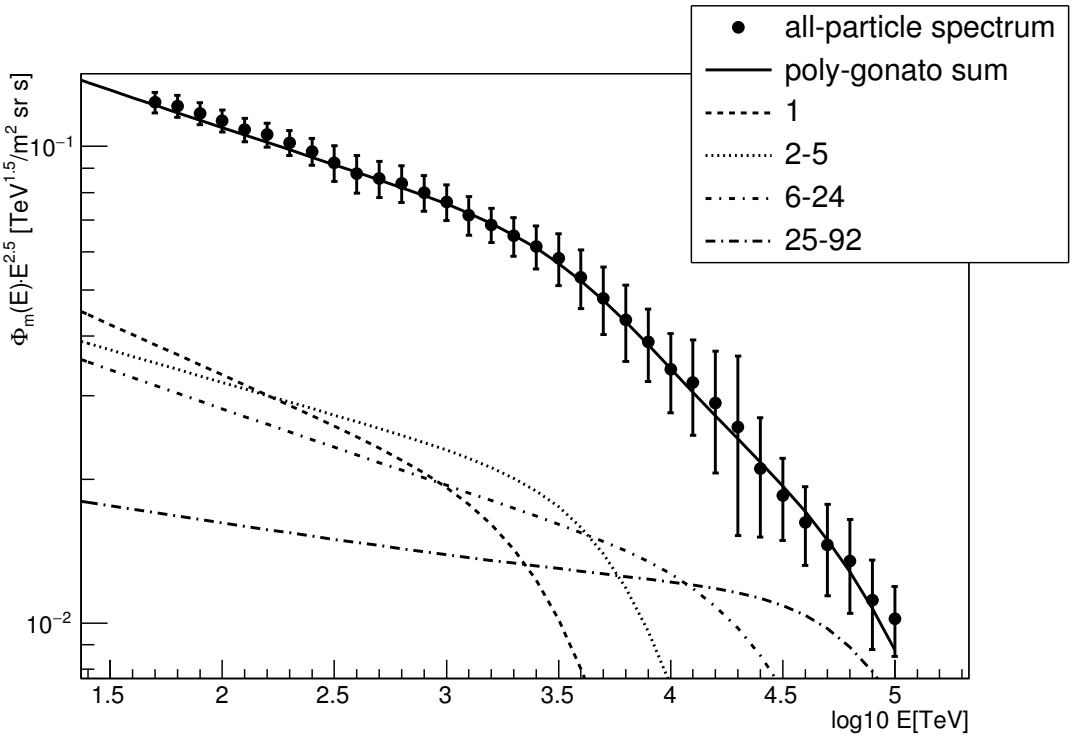

FIGURE A.1: The all-particle spectrum and its parametrization by the polygonato model [71]. Four different nuclei groups are shown.

TABLE A.1: Absolute flux $\Phi_Z^0[(\mathrm{m}^2\ \mathrm{sr\ s\ TeV})^{-1}]$ at $E_0 = 1$ TeV/nucleus and spectral index γ_Z of cosmic-ray elements [71].

Z		Φ_Z^0	$-\gamma_Z$	Z		Φ_Z^0	$-\gamma_Z$	Z		Φ_Z^0	$-\gamma_Z$
1	H	$8.73 \cdot 10^{-2}$	2.71	32	Ge	$4.02 \cdot 10^{-6}$	2.54	63	Eu	$1.58 \cdot 10^{-7}$	2.27
2	He	$5.71 \cdot 10^{-2}$	2.64	33	As	$9.99 \cdot 10^{-7}$	2.54	64	Gd	$6.99 \cdot 10^{-7}$	2.25
3	Li	$2.08 \cdot 10^{-3}$	2.54	34	Se	$2.11 \cdot 10^{-6}$	2.53	65	Tb	$1.48 \cdot 10^{-7}$	2.24
4	Be	$4.74 \cdot 10^{-4}$	2.75	35	Br	$1.34 \cdot 10^{-6}$	2.52	66	Dy	$6.27 \cdot 10^{-7}$	2.23
5	B	$8.95 \cdot 10^{-4}$	2.95	36	Kr	$1.30 \cdot 10^{-6}$	2.51	67	Ho	$8.36 \cdot 10^{-8}$	2.22
6	C	$1.06 \cdot 10^{-2}$	2.66	37	Rb	$6.93 \cdot 10^{-7}$	2.51	68	Er	$3.52 \cdot 10^{-7}$	2.21
7	N	$2.35 \cdot 10^{-3}$	2.72	38	Sr	$2.11 \cdot 10^{-6}$	2.50	69	Tm	$1.02 \cdot 10^{-7}$	2.20
8	O	$1.57 \cdot 10^{-2}$	2.68	39	Y	$7.82 \cdot 10^{-7}$	2.49	70	Yb	$4.15 \cdot 10^{-7}$	2.19
9	F	$3.28 \cdot 10^{-4}$	2.69	40	Zr	$8.42 \cdot 10^{-7}$	2.48	71	Lu	$1.72 \cdot 10^{-7}$	2.18
10	Ne	$4.60 \cdot 10^{-3}$	2.64	41	Nb	$5.05 \cdot 10^{-7}$	2.47	72	Hf	$3.57 \cdot 10^{-7}$	2.17
11	Na	$7.54 \cdot 10^{-4}$	2.66	42	Mo	$7.79 \cdot 10^{-7}$	2.46	73	Ta	$2.16 \cdot 10^{-7}$	2.16
12	Mg	$8.01 \cdot 10^{-3}$	2.64	43	Tc	$6.98 \cdot 10^{-8}$	2.46	74	W	$4.16 \cdot 10^{-7}$	2.15
13	Al	$1.15 \cdot 10^{-3}$	2.66	44	Ru	$3.01 \cdot 10^{-7}$	2.45	75	Re	$3.35 \cdot 10^{-7}$	2.13
14	Si	$7.96 \cdot 10^{-3}$	2.75	45	Rh	$3.77 \cdot 10^{-7}$	2.44	76	Os	$6.42 \cdot 10^{-7}$	2.12
15	P	$2.70 \cdot 10^{-4}$	2.69	46	Pd	$5.10 \cdot 10^{-7}$	2.43	77	Ir	$6.63 \cdot 10^{-7}$	2.11
16	S	$2.29 \cdot 10^{-3}$	2.55	47	Ag	$4.54 \cdot 10^{-7}$	2.42	78	Pt	$1.03 \cdot 10^{-6}$	2.10
17	Cl	$2.94 \cdot 10^{-4}$	2.68	48	Cd	$6.30 \cdot 10^{-7}$	2.41	79	Au	$7.70 \cdot 10^{-7}$	2.09
18	Ar	$8.36 \cdot 10^{-4}$	2.64	49	In	$1.61 \cdot 10^{-7}$	2.40	80	Hg	$7.43 \cdot 10^{-7}$	2.08
19	K	$5.36 \cdot 10^{-4}$	2.65	50	Sn	$7.15 \cdot 10^{-7}$	2.39	81	Ti	$4.28 \cdot 10^{-7}$	2.06
20	Ca	$1.47 \cdot 10^{-3}$	2.70	51	Sb	$2.03 \cdot 10^{-7}$	2.38	82	Pb	$8.06 \cdot 10^{-7}$	2.05
21	Sc	$3.04 \cdot 10^{-4}$	2.64	52	Te	$9.10 \cdot 10^{-7}$	2.37	83	Bi	$3.25 \cdot 10^{-7}$	2.04
22	Ti	$1.14 \cdot 10^{-3}$	2.61	53	I	$1.34 \cdot 10^{-7}$	2.37	84	Po	$3.99 \cdot 10^{-7}$	2.03
23	V	$6.31 \cdot 10^{-4}$	2.63	54	Xe	$5.74 \cdot 10^{-7}$	2.36	85	At	$4.08 \cdot 10^{-8}$	2.02
24	Cr	$1.36 \cdot 10^{-3}$	2.67	55	Cs	$2.79 \cdot 10^{-7}$	2.35	86	Rn	$1.74 \cdot 10^{-7}$	2.00
25	Mn	$1.35 \cdot 10^{-3}$	2.46	56	Ba	$1.23 \cdot 10^{-6}$	2.34	87	Fr	$1.78 \cdot 10^{-8}$	1.99
26	Fe	$2.04 \cdot 10^{-2}$	2.59	57	La	$1.23 \cdot 10^{-7}$	2.33	88	Ra	$7.54 \cdot 10^{-8}$	1.98
27	Co	$7.51 \cdot 10^{-5}$	2.72	58	Ce	$5.10 \cdot 10^{-7}$	2.32	89	Ac	$1.97 \cdot 10^{-8}$	1.97
28	Ni	$9.96 \cdot 10^{-4}$	2.51	59	Pr	$9.52 \cdot 10^{-8}$	2.31	90	Th	$8.87 \cdot 10^{-8}$	1.96
29	Cu	$2.18 \cdot 10^{-5}$	2.57	60	Nd	$4.05 \cdot 10^{-7}$	2.30	91	Pa	$1.71 \cdot 10^{-8}$	1.94
30	Zn	$1.66 \cdot 10^{-5}$	2.56	61	Pm	$8.30 \cdot 10^{-8}$	2.29	92	U	$3.54 \cdot 10^{-7}$	1.93
31	Ga	$2.75 \cdot 10^{-6}$	2.55	62	Sm	$3.68 \cdot 10^{-7}$	2.28				

Appendix B

Photomultiplier tubes

HAMAMATSU

PHOTOMULTIPLIER TUBE R5912

APPLICATIONS

● **For High Energy Physics**

GENERAL

Parameter		Description/Value	Unit
Spectral Response		300 to 650	nm
Wavelength of Maximum Response		420	nm
Photocathode	Material	Bialkali	—
	Effective Area	530 (Min. 450)	cm^2 Typ.
Window Material		Borosilicate glass	—
Dynode	Structure	Box and Line	—
	Number of Stages	10	—
Direct Interelectrode Capacitances (Approx.)	Anode to Last Dynode	3	pF
	Anode to All Other Dynode	7	pF
Base		20-pin base JEDEC B20-102	—
Weight		Approx. 720	g
Suitable Socket		E678-20A (supplied)	—

CHARACTERISTICS (at 25°C)

Parameter		Min.	Typ.	Max.	Unit
Cathode Sensitivity	Luminous (2856K)	—	70	—	μA/lm
	Radiant at 420nm	—	72	—	mA/W
	Blue (CS 5-58 filter)	—	9.0	—	μA/lm-b
	Quantum Efficiency at 390nm	—	22	—	%
Anode Sensitivity [1]	Luminous (2856K)	—	700	—	A/lm
	Radiant at 420nm	—	7.2×10^5	—	A/W
Gain [1]		—	1.0×10^7	—	—
Supply Voltage for Gain of 10^7		—	1500	1800	V
Anode Dark Current (after 30min. storage in darkness) [1]		—	50	700	nA
Dark Count (after dark condition for 15 hours) [1]		—	4	8	kcps
Time Response [1]	Anode Pulse Rise Time	—	3.8	—	ns
	Electron Transit Time	—	55	—	ns
	Transit Time Spread (FWHM) [3]	—	2.4	—	ns
Pre Pulse [4]	4ns to 20ns before Main pulse	—	0.5	2	%
Late Pulse [3]	8ns to 60ns after Main pulse	—	1.5	3	%
After Pulse [3]	100ns to 16μs after Main pulse	—	2	10	%
Single Photoelectron	PHD (Peak to Valley Ratio)	—	2.5	—	—
Pulse Linearity [2]	at ±2% Deviation	—	60	—	mA
	at ±5% Deviation	—	80	—	mA
Magnetic characteristics (at 200mG/20μT)	Sensitivity Degradation	—	10	—	%

1) Measured with the condition shown in the Table 1. 2) Measured with the condition shown in the Table 2.
3) Measured with 0.25 photoelectrons detection threshold (at single photoelectron/ event).
4) Measured with 0.25 photoelectrons detection threshold (at 50 photoelectron/ event).

PHOTOMULTIPLIER TUBE R5912

Table 1: VOLTAGE DISTRIBUTION RATIO AND SUPPLY VOLTAGE

Electrodes	K	Dy1	F2	F1	F3	Dy2	Dy3	Dy4	Dy5	Dy6	Dy7	Dy8	Dy9	Dy10	P
Ratio	11.3	0	0.6	0	3.4	5	3.33	1.67	1	1	1	1	1	1	

Supply Voltage: 1500Vdc, K: Cathode, Dy: Dynode, P: Anode, F: Focus

Table 2: TAPERED VOLTAGE DISTRIBUTION RATIO FOR LINEARITY MEASUREMENT

Electrodes	K	Dy1	F2	F1	F3	Dy2	Dy3	Dy4	Dy5	Dy6	Dy7	Dy8	Dy9	Dy10	P
Ratio	11.3	0	0.6	0	3.4	5	3.33	1.67	1	1.2	1.5	2.2	3	2.4	
Capacitors in μF												0.01	0.01	0.01	

Supply Voltage: 1500Vdc, K: Cathode, Dy: Dynode, P: Anode, F: Focus

MAXIMUM RATINGS (Absolute Maximum Values)

Parameter		Value	Unit
Supply Voltage	Between Anode and Cathode	1800	Vdc
	Between Anode and Last Dynode	300	V
Average Anode Current		0.1	mA
Average Cathode Current		100	nA
Ambient Temperature		-60 to +50	°C
Presure		7	atm

Figure 1: Typical Spectral Response

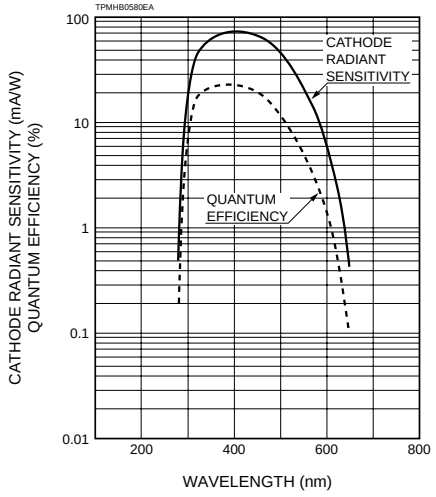

Figure 2: Typical Gain Caracteristic

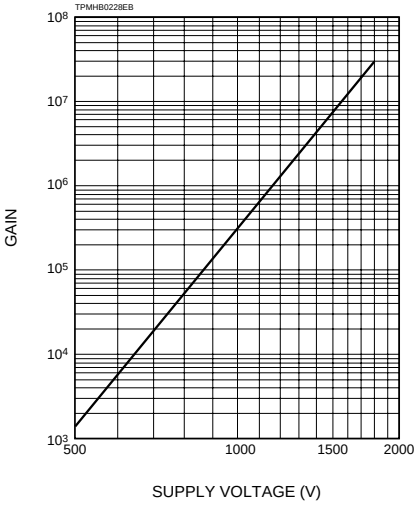

HAMAMATSU

Figure 3: Pulse Height Distribution

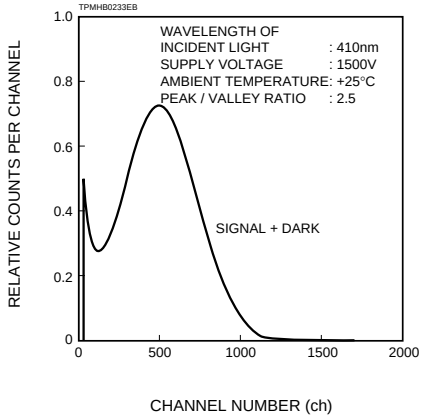

Figure 4: Transit Time Spread

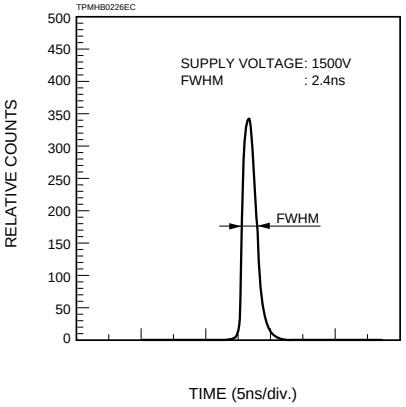

Figure 5: Typical Time Response

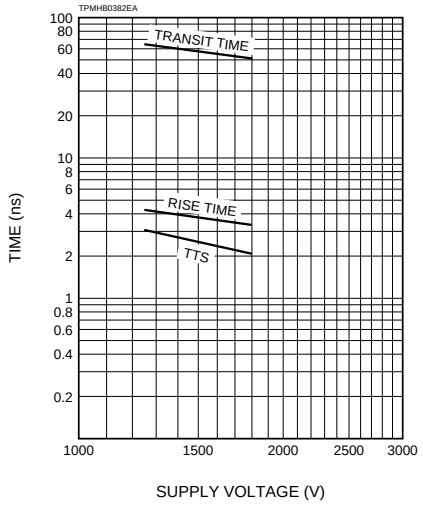

200 mm (8") photomultiplier
9352KB series data sheet

ET Enterprises electron tubes

1 description

The 9352KB is a 200mm (8") diameter end window photomultiplier with blue-green sensitive bialkali photocathode on a hemispherical window, and 6 BeCu dynodes of linear focused design for good linearity and timing. Metal fingers extend over the active area to ensure satisfactory operation at high ambient light levels.

2 applications

- high energy physics studies with high light levels (e.g. Cosmic Ray Shower studies in the night sky)

3 features

- 2π detection
- large active area
- internal collection efficiency optimised
- high light level capability
- fast time response
- low background glass envlope

4 window characteristics

	9352KB borosilicate
spectral range *(nm)	290 - 630
refractive index (n_d)	1.49
K (ppm)	300
Th (ppb)	250
U (ppb)	100

* wavelength range over which quantum efficiency exceeds 1 % of peak

6 characteristics

	unit	min	typ	max
photocathode: bialkali				
active diameter	mm		195	
active surface area	cm^2		480	
quantum efficiency at peak	%		30	
luminous sensitivity	µA/lm		70	
with CB filter		8	12	
with CR filter			1	
dynodes: 6LFBeCu				
anode sensitivity in divider A:				
nominal anode sevsitivity	A/lm		1	
max. rated anode sensitivity	A/lm		2	
overall V for nominal A/lm	V		1400	2300
overall V for max. rated A/lm	V		2000	
gain at nominal A/lm	$x10^6$		0.01	
dark current at 20°C:	nA			
dc at nominal A/lm	nA		0.2	5
dc at max. rated A/lm			0.5	
pulsed linearity (-5% deviation):	mA			
divider A	µA		50	
rate effect ($I_a$for $\Delta g/g$=1%):			1	
magnetic field sensitivity:				
the field for which the output decreases by 50%				
most sensitive direction	$T \times 10^{-4}$		0.4	
temperature coefficient:	$\%°C^{-1}$		± 0.5	
timing:				
multi electron rise time	ns		5	
multi electron (fwhm)	ns		8	
transit time	ns		50	
weight:	g		650	
maximum ratings:				
anode current	µA			100
cathode current	nA			5000
gain	$x\ 10^6$			0.03
sensitivity	A/lm			2
temperature	°C	-30		60
V (k-a)[1]	V			2400
V (k-d_1)	V			600
V (d-d)[2]	V			300
ambient pressure (absolute)	kPa			202

[1] subject to not exceeding max. rated sensitivity [2] subject to not exceeding max rated V(k-a)

5 typical spectral response curves

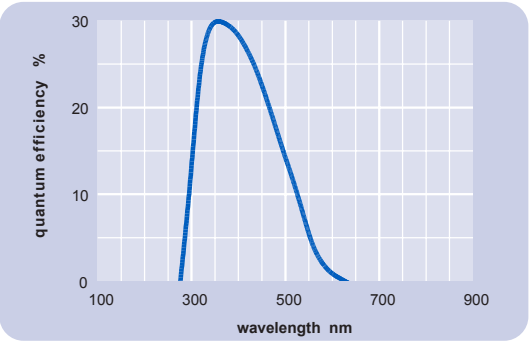

7 typical voltage gain characteristics

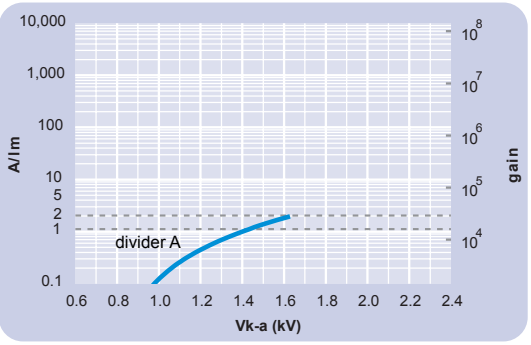

8 voltage divider distribution

	k	d_1	d_2	d_3	d_4	d_5	d_6	a	
A	600V	R	R	R	R	R	R		Standard

note: focus connected to d_1

Characteristics contained in this data sheet refer to divider A unless stated otherwise.

9 external dimensions mm

The drawings below show the 9352KB with the B20 cap fitted, and the 9352KFLB in flying lead format with a temporary B20 cap fitted. This temporary cap is attached as agreed with the customer.

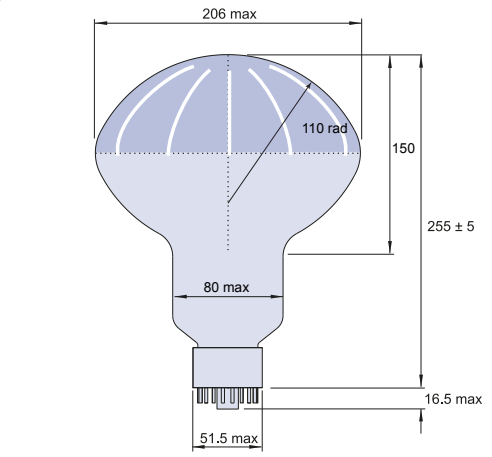

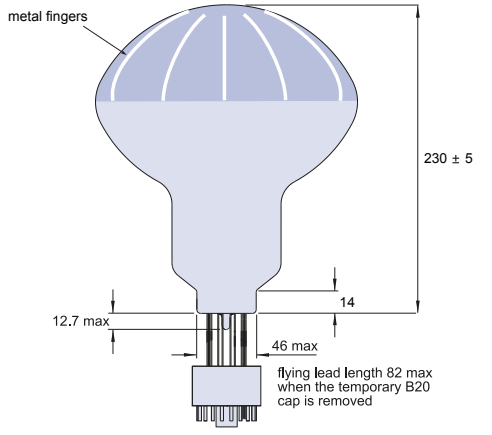

10 base configurations (viewed from below)

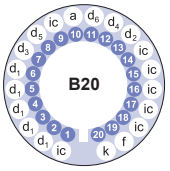

B20 cap
(for 9352KB & 9352KFLB)

'ic' indicates an internal connection

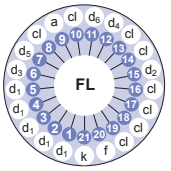

flying lead base
(for 9352FLB after removal
of temporary cap)

'ic' indicates an internal connection

note: focus connected to d_1

Our range of B20 sockets is available to suit the B20 cap. The socket range includes versions with or without a mounting flange, and versions with contacts for mounting directly onto printed circuit boards.

11 ordering information

The 9352KB meets the specification given in this data sheet. You may order **variants** by adding a suffix to the type number. You may also order **options** by adding a suffix to the type number. You may order product with **specification options** by discussing your requirements with us. If your selection option is for one-off order, then the product will be referred to as 9352KA. For a repeat order, ET Enterprises will give the product a two digit suffix after the letter B, for example B21. This identifies your specific requirement.

9352 ■ ■ ■

base options
K capped
KFL flying lead base with temporary cap

options
M supplied with spectral response calibration

specification options
B as given in data sheet
A single order to selected specification
Bnn repeat order to selected specification

12 voltage dividers

Voltage dividers for this type are available to special order. Please discuss your requirements with us.

ET Enterprises Limited
45 Riverside Way
Uxbridge UB8 2YF
United Kingdom
tel: +44 (0) 1895 200880
fax: +44 (0) 1895 270873
e-mail: sales@et-enterprises.com
web site: www.et-enterprises.com

ADIT Electron Tubes
300 Crane Street
Sweetwater TX 79556 USA
tel: (325) 235 1418
toll free: (800) 399 4557
fax: (325) 235 2872
e-mail: sales@electrontubes.com
web site: www.electrontubes.com

DS_ 93542B Issue 5 (26/02/14)

Appendix C

CORSIKA input-card

```
RUNNR   0                          number of run
EVTNR   1                          no. of first shower event
NSHOW   100                        no. of showers to simulate
PRMPAR  1                          primary particle code
ERANGE  1.000E+03  1.000E+03       energy range of primary (GeV)
THETAP  0  0                       range zenith angle (deg)
PHIP    0  360                     range azimuth angle (deg)
SEED    10000   0   0              seed for hadronic part
SEED    20000   0   0              seed for EGS4 part
SEED    30000   0   0              seed for Cherenkov part
SEED    40000   0   0              seed for IACT part
OBSLEV  675E2                      Tunka observation level (cm)
MAGNET  18.869  57.283             Tunka magnetic field(/uT)
ATMOD   3                          central European atmosphere for Feb.
LONGI   T  20.  T  F               longitude, stepsize(g/cm^2), fit, out
MAXPRT  1                          max. no. of printed events
CWAVLG  200.  700.                 Cherenkov wavelength band (nm)
CERSIZ  10                         bunch size Cherenkov photons
CSCAT   1   350E2   350E2         scatter Cherenkov events (cm)
PAROUT  F F                        particle output
CERFIL  F                          Cherenkov output file
IACT    IO_BUFFER 1990MB           IACT options
DIRECT  ./                         directory of particle output
TELFIL  ./score9st000000.iact      IACT output file
USER    esn                        user name
```

```
TELESCOPE   0.      0.      0.  100.    Cherenkov telescopes
TELESCOPE   0.      150E2   0.  100.
TELESCOPE   150E2   150E2   0.  100.
TELESCOPE   150E2   0.      0.  100.
TELESCOPE   150E2  -150E2   0.  100.
TELESCOPE   0.     -150E2   0.  100.
TELESCOPE  -150E2  -150E2   0.  100.
TELESCOPE  -150E2   0.      0.  100.
TELESCOPE  -150E2   150E2   0.  100.
EXIT
```

Appendix D

Data formats

D.1 Tunka-133

D.1.1 *Por*-file and *txt*-file

Source files written in binary (*por*) and ascii (*txt*) formats.

Name: ∗por.∗*cl*.

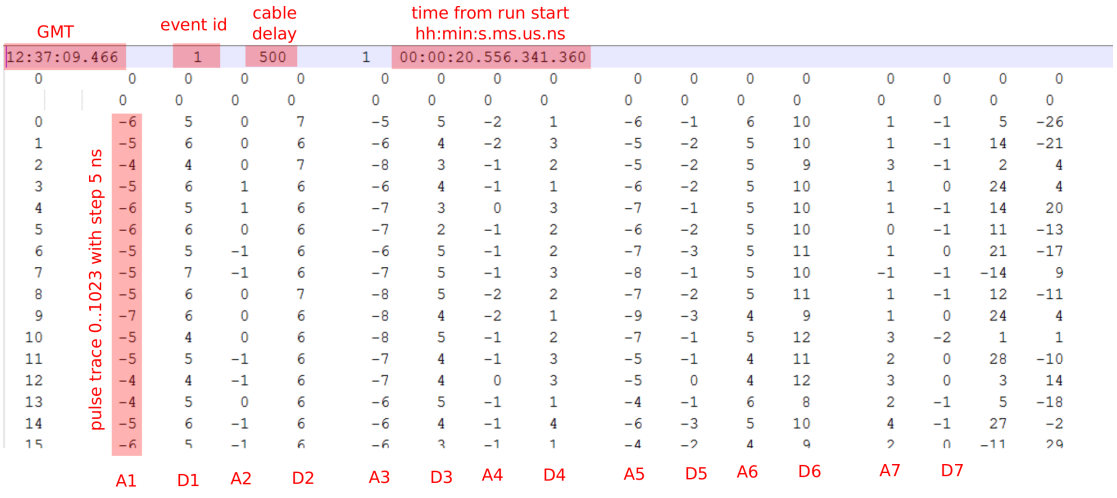

FIGURE D.1: Stricture of *por*- and *txt*-files.

D.1.2 *Tim*-file

Event merging.

Name: $*.tim$.

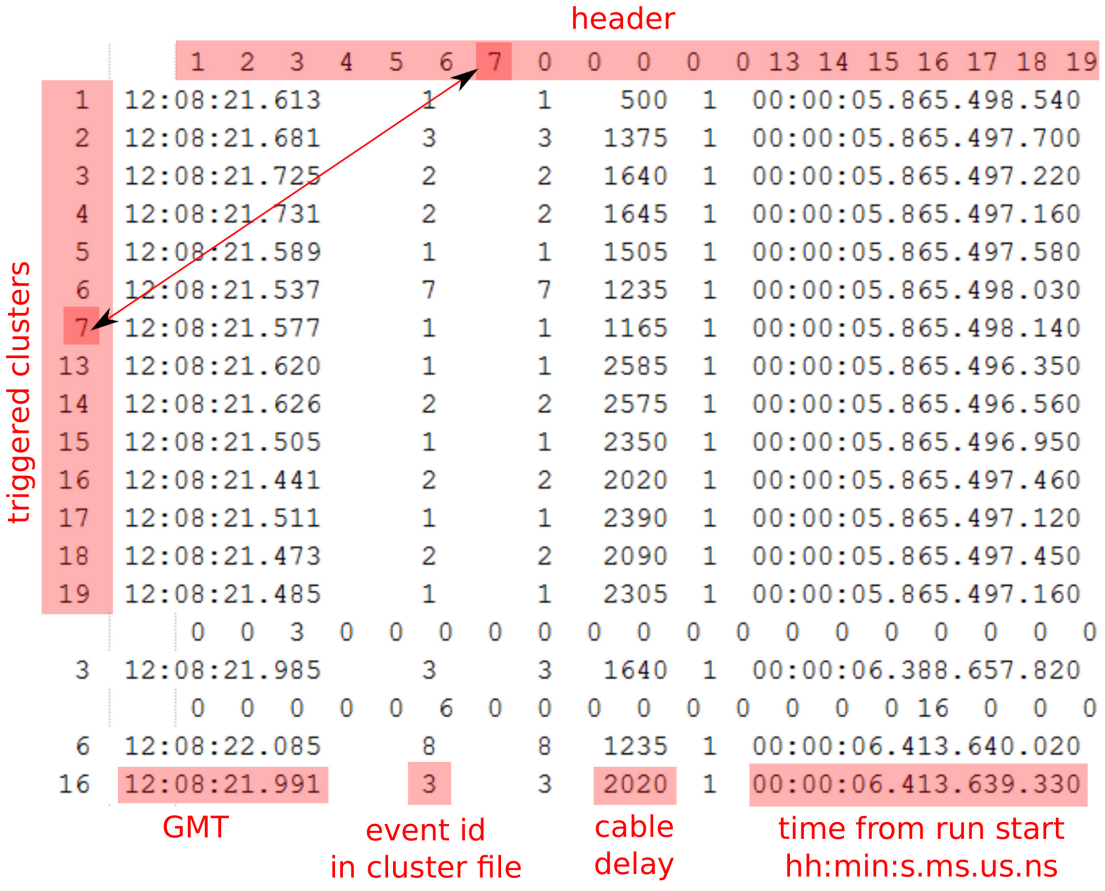

FIGURE D.2: Structure of *tim*-files.

D.1.3 *Prm*-file

Pulse parameters.

Name: $*.prm$.

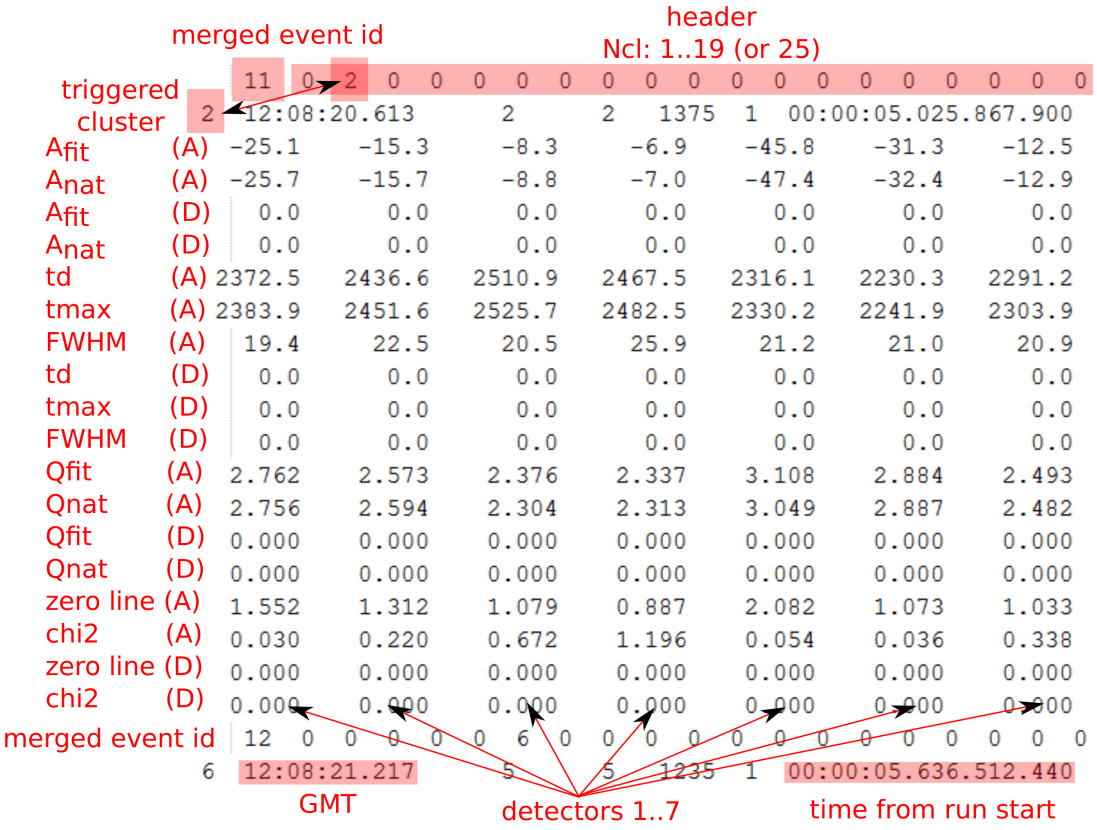

FIGURE D.3: Structure of *prm*-files.

D.2 Tunka-HiSCORE

D.2.1 *Tim*-file

Name: $*.tim$.

Event merging and pulse parameters.

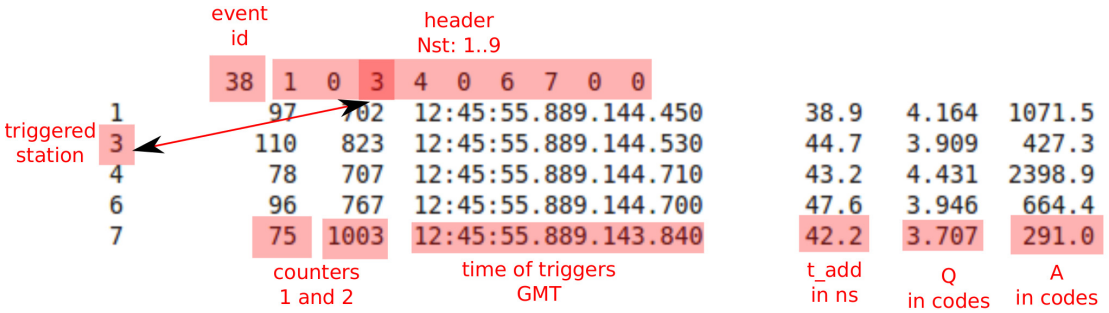

FIGURE D.4: Structure of *tim*-files.

Appendix E

Software developed for this work

E.1 DAQ software for HiSCORE-9

Description:	reading the binary data from DAQ-2
Directory:	`hiscore_read/`
Main script:	`diagnose.cpp`

Description:	event monitor
Directory:	`hiscore_monitor/`
Main script:	`monitor.cpp`

E.2 Monte Carlo simulations

Description:	HiSCORE-9 simulations
Directory:	`hiscore9/`
Main script:	`sim_9station.c`

Description:	Tunka-133 simulations
Directory:	`sim_tunka/`
Main script:	`sim_tunka.c`

E.3 LED calibration

Description: the LED calibration script
Directory: `led_calibration/`
Main script: `plot.cpp`

E.4 CHERRY

Description: the CHERRY program
Directory: `cherry/`
Main script: `cherry.cpp`

E.5 Miscellaneous

Description: Winston cone ray-tracing
Directory: `cone_acceptance/`
Main script: `fast_cone.cpp`

Description: NSB rate simulations for a single station
Directory: `nsb_rate_new/`
Main script: `nsb_rate.cpp`

Description: the polygonato model parametrization
Directory: `polygonato/`
Main script: `polygonato.c`

Description: average quantum efficiency
Directory: `average_qe/`
Main script: `plot.cpp`

Description: detector response
Directory: `detector_response/`
Main script: `plot.cpp`

Description: detector multiplicity
Directory: `multiplicity/`
Main script: `plot.cpp`

Bibliography

[1] Weekes T. C. et al. Observation of TeV gamma rays from the Crab nebula using the atmospheric Cerenkov imaging technique. *Astrophys. J.*, 342:379–395, 1989. URL `http://adsabs.harvard.edu/abs/1989ApJ...342..379W`.

[2] HESS Collaboration: Aharonian F. et al. Observation of the Crab nebula with HESS. *Astron. Astrophys.*, 457:889–915, 2006. ArXiv: astro-ph/0607333.

[3] MAGIC Collaboration: Lorenz E. et al. The MAGIC Telescope Project. In *Gev-TeV Gamma Ray astrophysics Workshop, Utah*, volume 515, page 510, 2000.

[4] VERITAS Collaboration: Weekes T. C. et al. VERITAS: the Very Energetic Radiation Imaging Telescope Array System. *Astropart. Phys.*, 17:221–243, 2002. ArXiv: astro-ph/0108478.

[5] CTA Consortium. Design Concepts for the Cherenkov Telescope Array. *Exp. Astron.*, 32:193–316, 2011.

[6] HAWC Collaboration: S. Westerhoff et al. HAWC: A next-generation all-sky gamma-ray telescope. *Adv. Space Res.*, 53:1492–1498, 2014.

[7] S. Cui, Y. Liu, Y. Liu, and S X. Ma. Simuulation on gamma ray astronomy research with LHAASO-KM2A. *Astropart. Phys.*, 54:86–92, 2014.

[8] A. Karle et al. Design and performance of the angle integrating Čerenkov array AIROBICC. *Astropart. Phys.*, 3:321–347, 1995.

[9] Tunka Collaboration: N. M. Budnev et al. Tunka-133: Status 2008 and Development of Methods for Data Analysis. *Bull. Russ. Acad. Sci.: Phys.*, 73:588–592, 2009.

[10] M. Tluczykont et al. The HiSCORE concept for gamma-ray and cosmic-ray astrophysics beyond 10 TeV. *Astropart. Phys.*, 56:42–53, 2014. ArXiv: 1403.5688.

[11] TAIGA Collaboration: N. Budnev ,... S. Epimakhov, ... et al. The Tunka experiment: from cosmic ray to gamma astronomy. In *Proc. 24th ECRS, Kiel*, 2014.

[12] J. Blümer, R. Engel, and J.R. Hörandel. Cosmic Rays from the Knee to the Highest Energies. *Prog. Part. Nucl. Phys*, 63:293–338, 2009. ArXiv: 0904.0725.

[13] H. Hu. Status of the EAS studies of cosmic rays with energy below 1016 eV. 2009. ArXiv: 0911.3034.

[14] G.V. Kulikov and G. B. Kristiansen. On the size spectrum of extensive air showers. *J. Exp. Theor. Phys.*, 35:635, 1958.

[15] K. Greisen. End to the Cosmic-Ray Spectrum? *Phys. Rev. Lett.*, 16:748, 1966.

[16] G. T. Zatsepin et al. Upper limit of the spectrum of cosmic rays. *JETP Lett.*, 4:78, 1966.

[17] V. Berezinsky. Extragalactic cosmic rays and their signatures. *Astropart. Phys.*, 53:120–129, 2014. ArXiv: 1301.0914.

[18] J. A. Simpson. Elemental and Isotopic Composition of the Galactic Cosmic Rays. *Annu. Rev. Nucl. Part. Sci.*, 33:323–382, 1983.

[19] P. Sokolsky. *Introduction to Ultrahigh Energy Cosmic Ray Physics*. Westview Pres, 2004.

[20] J. R. Hörandel. Overview on direct and indirect measurements of cosmic rays - Some thoughts on galactic cosmic rays and the knee. *Int. J. Mod. Phys.*, A20:6753–6764, 2005. ArXiv: astro-ph/0501251.

[21] EAS-TOP Collaboration: Valchierotti S. et al. The Cosmic Ray Primary Composition in the Knee Region through the EAS Electromagnetic and Muon Measurements at EAS-TOP. In *Proc. 28th ICRC, Tsukuba, Japan*, 2003.

[22] KASCADE Collaboration: Roth M. et al. Energy Spectrum and Elemental Composition in the PeV Region. In *Proc. 28th ICRC, Tsukuba, Japan*, 2003.

[23] E. A. Vishnevskaya, V. N. Kalmykov, and N. N. Kalmykov. Cosmic ray energy spectrum derived from EAS electron, muon, and Cherenkov components. *Izv. Akad. Nauk, Ser. Fiz.*, 66:1566, 2002.

[24] Tunka Collaboration: N. M. Budnev et al. Simulation of the hybrid Tunka Area Instrument for cosmic rays and Gamma-ray Astronomy (TAIGA). In *Proc. 21th ECRS, Koăice*, 2008.

[25] KASCADE Collaboration: W. D. Apel et al. Energy spectra of elemental groups of cosmic rays: Update on the KASCADE unfolding analysis. *Astropart. Phys.*, 31:86–91, 2009. ArXiv: 0812.0322.

[26] KASCADE-Grande Collaboration: W. D. Apel et al. Ankle-like feature in the energy spectrum of light elements of cosmic rays observed with KASCADE-Grande. *Phys. Rev. D*, 87:081101(R), 2013. ArXiv: 1304.7114.

[27] K.-H. Kampert and M. Unger. Measurements of the Cosmic Ray Composition with Air Shower Experiments. *Astropart. Phys.*, 2012. Manuscript accepted for publication. ArXiv: 1201.0018.

[28] R.C.Hartman et al. The third EGRET catalog of high-energy gamma-ray sources. *Astrophys. J. Suppl. Ser.*, 123:79–202, 1999.

[29] Fermi-LAT Collaboration. Fermi Large Area Telescope Third Source Catalog. *Astrophys. J. Suppl.*, 2015. Manuscript submitted for publication. ArXiv: 1501.02003.

[30] P. F. Michelson, W. B. Atwood, and S. Ritz. Fermi Gamma-ray Space Telescope: High-Energy Results from the First Year. *Rept.Prog.Phys.*, 73: 074901, 2010. ArXiv: 1011.0213.

[31] Sc. Wakely and D. Horan. TeVCat: Online Gamma-Ray Catalog, 2015. URL `http://tevcat.uchicago.edu/`.

[32] A. A. Abdo et al. Discovery of TeV Gamma-Ray Emission from the Cygnus Region of the Galaxy. *Astrophys. J.*, 658:L33–L36, 2007. ArXiv: astro-ph/0611691.

[33] ARGO-YBJ Collaboration: B. Bartoli et al. TeV Gamma-Ray Survey of the Northern Sky Using the ARGO-YBJ Detector. *Astrophys. J.*, 779:27, 2013. ArXiv: 1311.3376.

[34] The Tibet AS Gamma Collaboration: M. Amenomori et al. Multi-TeV Gamma-Ray Observation from the Crab Nebula Using the Tibet-III Air Shower Array Finely Tuned by the Cosmic Ray Moon's Shadow. *Astrophys. J.*, 692:61, 2009. ArXiv: 0810.3757.

[35] F. A. Aharonian F. M. Rieger, E. de Ona-Wilhelmi. TeV Astronomy. ArXiv: 1302.5603, 2013.

[36] Drury L.O'. An introduction to the theory of diffusive shock acceleration of energetic particles in tenuous plasmas. *RPPh*, 46:973, 1983.

[37] R. Blandford and D. Eichler. Particle Acceleration at Astrophysical Shocks: a Theory of Cosmic Ray Origin. *Phys. Rep.*, 1154:1, 1987.

[38] HESS Collaboration: M. de Naurois et al. The Galactic Sky seen by H.E.S.S. *Adv. Space Res.*, 2011. Accepted for publication. ArXiv: 1104.1680.

[39] S. Gabici, F. A. Aharonian, and S. Casanova. Broad-band nonthermal emission from molecular clouds illuminated by cosmic rays from nearby supernova remnants. *MNRAS*, 2009. Submitted. ArXiv: 0901.4549.

[40] Q. Yuan, S. Liu (PMO), and X.-J. Bi. Unified model for the gamma-ray emission of supernova remnants. *Astrophys. J.*, 761:133, 2012. ArXiv: 1203.0085.

[41] D. Horns, F. Aharonian, A. Santangelo, A.I.D.Hoffmann, and C. Masterson. Nucleonic gamma-ray production in Vela X. *A&A*, 451:L51–L54, 2006.

[42] R. Antonucci. Unified Models for Active Galactic Nuclei and Quasars. *Annu. Rev. Astron. Astrophys.*, 31:473–521, 1993.

[43] C. A. Norman, D. B. Melrose, and A. Achterberg. The Origin of Cosmic Rays above 10^{18} eV. *Astrophys. J.*, 454:60, 1995.

[44] URL `http://www.auger.org/news/PRagn/images/agn4prouza.png`.

[45] J. Hinton. Ground-based gamma-ray astronomy with Cherenkov telescopes. *New J. Phys.*, 11:055005, 2009.

[46] Tunka-HiSCORE Collaboration: M. Tluczykont ,... S. Epimakhov, ... et al. Towards gamma-ray astronomy with timing arrays. In *Proc. 24th ECRS, Kiel*, 2014.

[47] M. Tluczykont et al. The ground-based large-area wide-angle γ-ray and cosmic-ray experiment HiSCORE. *J. Adv. Space Res.*, 2011. Manuscript accepted for publication. ArXiv: 1108.5880.

[48] S. Gabici and F. A. Aharonian. The ground-based large-area wide-angle γ-ray and cosmic-ray experiment HiSCORE. *Astrophys. J.*, 2007. In press. ArXiv: 0705.3011.

[49] Fermi-LAT Collaboration: M. Ackermann et al. Detection of the Characteristic Pion-Decay Signature in Supernova Remnants. *Sc. Mag.*, 339:807, 2013. ArXiv: 1302.3307.

[50] IceCube Collaboration: M. G. Aartsen et al. First observation of PeV-energy neutrinos with IceCube. *Phys. Rev. Lett.*, 111:021103, 2013. ArXiv: 1304.5356.

[51] G. Di Sciascio. Future Extensive Air Shower arrays: from Gamma-Ray Astronomy to Cosmic Rays. In *RICAP2014*, 2014. ArXiv: 1503.05512.

[52] Tunka-HiSCORE Collaboration. Gamma astronomy in the range above 10 TeV: the observatory Tunka-HiSCORE. URL `http://dec1.sinp.msu.ru/~tunka/proposal/`.

[53] U. Einhaus. Spektroskopie und Rekonstruktion von Quellen-Morphologie mit HiSCORE. Master thesis, Universität Hamburg, Germany, 2012.

[54] K. Bernlöhr. Air shower Cherenkov light simulations. URL `www.mpi-hd.mpg.de/hfm/CosmicRay/ChLight/ChLat.html`.

[55] D. Hampf. *Study for the wide-angle air Cherenkov detector HiSCORE and time gradient event reconstruction for the H.E.S.S. experiment.* PhD thesis, Universität Hamburg, Germany, 2012.

[56] Ch. Leinert et al. The 1997 reference of diffuse night sky brightness. *Astron. Astrophys. Suppl. Ser.*, 127:1–99, 1998.

[57] R. Mirzoyan and E. Lorenz. Measurement of the Night Sky Light Background at La Palma. Preprint MPI-PhE/94-35, 1994.

[58] S. Preuss, G. Hermann, W. Hofmann, and A. Kohnle. Study of the photon flux from the night sky at La Palma and Namibia, in the wavelength region relevant for imaging atmospheric Cherenkov telescopes. *NIM A*, 481:229–240, 2002. ArXiv: astro-ph/0107120.

[59] D. Hampf, G. Rowell, N. Wild, T. Sudholz, D. Horns, and M. Tluczykont. Measurement of night sky brightness in southern Australia. *Adv. Space Res.*, 48:1017, 2011.

[60] Tunka Collaboration: N. M. Budnev et al. The Tunka-133 EAS Cherenkov array - status, first results and plans. In *Proc. 31th ICRC, Lodz Poland*, 2009. ArXiv: 1003.0089.

[61] Tunka Collaboration: N. M. Budnev et al. The Cosmic Ray Mass Composition in the Energy Range 1015 - 1018 eV measured with the Tunka Array: Results and Perspectives. *Nucl. Phys. B (Proc. Suppl.)*, 190:247–252, 2009. ArXiv: 0902.3156.

[62] Tunka Collaboration: N. M. Budnev et al. Data acquisition system for the Tunka-133. In *Proc. 10th ICATPP, Como Italy*, 2007. ArXiv: 0804.0856.

[63] Tunka Collaboration: S. F. Berezhnev ,... S. Epimakhov, ... et al. The Tunka-133 EAS Cherenkov light array: status of 2011. *NIM A*, 2011. ArXiv: 1201.2122.

[64] Chernov D.V. et al. Methodics for measuring of pulse shape of Cherenkov light from EAS at Tunka array. Preprint SINP MSU 1/740, 2004.

[65] Tunka Collaboration: N. M. Budnev et al. Array for detection of EAS by Cherenkov light with area of 1 km^2 in Tunka valley. *Bull. Russ. Acad. Sci.: Phys.*, 69:395–399, 2005.

[66] Tunka Collaboration: V. V. Prosin ,... S. Epimakhov, ... et al. Tunka-133: Main Experimental Results of 3 Year Operation. In *Proc. 33rd ICRC, Rio de Janeiro*, 2013.

[67] N. Budnev et al. Tunka-25 Air Shower Cherenkov array: The main results. *Astropart. Phys.*, 50-52:18–25, 2013.

[68] E. E. Korosteleva, V. V. Prosin, L. A. Kuzmichev, and G. Navarra. Measurement of Cosmic Ray Primary Energy with the Atmosperic Cherenkov

Light Technique in Extensive Air Showers. *Nucl. Phys. B (Proc. Suppl.)*, 165:74–80, 2007.

[69] Pierre Auger Collaboration: M. Unger et al. Study of the Cosmic Ray Composition above 0.4 EeV using the Longitudinal Profiles of Showers observed at the Pierre Auger Observatory. In *Proc. 30th ICRC, Merida Mexico*, 2007. ArXiv: 0706.1495.

[70] Telescope Array Collaboration: H. Tokuno et al. New air fluorescence detectors employed in the Telescope Array experiment. *NIM A*, 676:54–65, 2012.

[71] J. R. Hörandel. On the Knee in the Energy Spectrum of Cosmic Rays. *Astropart. Phys.*, 19:193–220, 2003. ArXiv: astro-ph/0210453.

[72] T. Abu-Zayyad et al. Evidence for Changing of Cosmic Ray Composition between 1017 and 1018 eV from Multicomponent Measurements. *Phys. Rev. Lett.*, 84:4276, 2000.

[73] Tunka Collaboration: S. Epimakhov et al. Elemental Composition of Cosmic Rays above the Knee from the Xmax measurements of the Tunka Array. In *Proc. 33rd ICRC, Rio de Janeiro*, 2013.

[74] Tunka Collaboration: L. G. Sveshnikova ,... S. Epimakhov, ... et al. Cosmic ray spectrum above the knee measured by the Tunka-133 experiment: special features and possible interpretations. In *Proc. 33rd ICRC, Rio de Janeiro*, 2013.

[75] Tunka-HiSCORE Collaboration: N. Budnev ,... S. Epimakhov, ... et al. MSU DAQ for Tunka-HiSCORE : 8-channel DRS-4 Board. In *Proc. 24th ECRS, Kiel*, 2014.

[76] M. Kunnas. Bau eines Triggersystems für den HiSCORE-Detektor. Diploma thesis, Universität Hamburg, Germany, 2012.

[77] Tunka-HiSCORE Collaboration: M. Porelli ,... S. Epimakhov, ... et al. Timing calibration and derectional reconstruction for Tunka-HiSCORE. In *Proc. 24th ECRS, Kiel*, 2014.

[78] DRS4 chip. URL `http://drs.web.psi.ch/datasheets`.

[79] White Rabbit technology. URL `http://www.ohwr.org/projects/white-rabbit`.

[80] FPGA Spartan-6 SP605. URL `http://www.xilinx.com/products/boards-and-kits/ek-s6-sp605-g.html/`.

[81] Tunka-HiSCORE Collaboration: M. Brückner ,... S. Epimakhov, ... et al. Results from the WhiteRabbit sub-nsec time synchronization setup at HiSCORE-Tunka. In *Proc. 33rd ICRC, Rio de Janeiro*, 2013.

[82] R. Winston. Light Collection within the Framework of Geometrical Optics. *J. Opt. Soc. Amer.*, 60:245–247, 1970.

[83] R. Nachtigall. Charakterisirung von Photomultipliern und Beiträge zur Entwicklung eines Prototypen für Luftcherenkovmessungen. Diploma thesis, Universität Hamburg, Germany, 2011.

[84] C. R. Benn and S. L. Ellison. Brightness of the night sky over La Palma. *New Astron. Rev.*, 42:503–507, 1998.

[85] Hamamatsu Photonics K.K. Photomultiplier tubes. Basics and applications. 2006. URL `http://psec.uchicago.edu/links/pmt_handbook_complete.pdf`.

[86] H.M. Smith G.A. Morton and R. Wasserman. Afterpulses in Photomultipliers. *IEEE Trans. Nucl. Sci.*, NS-14(1):443, 1967.

[87] R. Mirzoyan et al. On the influence of afterpulsing in PMTs on the trigger threshold of multichannel light detectors in self-trigger mode. *NIM A*, 387: 74–78, 1997.

[88] K. Bernlöhr. Simulataion of imaging atmospheric Cherenkov telescopes with CORSIKA and sim_telarray. *Astropart. Phys.*, 30:149–158, 2008.

[89] V. Henke. Studie zur Auswertung der Ankuftszeitverteilung des Cerenkov-Lichts ausgedehnter Luftschauer. Diploma thesis, Universität Hamburg, Germany, 1994.

[90] Tunka-HiSCORE Collaboration: S. Epimakhov et al. Amplitude calibration with the HiSCORE-9 array. In *Proc. 24th ECRS, Kiel*, 2014.

[91] R. Mirzoyan. Conversation Factor Calibration for MAGIC Based on The Use of Measured F-Factor of PMTs. *MAGIC internal note*, 2000.

[92] T. Schweizer and E. Lorenz and M. Martinez and A. Ostankov and D. Paneque. The Optical Calibration of the MAGIC Telescope Camera. 2001.

[93] I. Fedorko, S. Tokar, and I. Chirikov-Zorin. Simulation of Photomultiplier Response. 1999.

[94] TAIGA Collaboration: V. V. Prosin ,... S. Epimakhov, ... et al. Results from Tunka-133 (5 Years Observation) and from the Tunka-HiSCORE Prototype. In *Proc. RICAP2014*, 2014.

[95] Tunka-HiSCORE Collaboration: V. Prosin ,... S. Epimakhov, ... et al. Primary CR Energy Spectrum and Mass Composition by the Data of Tunka-133 Array. In *Proc. ISVHECRI2014, CERN, Geneva*, 2014.

[96] D. Heck et al. CORSIKA: A Monte Carlo Code to Simulate Extensive Air Showers. In *FZKA 6090*, 1998.

[97] GEOMAG. URL `http://www.ngdc.noaa.gov/geomag/`.

[98] D. Hampf, M. Tluczykont, and D. Horns. Event reconstruction techniques for the wide-angle air Cherenkov detector HiSCORE. *Nucl. Instr. Meth. Phys. Res. A*, 2013. Manuscript submitted for publication. ArXiv: 1302.3957.

[99] Tunka-HiSCORE Collaboration: R. Wischnewski ,... S. Epimakhov, ... et al. Status of the HiSCORE experiment. In *Proc. 33rd ICRC, Rio de Janeiro*, 2013.

[100] T.-P. Li and Y.-Q. Ma. Analysis methods for results in gamma-ray astronomy. *Astrophys. J.*, 272:317–324, 1983.

[101] Tunka-HiSCORE Collaboration: M. Kunnas ,... S. Epimakhov, ... et al. Simulation of the hybrid Tunka Area Instrument for cosmic rays and Gamma-ray Astronomy (TAIGA). In *Proc. 24th ECRS, Kiel*, 2014.

[102] MAGIC Collaboration: J. Aleksić et al. Measurement of the Crab Nebula spectrum over three decades in energy with the MAGIC telescopes. 2014. ArXiv: 1406.6892.

[103] M. Bensimhoun. N-Dimensional Cumulative Function, And Other Useful Facts About Gaussians and Normal Densities. Preprint, 2006.

[104] Pierre Auger Collaboration: Kobal M. et al. A thinning method using weight limitation for air-shower simulations. *Astropart. Phys.*, 15:259–273, 2001.

[105] R. Bruijn, F. Schmidt, and J. Ileeand J. Knapp. Study of statistical thinning with fully-simulated air showers at ultra-high energies. In *Proc. 31th ICRC, Lodz Poland*, 2009.

[106] B. T. Stokes, R. Cady, D. Ivanov, J. N. Matthews, and G. B. Thomson. Dethinning Extensive Air Shower Simulations. *Astropart. Phys.*, 2012. Manuscript submitted for publication. ArXiv: 1104.3182.

[107] B. T. Stokes, R. Cady, D. Ivanov, J. N. Matthews, and G. B. Thomson. A Simple Parallelization Scheme for Extensive Air Shower Simulations. *Astropart. Phys.*, 2011. Manuscript submitted for publication. ArXiv: 1103.4643.

[108] A. Razdan, A. Haungs, H. Rebel, and C. L. Bhat. Image and Non-Image Parameters of Atmospheric Cherenkov Events: a comparative study of their gamma-ray/hadron classification potential in UHE regime. *Astropart. Phys.*, 17:497–508, 2002. ArXiv: astro-ph/0109476.

[109] S. Ostapchenko. Monte Carlo treatment of hadronic interactions in enhanced Pomeron scheme: QGSJET-II model. *Phys. Rev. D*, 83:014018, 2011. ArXiv: 1010.1869.